

Numerical analysis of scattering from certain conducting and dielectric bodies of arbitrary shape

by

HAMID MOHEB

A thesis submitted to the Faculty of Graduate Studies of the University of Manitoba in partial fulfillment of the requirements for the degree of

DOCTOR OF PHILOSOPHY

© 1990

Permission has been granted to the LIBRARY OF THE UNIVERSITY OF MANITOBA to lend or sell copies of this thesis. To the NATIONAL LIBRARY OF CANADA to microfilm this thesis and to lend or sell copies of the film, and UNIVERSITY MICROFILMS to publish an abstract of this thesis.

The author reserves other publication rights, and neither the thesis nor extensive extracts from it may be printed or otherwise reproduced without the author's written permission.



National Library
of Canada

Bibliothèque nationale
du Canada

Canadian Theses Service Service des thèses canadiennes

Ottawa, Canada
K1A 0N4

The author has granted an irrevocable non-exclusive licence allowing the National Library of Canada to reproduce, loan, distribute or sell copies of his/her thesis by any means and in any form or format, making this thesis available to interested persons.

The author retains ownership of the copyright in his/her thesis. Neither the thesis nor substantial extracts from it may be printed or otherwise reproduced without his/her permission.

L'auteur a accordé une licence irrévocable et non exclusive permettant à la Bibliothèque nationale du Canada de reproduire, prêter, distribuer ou vendre des copies de sa thèse de quelque manière et sous quelque forme que ce soit pour mettre des exemplaires de cette thèse à la disposition des personnes intéressées.

L'auteur conserve la propriété du droit d'auteur qui protège sa thèse. Ni la thèse ni des extraits substantiels de celle-ci ne doivent être imprimés ou autrement reproduits sans son autorisation.

ISBN 0-315-63282-8

Canada

**NUMERICAL ANALYSIS OF SCATTERING FROM CERTAIN
CONDUCTING AND DIELECTRIC BODIES OF ARBITRARY SHAPE**

BY

HAMID MOHEB

A thesis submitted to the Faculty of Graduate Studies of
the University of Manitoba in partial fulfillment of the requirements
of the degree of

DOCTOR OF PHILOSOPHY

© 1990

Permission has been granted to the LIBRARY OF THE UNIVER-
SITY OF MANITOBA to lend or sell copies of this thesis, to
the NATIONAL LIBRARY OF CANADA to microfilm this
thesis and to lend or sell copies of the film, and UNIVERSITY
MICROFILMS to publish an abstract of this thesis.

The author reserves other publication rights, and neither the
thesis nor extensive extracts from it may be printed or other-
wise reproduced without the author's written permission.

ABSTRACT

A numerical method is developed to study the electromagnetic scattering from three-dimensional geometries, which is a generalization of the method previously used for bodies of revolution. On the object's surface two orthogonal tangent vectors are defined. Along one, the surface currents are represented by discrete triangular basis functions and along the other by a finite set of entire domain basis functions. To enable the latter expansion two different techniques are adopted. In one, called the method of coordinate transformation, the object's cross-section is conformally transformed onto a circle, and cylindrical basis functions are selected in the new space. In the second technique Fourier type basis functions are used directly in the physical coordinates of the object. The developed methods are then applied to study the scattering from geometries such as cubes and plates. The behavior of the solutions with different number of modes are investigated to determine their coupling. The conformal transformation method is applicable to any geometry of arbitrary cross-section, but it needs the transformation function to be useful. The direct method, on the other hand, does not have such a restriction. Both methods are, however, limited in use to small objects when their size is in order of the wavelength.

The developed methods are then extended to treat dielectric geometries of arbitrary shape. The surface integral equations are formulated in terms of the equivalent electric and magnetic currents over the object's surface. The surface currents are obtained from the tangential components of the fields and related to the integral operators of the conducting objects. The resulting integral equations are solved similarly.

Finally, the developed techniques are also applied to the antenna problems, in particular, for handling the radiation from rectangular waveguides. An x-directed dipole is used as a source of excitation and the radiation characteristics of the rectangular waveguides are determined.

ACKNOWLEDGMENT

The author would like to express his sincere gratitude to professor L. Shafai, advisor and friend, for his counsel, guideness and continuous encouragement over the course of this work. I am also indebted to him for taking the time in long late night discussions and valuable suggestions. Indeed, to the author, he is more than an advisor.

Special thanks to my parents for their continuous support and consideration, during my study in the United States and Canada.

Extended thanks are due to my lovely fiancée, Mahta, for her kindness and words of encouragement during the final stage of my Ph.D. program, which made this work possible.

Special acknowledgment go to my colleague and friend R. Epp, for many valuable comments and helpful discussions.

Financial assistance provided by the Natural Sciences and Engineering Research Council of Canada is gratefully acknowledged.

TABLE OF CONTENTS

Abstract	i
Acknowledgements	ii
List of principle symbols	vi
List of Tables	ix
List of Figures	x
Chapter 1: Introduction	1
1.1. Introduction	1
1.2. Literature Survey on Integral Equation	2
1.2.1. Conducting Bodies	2
1.2.1.1. Geometrical Singularity	4
1.2.1.2. Numerical Techniques	5
1.2.1.3. Basis Function	7
1.2.2. Dielectric Bodies	9
1.3. Statement of the problem	11
Chapter 2: Conformal Transformation Method	14
2.1. Introduction	14
2.2. E-field formulation	17
2.3. H-field formulation	22
2.4. Plane wave excitation and far field	25
2.5. Transformation	28
2.6. Numerical Results	30
2.6.1. Objects with square cross-section	36

2.6.2. Rectangular prism	40
2.6.3. Effect of the incidence angle	47
2.7. Conclusions	47
Chapter 3: Direct Method	52
3.1. Introduction	52
3.2. Matrix formulation	53
3.3. Excitation matrix	58
3.4. Numerical results	59
3.4.1. cube	60
3.4.2. plate	61
3.5. Conclusions	63
Chapter 4: Scattering from dielectric objects	74
4.1. Introduction	74
4.2. Analysis	76
4.3. Matrix Formulation	79
4.3.1. <i>PMCHW</i> and <i>Müller</i> matrices	80
4.3.2. E-field matrix	81
4.3.3. H-field matrix	82
4.3.4. C-field matrix	82
4.4. Scattered field	84
4.5. Numerical results	85
4.6. Conclusions	95
Chapter 5: Rectangular Waveguide Feed	103
5.1. Introduction	103

5.2. Formulation	106
5.3. Numerical results	110
5.4. Conclusions	122
Chapter 6: Discussion, Conclusions and Recommendations	123
6.1. Discussion and conclusions	123
6.2. Recommendations	127
Appendix I: Coordinate transformation	129
Appendix II: Triangular basis function	132
Appendix III: Far field components of an x-directed dipole	135
References	137

List of principle symbol

Unless otherwise stated, the symbols most commonly used in this thesis have the following meaning:

α	orientation angle used with unit vector \hat{u}_s
β	orientation angle used with unit vector \hat{u}_t
χ, ξ	polar coordinates of the transformed space
∇	Gradient operator
∇_s	surface divergence operator
ϵ_e, μ_e	permittivity and permeability of the exterior region
ϵ_d, μ_d	permittivity and permeability of the dielectric region
η_q	characteristic impedance of the medium
γ	combination parameter
λ	wavelength in free space
μ	permeability of medium
ω	radian frequency
ϕ	electric scalar potential
$c(\xi), \phi(\xi), z$	circular cylindrical coordinates of the transformed space
σ	electric charge density
σ^{pq}	scattering cross-section
u, v	coordinates of the half space
ξ, c, z	transformed coordinates system
$h(\xi)$	metric coefficient
$\left \frac{dZ}{d\zeta} \right ^2$	Jacobian of the transformation
A	electric vector potential

a_{ni}	electric expansion coefficients
b_{nj}	magnetic expansion coefficients
$2a$	length of the rectangle
$2b$	width of the rectangle, (chapter II)
<i>CTM</i>	Conformal Transformation Method
<i>CFIE</i>	Combined Field Integral Equation
<i>DM</i>	Direct Method
<i>EFIE</i>	Electric Field Integral Equation
E_q	scattered electric field
E^i	incident electric field
$E_l(\mathbf{J})$	electric field due to currents \mathbf{J} , radiating in a medium characterized by ϵ_l, μ_l
$E_l(\mathbf{M})$	electric field due to currents \mathbf{M} , radiating in a medium characterized by ϵ_l, μ_l
$f_j(t)$	triangle function
G	scaler Green's function
$h_0^2(R)$	spherical Hankel function of the second kind and zero order
H^i	incident magnetic field
$H_l(\mathbf{J})$	magnetic field due to currents \mathbf{J} , radiating in a medium characterized by ϵ_l, μ_l
$H_l(\mathbf{M})$	magnetic field due to currents \mathbf{M} , radiating in a medium characterized by ϵ_l, μ_l
I_{mi}^p	excitation column matrix
\mathbf{II}	dipole moment
\mathbf{J}	electric surface current
k_q	propagation constant in a medium characterized by ϵ_q, μ_q
\mathbf{M}	magnetic surface current

$MFIE$	Magnetic Field Integral Equation
n, m	Fourier mode numbers
\hat{n}	normal unit vector on S
r_r, θ_r, ϕ_r	far field point in spherical coordinates
R	distance between the field and the source points
R_{mi}^{pq}	scattering column matrices
T_i	coefficients of the triangle function
T_i'	coefficients of the derivative of the triangle functions
\hat{l}_t, \hat{l}_s	unit vectors tangential to the body
$\hat{l}_\theta, \hat{l}_\phi$	unit vectors in a spherical coordinates
V_{mi}^p	excitation column matrix
$W_i(t)$	testing function
x, y, z	field point in a Cartesian coordinates
$(Y_{mng}^{pq})_{ij}$	admittance matrix for a medium characterized by ϵ_g, μ_g
$(Z_{mng}^{pq})_{ij}$	impedance matrix for a medium characterized by ϵ_g, μ_g

LIST OF TABLES

Table		page
2.1	Radar cross-section of a square plate of size $L = 1.0\lambda$ and thickness $t = 0.0317 \lambda$.	32
2.2	Radar cross-section of a square plate of size $L = 0.2 \lambda$ and thickness $t = 0.0317 \lambda$.	32
2.3	Parameters used in computing the back scattering of a cube of size $L = 0.75 \lambda$.	33
2.4	Magnitude of current coefficients of a conducting cube of size $L = 1.5 \lambda$, computed in the 45° plane.	38
4.1	Parameters used in computing the bistatic scattering patterns of a dielectric cube of size $L = 0.75 \lambda$.	94

LIST OF FIGURES

Figure		page
2.1	Coordinate geometry of a conducting cube of side length L .	16
2.2	Bistatic scattering patterns of a conducting cube of $L = 0.75 \lambda$.	35
2.3	Back scattering cross section of a conducting square plate of thickness $t = 0.0317 \lambda$, for a normal incident plane wave.	35
2.4	Bistatic scattering patterns of a conducting cube for a normal incident plane wave, (a) $A = 2.25\lambda^2$, (b). $A = 9.0\lambda^2$.	41
2.4.c	Bistatic scattering patterns of a conducting cube of side length $L = 5.0 \lambda$ for a normal incident plane wave, same polarization as Fig. 3a.	42
2.5	Auxiliary current distributions on the surface of conducting plate of $L = 1.0 \lambda$ and thickness $t = 0.0317 \lambda$, for a normal incident plane wave.	43
2.6	Back scattering cross-section of a conducting rectangular box of $h = 0.5 \lambda$.	42
2.7	Back scattering cross-sections of a conducting rectangular plate of aspect ratio $AR = 0.5$ and thickness $t = 0.0317\lambda$, for a normal incident plane wave.	45
2.8	Back scattering cross-sections of a conducting rectangular plate of aspect ratio $AR = 0.25$ and thickness $t = 0.0317\lambda$, for a normal incident plane wave.	45
2.9	Back-scattering cross-section of a conducting rectangular box of aspect ratio $AR = 0.5$ and height $h = 1.0 \lambda$, for a normal incident plane wave.	46
2.10.a	Contribution of various modes to the bistatic scattering cross-section	

	of a conducting square plate of side length $L = 1.0 \lambda$ and thickness $t = 0.1 \lambda$ for a plane wave incidence.	49
2.10.b	Contribution of various modes to the bistatic scattering cross-section of a conducting square plate of side length $L = 1.0 \lambda$ and thickness $t = 0.1 \lambda$ for a plane wave incidence.	50
2.11	Bistatic scattering cross-sections of a conducting square plate of side length $L = 1.0 \lambda$ and thickness $t = 0.1 \lambda$, for a oblique incident plane wave.	51
3.1.a	Bistatic scattering patterns of a conducting cube of side length $L = 0.75 \lambda$ for a normal incident plane wave.	65
3.1.c	Bistatic scattering pattern of a conducting cube of side length $L = 0.75 \lambda$ for a normal incident plane wave.	66
3.2	Back scattering cross-section of a conducting cube of side length L , for a normal incident plane wave.	67
3.3	Back scattering cross-section of a conducting square plate of thickness $t = 0.0317 \lambda$, for a normal incident plane wave.	67
3.4	Back scattering cross-sections of a conducting rectangular plate of aspect ratio $AR = 0.5$ and thickness $t = 0.0317\lambda$, for a normal incident plane wave.	68
3.5	Current distributions on the surface of conducting plate of $L = 0.6 \lambda$ and thickness $t = 0.0317 \lambda$, for a normal incident plane wave.	69
3.6.a	Bistatic scattering cross-sections of a conducting square plate of side length $L = 1.0 \lambda$ and thickness $t = 0.1 \lambda$, for a normal incident plane wave.	70
3.6.b	Contribution of various modes to the bistatic scattering cross-section of a conducting square plate of side length $L = 1.0 \lambda$ and thickness $t = 0.1 \lambda$ for a plane wave incidence.	71

3.7.a	Bistatic cross-section of a conducting square plate of side length $L = 1.0 \lambda$ and thickness $t = 0.1 \lambda$, for a oblique incident plane wave.	72
3.7.b	Contribution of various modes to the bistatic scattering cross-section of a conducting square plate of side length $L = 1.0 \lambda$ and thickness $t = 0.1 \lambda$ for a plane wave incidence.	73
4.1	(a) Original problem. (b) outside equivalence. (c) inside equivalence.	77
4.2.a	E- and H-plane scattering patterns for a dielectric sphere of $ka = 3.0$, and $\epsilon_r = 4$, for a normal incident plane wave.	86
4.2.b	Bistatic scattering patterns for a dielectric cylinder of $a = 0.25 \lambda$, $h = 2a \lambda$, and $\epsilon_r = 4$, for a normal incident plane wave.	87
4.3.a	Bistatic scattering patterns for a dielectric cube of size $L = 0.2 \lambda$, $\epsilon_r = 4$, $n = 1$, and 4 pulses per triangle, for a normal incident plane wave.	88
4.3.b	Bistatic scattering patterns for a dielectric cube of size $L = 0.2 \lambda$, $\epsilon_r = 9$, $n = 1$, and 4 pulses per triangle, for a normal incident plane wave.	89
4.4.a	Bistatic scattering patterns for a dielectric cube of size $L = 0.2 \lambda$, $\epsilon_r = 4$, $n = 1$, and 6 pulses per triangle, for a normal incident plane wave.	92
4.4.b	Bistatic scattering patterns for a dielectric cube of size $L = 0.2 \lambda$, $\epsilon_r = 4$, $n = 1$, and 6 pulses per triangle, for a normal incident plane wave.	93
4.5	Contribution of various modes to the bistatic scattering cross-section of a dielectric cube of side length, $L = 0.2 \lambda$, for a normal incident plane wave.	97
4.6	Same as Fig. 4.5, the E-field solution	98
4.7	Same as Fig. 4.5, the H-field solution	99
4.8	Same as Fig. 4.5, the C-field solution	100
4.9	Same as Fig. 4.5, the PMCHW solution	98
4.10	Bistatic scattering pattern for a dielectric cube of size $L = 0.256 \lambda$, $\epsilon_r = 4$, for a normal incident plane wave.	102

5.1	Physical and numerical modeling of a rectangular waveguide.	107
5.2	Radiation pattern of a rectangular waveguide, $a = 0.5 \lambda$, $b = 0.22 \lambda$, $L = 1.5 \lambda$, and $f = 1.1f_c$.	114
5.3	Effect of the waveguide length on the radiation pattern, $a = 0.686 \lambda$, $b = 0.305 \lambda$, $n = 1$ mode, and $f = 1.37f_c$.	115
5.4.a	Contribution of higher order modes to the radiation pattern of a rectangular waveguide, $a = 0.686 \lambda$, $b = 0.305 \lambda$, $L = 1.5 \lambda$, and $f = 1.37f_c$.	116
5.4.b	Same as Fig. 5.4.a except $f = 1.82f_c$.	117
5.5	Effect of the wall thickness on the radiation pattern, $a = 0.686 \lambda$, $b = 0.305 \lambda$, $L = 1.5 \lambda$, $n = 1$ mode, and $f = 1.37f_c$.	118
5.6	Radiation pattern of a rectangular waveguide, $a = 0.686 \lambda$, $b = 0.305 \lambda$, $L = 1.5 \lambda$, and $f = 1.37f_c$.	119
5.7.a	Cross-polar characteristic of a square waveguide.	120
5.7.b	Cross-polar radiation pattern of a rectangular waveguide of $L = 1.2 \lambda$ and $n = 1$ mode.	120
5.7.c	Cross-polar radiation pattern of a rectangular waveguide of $a = 0.686 \lambda$, $b = 0.305 \lambda$, $L = 1.5 \lambda$, $n = 1$ and $f = 1.37f_c$.	121
I.1	Coordinate transformation of an object with a rectangular cross-section.	131
II.1	Generic curve of the geometry.	134

Chapter 1

Introduction

1.1. Introduction

Most of the problems in electromagnetic field involve determination of the field distribution of a given source in the presence of material bodies. To achieve this goal, the problem must be formulated first and then solve by a suitable mean to generate useful results. In practical problems developing a formulation is usually straightforward, but obtaining a solution for them is often a difficult task. Two fundamental approaches can be taken to lead to formulations, which are based on differential or integral forms of the field equations. The former leads to well known boundary value problems for the wave equation and the latter provides integral equation formulations for the field distributions. In either case, analytic solutions for the required field components can only be obtained, when the shape of the material objects is simple and coincides with one of the surfaces. Otherwise a numerical method must be used. This thesis deals with the development of such a method, using integral equations. For this reason this chapter provides a brief review of the recent contributions by various authors to the development of solutions using integral equation formulations.

1.2. Literature Survey on Integral Equations

1.2.1. Conducting Bodies

The problem of scattering from arbitrary conducting objects is a complex mathematical boundary value problem. One of the traditional approaches is based on integral equation formulation, which is capable of handling complex structures. The starting point for developing such an integral equation model in electromagnetics, is the selection of a Green's function appropriate for the problem. A popular choice is the Green's function for the infinite medium, which simplifies the formulation. The formulation, on the other hand, is often generated using a Green's theorem. This leads to the Kirchoff integrals from which the fields in a given set of contiguous volumes of space can be written in terms of integrals over the surfaces enclosing them and volume integrals over those sources located within them. Such an analytic formulation leads to an integral operator, whose kernel can also include differential operators, which act on the unknown sources or fields. Historically, two kinds of integral equations were derived, in 1949, by Maue [1] for the surface current density excited by arbitrary harmonic fields incident upon a perfect electric conductor in free space. One, known as an Electric Field Integral Equation (*EFIE*), is a Fredholm integral equation of the first kind, in which the unknown appears only under the integral. The other one, known as a Magnetic Field Integral Equation (*MFIE*), is a Fredholm integral equation of the second kind, in which the unknown also appears outside the integral. Either integral equation holds for both exterior and interior regions. However, when they are applied to an exterior region, they fail to yield a unique solution for the surface current at frequencies equal to the resonant frequencies of the corresponding interior cavity, even though the exterior solution to Maxwell's equations, subject to boundary and radiation conditions for a perfectly conducting scatterer exists uniquely [2].

Four basic methods have been purposed successfully for eliminating the spurious resonances from the electromagnetic exterior surface integral equation solutions. They are referred to as the combined-field solution (*CFIE*) [3], combined-source solution [4], hybrid method [5], and the augmented electric- and magnetic-field integral equations (*AEFIE*, *AMFIE*) [6]. While each of these methods offer advantages in removing the spurious solutions, they suffer from limitations. For instance, an accurate solution of *AMFIE* is limited to geometries of the order of 1λ in size, and the *CFIE* requires an optimum weighting parameter to construct an integral equation valid at all frequencies. On the other hand, the combined-source formulation fails in handling the problem of zero-thickness bodies, and the radiation from apertures on conducting surfaces which were not closed before cutting the aperture.

The main difficulty encountered in integral equation solutions lies in the numerical approximation to the integration process for the kernels, which is due to the singularity of the Green's function, when the observer and source locations coincide. In avoiding this difficulty by merely skipping over the singularity, matrix conditioning generally deteriorates due to a loss in the diagonal dominance.

Improved conventional methods have relied, among others, on complex variable transforms, and the evaluation of Cauchy principle values. Being predominantly analytic, these techniques are necessarily problem geometry dependent, thus restricting their wide-spread application due to a lack in generality. With a few exceptions, their use entails tedious manipulations. A convenient scheme that is numerical in concept, thus yielding for automation may be obtained by displacing the field point a distance d perpendicular to the plane of the source. This method has been applied in the numerical formulation of rotationally symmetric conducting and dielectric bodies by Mautz and Harrington [7] and combined bodies by Kishk and shafai[8].

1.2.1.1. Geometrical Singularity

Source discontinuities due to geometrical singularities, i.e., edges or corners, where source densities rise rapidly to infinity, are of secondary importance with respect to the integral equation solution. However, the proper modeling of such limiting behaviors accelerates the convergence and improves the precision of computed near-field quantities. Other factors that contribute to inaccuracies in the field solution include, incompatibility of boundary conditions at common edges or points, and abrupt changes in the direction of boundary surfaces or contours that lead to singular derivatives of the field. The latter arises wholly from the geometrical considerations and frequently causes a situation where the integrand is singular but its integral is finite. Interpolatory polynomials, no matter how high their order, cannot be expected to represent the field in the vicinity of the singular points as accurately as desired, mathematically, because of the fact that polynomial functions are not complete for this task. Hence, convergence is usually slow and also depends on the degree of modeling and the method of solution. The prediction of the singular behavior is dependent on the expansions for the solution and jumps in boundary conditions. In general, to accelerate convergence, special functions are required to approximate the discontinuous behavior of the field.

Explicit forms and orders of singularity are obtainable in closed form from two-dimensional analyses of geometries where separation of variables may be invoked [9]-[11]. For the static case, the edges and right-angled corners have orders of singularity as $r^{-\frac{1}{2}}$ and $r^{-\frac{1}{3}}$, with r being the distance from the corner, respectively. In the case of scattering from conducting objects, the order of singularity becomes depended on the particular configuration and the media surrounding it. By representing the electromagnetic field vectors as a power series of radial distance from the edge and substituting in Maxwell's equations, Meixner has shown that [12], for the right angled conducting corner the singular components of the field behave as $r^{-\frac{1}{3}}$, which is similar to the stat-

ic case. one method of eliminating such a problem is to use a conformal transformation to remove the geometrical discontinuity. Such a transformation introduces a scale factor into the integral equation through the use of a complex variable transformation and thus provides more regular expressions [13]-[15].

1.2.1.2. Numerical Techniques

There are basically two class of numerical techniques that are used for solving a linear system of equations resulting from an integral equation formulation. One, is a direct method, and the other is the iterative method.

The direct method gives an answer in a fixed number of steps subject to rounding errors and the iterative technique achieves an acceptable solution after a number of iterations via an iteration strategy.

One of the most powerful direct techniques that can be utilized to carry out the numerical evaluation of the integral equations is the method of moments [16]. It is a generic name for a variety of techniques which solve a linear operator equation by converting it to a matrix equation. A numerical implementation of the moment method is relatively straightforward and is based on an expansion of the surface field distributions in series of suitable basis functions. Utilizing a set of testing functions, together with the evaluation of their moments, the integral equations can be reduced to a set of simultaneous linear equations, a solution of which gives the required surface distributions. The method, while being generally applicable to any scattering problem, is limited by the storage and computation time of computers. This limitation is most severe for dielectric bodies wherein existence of both equivalent electric and magnetic surface distributions increases the size of the moment matrix compared with that of perfectly conducting case. In such a case, and for a given object size, the larger matrix size results in costlier solutions or, alternatively, in less accurately calculated near field

parameters. However, if only the far field patterns were desired, usually lower degree of accuracy in the solution of the matrix equation can be tolerated. This is due to the fact that, the accuracy of the far field is generally better than that of the surface currents.

Another technique which has been used in the scattering matrix formulation is developed by Waterman [17]. It is called the extended boundary condition method, and provides a general formulation for the scattering from conducting and dielectric bodies of arbitrary size and shape, with sizes from the Rayleigh region to the geometrical optics limit.

There are also several hybrid techniques available to solve the scattering problems. One example is that of combining the moment method with the geometrical theory of diffraction (*GTD*), [18]-[19]. The advantage of this technique over the moment method, is that of the computation time, in which the *GTD* computer run time is essentially independent of the frequency. On the other hand, the *GTD* suffers from ray tracing which ultimately limits its applicability. Nevertheless, such hybrid techniques have potential for developing solutions involving large, and complex problems.

Another hybrid technique that deals with the numerical solution of integral equations in field problems is the unimoment method [20]. This method is a combination of the finite element method and the method of moments and is based on replacing the integral equations by finite difference or finite element equations. As implemented by Mie [20], this technique involves solving an interior problem using finite-differences involving a shooting method, or a Ricatti transformation for the generation of trial function pairs. The exterior solution is then expanded by cylindrical or spherical harmonics with unknown coefficients and matched at the interface, thus requiring the solution of a system of $4N$ linear equations. The ability of the technique to handle inhomogeneous structures [21] is one of its main advantages in engineering applications.

There are a number of numerical schemes, by which the cost of a moment method solution can be reduced. As discussed by Miller [22], the approach basically consists of solving the original integral equation by iterative techniques such as a Jacobi, Gauss-Seidel [22], and the conjugate-gradient method (*CGT*) [23], [24]. They vary basically in handling the updating procedure at each iteration step. The iterative techniques are usually implemented via the Fast Fourier Transform (*FFT*) to improve the computational efficiency [25]. The advantage gain is due to the fact that integral equations have the form of a spatial convolution between the unknown and the kernel functions. Consequently, the order of the discretized form of the integral equation is decreased from a squared dependence on the unknowns to a linear one (product of two sample spectra). However, since the boundary conditions are expressed in the real space and the product in the spectral space, an iteration to achieve a valid solution becomes necessary. The method is often described as the *k*-space transform [26], the spectral-iterative technique [27], [28], and the *FFT* approach [25]-[29].

1.2.1.3. Basis Function

In order to solve integral equations by means of numerical techniques such as a method of moment, a set of appropriate basis functions is required. Among the various choices of possible functions only a few exhibit optimal properties to yield solutions with acceptable accuracies. The criteria which affect the optimal choice of a basis function are; the computational efficiency, numerical stability and capability of accounting for boundary conditions or the continuity requirements.

There are basically two classes of basis functions that are used in numerical modelings, they are the subdomain basis functions and entire domain basis functions. The former involves the basis functions that are finite over small segment of the object and lead to a single unknown constant for each subdomain. The entire domain

basis functions, on the other hand, utilize series expansions such as Fourier series extending over the entire object. The selection of basis functions employed in the numerical computations depends, ultimately on the resemblance of the physical behavior of the unknown it represents, and reducing the computational effort needed to obtain the unknown coefficients. Although subdomain bases are quite efficient and simple to use, they possess the lack of discontinuity that occurs at the domain boundaries. On the other hand, the entire domain bases have advantages in continuous differentiability of the set and the possibility of handling larger objects. However, they exhibit a tendency for oscillatory behavior even if the solution function has a smooth behavior.

Based on the foregoing discussion on the selection of basis functions, two numerical modeling strategies have been used successfully in solving the scattering problems. They are the wire-grid, and the surface-patch techniques. The wire-grid technique has been remarkably successful, in predicting the far-field quantities such as the radiation patterns and radar cross-sections [30], [31]. In addition to resulting in a surface model of the object, which is easy to employ on the computer, the technique has the advantage that all numerically computed integrals are essentially one-dimensional. However, it is not well-suited for calculating near-field quantities such as surface currents and the input impedance. This technique is sensitive to the wire grid diameter and wire spacing [32] and its accuracy has also been questioned on the theoretical grounds [33], and due to its difficulties with the internal resonances. These difficulties have resulted in the development of surface patch models, as an alternative to the wire-grid technique, whereby the body is described by planar rectangular patches [34], [35], triangular patches [36], [37], or polygonal patches [38].

The choice of hybrid bases, where sub-domain and entire-domain bases are selected on different parts of an object has provided both a solution stability and a reduction in computer processing time. This technique was first employed for handling conducting and dielectric bodies of revolution (*BOR*) by Mautz and Harrington [39] and later

for conducting bodies of translation (*BOT*) by Medgysei-Mitschang and Putnam [40]. In either cases the functional variation of the current on the generating curve of the scatterer is represented by sub-domain basis functions and the circumferential variation by an entire-domain basis functions. A similar approach is adopted in the present work.

1.2.2. Dielectric Bodies

In many problems involving radar scattering it is desirable to understand the scattering properties of dielectric bodies. A knowledge of the scattered field of dielectric objects is required in many area, such as propagation of microwaves through rain or snow, scattering by chemical and biological particles, and performance of communication antennas in the presence of dielectric inhomogeneities. Analytic solutions are possible for a few geometries such as a sphere in the form of Mie series for both homogeneous spheres [41] and multilayered spheres [42]. A theoretical formulation, employing spherical basis functions in conjunction with the extended boundary condition method has also been developed to treat dielectric spheres, spheroids and finite cylinders [43].

For bodies of arbitrary shape, numerical techniques are often used to formulate the scattering from dielectric objects. A number of methods have been developed and applied to two and three dimensional scattering problems [44]-[50]. Some of these are restricted to bodies of revolution, while others have been demonstrated only for homogeneous bodies.

The method used in [40] for conducting bodies of revolution has been extended in [47] to treat dielectric bodies of revolution by incorporating the equivalent electric and magnetic surface currents. The unknown surface currents are then found by a Fourier decomposition, using a moment method, and the solution accuracy is depen-

dent on the material permittivity.

The methods presented in [45] and [46] are based on time-domain formulations and are not suitable for single frequency applications. Whereas, the methods of [50], [51] apply to arbitrarily shaped bodies by utilizing cubical or rectangular cells. However, in order to accurately model arbitrarily curved body surfaces, a large number of cells must be utilized. Here, pulse expansion functions are employed to expand the unknown field within the body. This can lead to a divergence of the numerical solution, when the cells are subdivided to smaller ones.

The method based on the surface integral equation employing the equivalent electric and magnetic surface currents and volume integral equation utilizing the equivalent electric polarization current has been developed to treat the far-scattered fields of composite dielectric cubes [52]. Triangular patches are used in the surface formulation and cubical cells are used in the volume formulation. The volume integral formulation, however, is somewhat limited to thin layers of dielectric materials, due to an increase in the size of the moment matrix. Also, it is not recommended for the near field computations, since the selected basis functions for the currents, can result in a charge build up within the body.

A volume integral equation is formulated in [53] and solved by using the method of moments. Tetrahedral volume elements are used to model a scattering body in which the electrical parameters are assumed constant in each tetrahedron. Special basis functions are defined within the tetrahedral volume elements to insure that the normal component of the electric field satisfies the correct jump condition at interfaces between different dielectric media. The accuracy of the developed technique is compared to that of cubical cell methods [52]. Its practical applications, however, is somewhat limited because of the extensive computer time needed to fill the moment method matrix.

An iterative technique is also used to solve the scattering problem of arbitrary shape inhomogeneous, and anisotropic objects [54]. The surface electric field integral equation is solved using the conjugate gradient technique and an *FFT* algorithm. The main draw back of the method is that the convergence rate slows down when the relative permittivity of the object becomes large (≥ 10). Also, the computation has to be repeated for different incident fields.

1.3. Statement of the problem

In this work, a method similar to that of Mautz and Harrington [40] is used to study the scattering of electromagnetic waves by conducting and dielectric bodies of arbitrary cross-section. It is essentially a surface integral equation formulation. For three-dimensional objects the segmentation is over the entire surface of the object and results in large matrices. Consequently, the solution becomes limited to objects small in terms of the wavelength. The matrix dimension can be reduced by utilizing the symmetry of the geometry (reflection, translation, or rotation). Such symmetries are used extensively in the case of three dimensional objects to reduce the solution time [55], [56].

It is the purpose of this thesis to present techniques which can be used to solve problems associated with bodies which have arbitrary cross-sections, such as plates, squares, and polygons.

Two similar, but different, techniques are used to handle these problems. The first technique utilizes a coordinate transformation (*CTM*). This technique was used previously in studying electromagnetic fields in the presence of arbitrary boundary surfaces [57], [58]. Generally, a mapping function is defined to transform a surface from the object space onto a uniform space which has no cross-sectional discontinuity. In

the new space the surface integrals are reduced to a set of one dimensional integrals along the generating curve of the object, similar to the case of bodies of revolution. The induced currents on the surface of the object are expanded in terms of an angular variable in the new space, as auxiliary currents, similar to the Fourier expansion. The physical currents can be obtained by an inverse transformation of the auxiliary currents to the coordinate of the object.

The second technique which is as an extension of the method used for bodies of revolution, which is adopted to geometries of arbitrary shapes. In this method the physical structure of the object is geometrically represented by two contours, which are defined by intersection of the objects surface with coordinate planes. One is due to the intersection of the $x-z$ plane with surface of the object, and the other, in the cross section, is that with the $x-y$ plane. Hybrid basis functions are selected to model the surface currents by virtue of the current decomposition on the surface. Subsectional expansion functions are selected to model the current in the plane orthogonal to the cross-section, since it results in well conditioned matrices. Entire domain basis functions are selected to represent the circumferential surface currents. Since the coordinate system is not separable, the selected basis functions are not the eigenfunctions of the integral operator, leading to the coupled current modes on the surface. As a result, a finite number of Fourier modes are required to be solved simultaneously, in order to compute their coefficients.

The method of moment is used to solve either formulations numerically. The methods are subsequently applied to study the scattering from geometries such as spheres, finite cylinders, and objects with any polygonal cross-section such as cubes, prisms and plates.

In chapter 2, the formulation for both Electric Field Integral Equation (*EFIE*) and Magnetic Field Integral Equation (*MFIE*), based on Conformal Transformation Method (*CTM*), are given and then the convergence of the solutions and the accuracy of the

results are investigated. The method is subsequently applied to study the scattering properties of conducting bodies of rectangular cross-sections. Representative results, for both near- and far-field quantities are obtained and compared.

In chapter 3, the E - and H - field integral equations are solved directly in the object's physical coordinates. Both formulations are presented and the convergence of the solutions and their accuracy are compared with the *CTM* technique.

In chapter 4, the formulation used for conducting bodies is extended to treat dielectric bodies of arbitrary shape. Five different matrix formulations are presented and the method is subsequently employed to study the scattering properties of different geometries such as spheres, cylinders, and cubes.

In chapter 5, the developed numerical technique is applied to an antenna problem, that is, the radiation from rectangular waveguides. An x -directed dipole is used as a source of excitation and the radiation characteristic of the rectangular waveguide is determined.

Finally, conclusions of the work presented herein are drawn and the future work is suggested in chapter 6.

Chapter 2

Conformal Transformation Method

2.1. Introduction

In electromagnetic scattering problems involving conducting objects surface integral equations are often used to study the far and near field parameters. For three dimensional objects of complex shape the surface patch [34]-[38] or wire grids [30]-[32] are extensively used to model the scattering surface. Techniques such as the moment methods [16] are subsequently used to reduce the integral equations to a system of linear equations, in order to determine the surface currents and the far scattered fields. The matrix dimensions can be reduced by utilizing the symmetry of the geometry by enforcing the reflection, translation, or the rotational symmetry. The rotationally symmetric case have been used in problems involving bodies of revolution to reduce the overall matrix to a number of small matrices of uncoupled azimuthal modes [7].

For arbitrary structures, the basis functions in the moment method are not the eigenfunctions of the integral operator, forcing the current modes to be coupled on the surface. As a result, an infinite number of coupled modes contribute to the scattered field. These current modes are dependent on the wavelength and, in turn to the electrical size of the scatterer. In the Rayleigh and the resonance regions only a few modes are needed to characterize the electromagnetic behavior of the conducting bodies. Therefore, one can obtain a numerical solution to the scattered field by including a finite number of modes.

In the following sections, the E- and H-field integral equations are formulated to investigate the scattering from complex three-dimensional structures. However, rather than utilizing the surface patch, or wire grid modelings, a mapping function is used to model the surface. For a three dimensional object a transformation that maps its surface onto a new one is not feasible in a general sense. Thus, a conformal mapping is used to transform only its cross-section. That is, the object's surface from the x,y,z coordinates is mapped onto a new one in a χ,ξ,z coordinate system. In this manner, only the x,y coordinates are transformed which map the object's cross-section from the $x-y$ plane onto a region outside a circle in the $\chi-\xi$ plane. In this regard the method is similar to one previously applied to two-dimensional scattering [13].

Subsequently, and similar to bodies of revolution, on the object's surface two orthogonal tangent vectors \hat{t} and \hat{s} are defined, Fig. 2.1. The \hat{t} vector is located in a plane normal to the $x-y$ plane, which contains the z -axis. The \hat{s} vector, on the other hand, is in the $x-y$ plane. The surface integral equations are then reduced to a matrix equation by a procedure similar to bodies of revolutions and a use of the moment methods. Specifically, the surface currents are represented by sub-domain basis functions along the vector \hat{t} and by entire domain basis functions in the transformed space along the vector \hat{s} . A matrix equation is then obtained by application of a moment method. However, since the modes are coupled the resulting matrix contains all current modes. The method is thus a generalization of the method used for bodies of revolution (*BOR*).

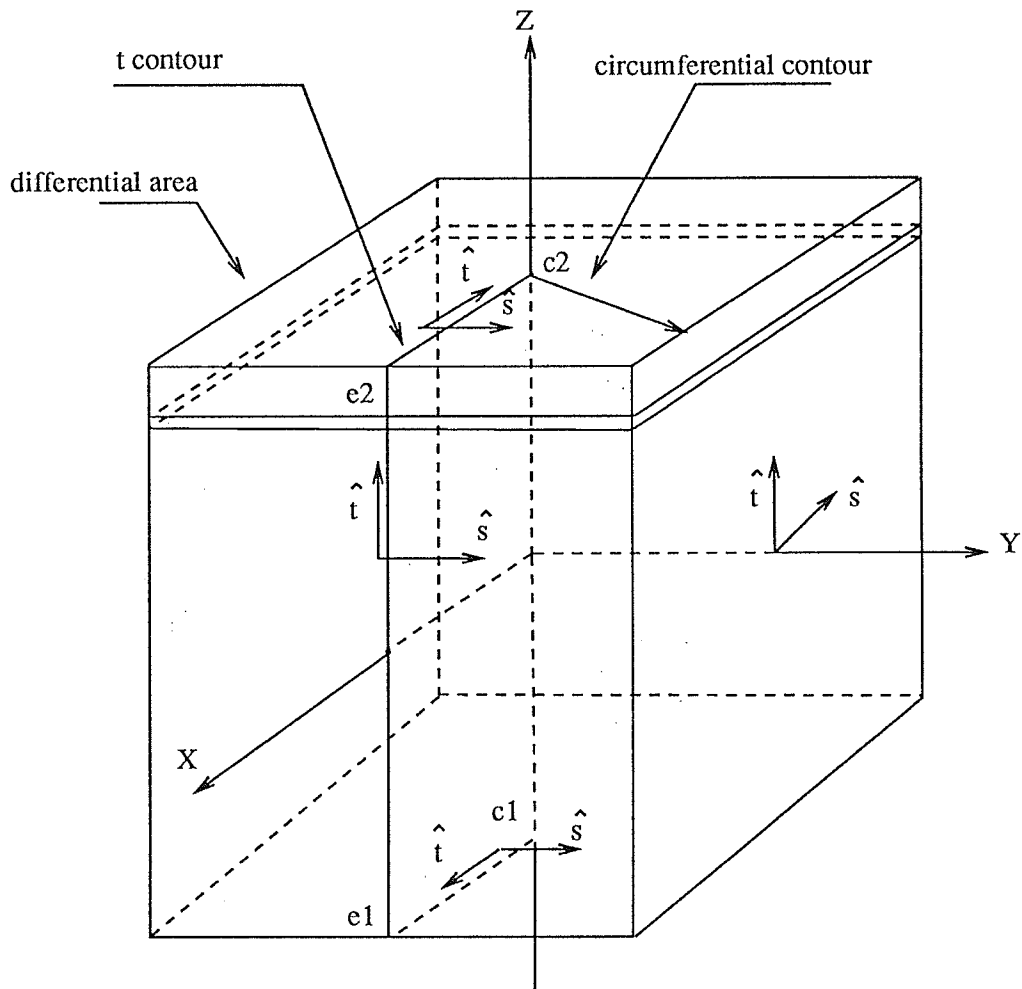


Fig. 2.1 : Coordinate geometry of a conducting cube of side length L .

2.2. E-field formulation

The electric field exterior to an object's surface can be expressed in terms of a vector potential $\mathbf{A}(\mathbf{J})$ and a scalar potential $\phi(\mathbf{J})$ as

$$\mathbf{E}^s = -j\omega\mathbf{A}(\mathbf{J}) - \nabla\phi(\mathbf{J}) \quad (2.1)$$

$$\mathbf{A}(\mathbf{J}) = \mu \iint_S \mathbf{J}(r') \frac{e^{-jkR}}{4\pi R} ds' \quad (2.2)$$

$$\phi(\mathbf{J}) = \frac{1}{\epsilon} \iint_S \sigma \frac{e^{-jkR}}{4\pi R} ds' \quad (2.3)$$

where σ is the surface charge density defined as,

$$\sigma = \frac{-1}{j\omega} \nabla_s \cdot \mathbf{J} \quad (2.4)$$

and R is the distance between the field and source points on S . Enforcing the boundary conditions result in an integro-differential equation for the surface current \mathbf{J} which can be solved numerically.

Now, we consider two orthogonal unit vectors on the object's surface as depicted in Fig. 2.1.

$$\hat{u}_i = \sin \beta \hat{u}_\rho + \cos \beta \hat{u}_z \quad (2.5)$$

$$\hat{u}_s = -\sin \alpha \hat{u}_i + \cos \alpha \hat{u}_j \quad (2.6)$$

where, β is the angle between the unit vector \hat{u}_i and the z -axis, and α is the angle which is used to define the unit vector \hat{u}_s on different portions of the surface contour in the xy plane. For rotationally symmetric cases, this angle, i.e. α , reduces to the az-

azimuthal angle ϕ . The current is defined on the object's surface as

$$\mathbf{J}(\mathbf{r}) = \hat{u}_t J^t(t, \xi) + \hat{u}_s J^s(t, \xi) \quad (2.7)$$

where J^t and J^s are the \hat{t} and \hat{s} directed current components, and defined as

$$J^p = \sum_{n=-\infty}^{\infty} \sum_{j=1}^N a_{nj}^p J_{nj}^p, \quad p = t \text{ or } s \quad (2.8)$$

The constants a_{nj}^p are current coefficients to be determined and J_{nj}^p are the expansion functions defined by

$$\mathbf{J}_{nj}^p = \hat{u}_p f_j(t) e^{jn\xi} \quad (2.9)$$

together with testing functions which have the form

$$\mathbf{W}_{mi}^p = \hat{u}_p f_i(t) e^{-jm\xi} \quad (2.10)$$

In equation (2.7), t represents the arc length along a selected generating curve of the structure. Similar to bodies of revolution $f_i(t)$ is an overlapping triangle basis function which spans the generating curve, n and m are the mode numbers along the vector \hat{s} and ξ is the azimuthal angle measured from the $x-z$ plane in the transformed coordinate system. A substitution of the current expansion (2.7) into (2.1) yields a system of linear algebraic equations which may be written as

$$\sum_{n=-\infty}^{\infty} \sum_{j=1}^N (Z_{mn}^{pq})_{ij} a_{nj}^p = V_{mi}^p, \quad m = 0, \pm 1, \pm 2, \dots \quad (2.11)$$

The elements of the impedance matrix $(Z_{mn}^{pq})_{ij}$ are then computed from

$$(Z_{mn}^{pq})_{ij} = \frac{j\omega}{\eta} \iint_S [\mathbf{W}_{mi}^p \cdot \mathbf{A}(\mathbf{J}_{nj}^q) + \sigma_{mi}^p \phi(\mathbf{J}_{nj}^q)] ds \quad (2.12)$$

where p and q are either t or s which define four partitioned impedance submatrices, $\sigma_{mi}^p = \frac{-1}{j\omega} \nabla_s \cdot \mathbf{W}_{mi}^p$, and V_{mi}^p is the excitation vector defined as

$$V_{mi}^p = \frac{1}{\eta} \iint_s \mathbf{W}_{mi}^p \cdot \mathbf{E}^i ds \quad (2.13)$$

Here, η is the intrinsic impedance of the medium, ∇_s is the surface gradient expressed in the object's coordinate system, and \mathbf{E}^i is the incident field. By definition, the surface gradient is given by

$$\nabla_s = \hat{u}_t \frac{1}{h_1} \frac{\partial}{\partial t} + \hat{u}_s \frac{1}{h_2} \frac{\partial}{\partial s} \quad (2.14)$$

and the surface divergence of a function \mathbf{J} is defined as

$$\nabla_s \cdot \mathbf{J} = \frac{1}{h_1 h_2} \left[\frac{\partial}{\partial t} (h_2 J) + \frac{\partial}{\partial s} (h_1 J) \right] \quad (2.15)$$

where, h_1 and h_2 are the metric coefficients of t and s coordinates and specify the nature of the coordinate system. These metric coefficients may be conveniently identified as a differential length of integration, $dl = h(\xi)d\xi$, for any given line integral. In the selected t and s coordinate system we have

$$h_1 = 1 \quad (2.16)$$

$$h_2^2(\xi) = \left| \frac{dZ}{d\tau} \right|^2 = \left(\frac{dx}{d\xi} \right)^2 + \left(\frac{dy}{d\xi} \right)^2 \quad (2.17)$$

where the parameters given in (2.17) are defined in appendix I. Under the required transformation the basis functions are continuous over the physical boundaries and the transformations along the common boundaries of two adjacent contours are the same, but with different scaling factors. Therefore, the conditions for the continuity of the basis functions are not altered with the transformation. Using the selected basis and weighting functions in (2.9) and (2.10) it can be shown that, the elements of the partitioned sub-matrices $(Z_{mn}^{pq})_{ij}$ are given by

$$\begin{aligned}
(Z''_{mn})_{ij} = & jk^2 \int_0^t dt \int_0^t dt' [cf_i(t) c'f_j(t')(\sin \beta \sin \beta' G_1 \\
& + \cos \beta \cos \beta' G_2) - j \frac{\partial}{\partial t} (cf_i(t)) \frac{\partial}{\partial t'} (c'f_j(t'))G_2] \quad (2.18.a)
\end{aligned}$$

$$\begin{aligned}
(Z''_{mn})_{ij} = & jk^2 \int_0^t dt \int_0^t dt' [cf_i(t) c'f_j(t') \sin \beta' G_3 \\
& - \frac{m}{c} cf_i(t) \frac{\partial}{\partial t'} (c'f_j(t'))G_4] \quad (2.18.b)
\end{aligned}$$

$$\begin{aligned}
(Z''_{mn})_{ij} = & jk^2 \int_0^t dt \int_0^t dt' [cf_i(t) c'f_j(t')(-\sin \beta G_5) \\
& + \frac{n}{c} \frac{\partial}{\partial t} (cf_i(t))c'f_j(t')G_6] \quad (2.18.c)
\end{aligned}$$

$$(Z''_{mn})_{ij} = jk^2 \int_0^t dt \int_0^t dt' cf_i(t)c'f_j(t')(G_7 - \frac{jmn}{cc'} G_8) \quad (2.18.d)$$

where, c is the transformed radius of the object in the new coordinate system, and G 's are defined as

$$G_1 = \int_0^{2\pi} \int_0^{2\pi} F(\xi, \xi') \cos(\phi'(\xi') - \phi(\xi)) d\phi d\phi' \quad (2.19)$$

$$G_2 = \int_0^{2\pi} \int_0^{2\pi} F(\xi, \xi') d\phi d\phi' \quad (2.20)$$

$$G_3 = \int_0^{2\pi} \int_0^{2\pi} F(\xi, \xi') \sin(\phi'(\xi') - \alpha(\xi)) d\phi d\phi' \quad (2.21)$$

$$G_4 = \int_0^{2\pi} \int_0^{2\pi} h(\xi') G(\xi, \xi') L(\xi, \xi') e^{j(n\xi' - m\xi)} d\phi d\phi' \quad (2.22)$$

$$G_5 = \int_0^{2\pi} \int_0^{2\pi} F(\xi, \xi') \sin(\alpha'(\xi') - \phi(\xi)) d\phi d\phi' \quad (2.23)$$

$$G_6 = \int_0^{2\pi} \int_0^{2\pi} h(\xi) G(\xi, \xi') L'(\xi, \xi') e^{j(n\xi' - m\xi)} d\phi d\phi' \quad (2.24)$$

$$G_7 = \int_0^{2\pi} \int_0^{2\pi} F(\xi, \xi') \cos(\alpha'(\xi') - \alpha(\xi)) d\phi d\phi' \quad (2.25)$$

$$G_8 = \int_0^{2\pi} \int_0^{2\pi} G(\xi, \xi') L(\xi, \xi') L'(\xi, \xi') e^{j(n\xi' - m\xi)} d\phi d\phi' \quad (2.26)$$

with,

$$F(\xi, \xi') = h(\xi)h(\xi') G(\xi, \xi') e^{j(n\xi' - m\xi)} \quad (2.27)$$

$$L(\xi, \xi') = \frac{1}{h(\xi)} [\sin^2 \alpha x'_\xi + \cos^2 \alpha y'_\xi] \quad (2.28)$$

$$G(\xi, \xi') = \frac{e^{-jkR}}{kR} \quad (2.29)$$

the parameters given in (2.28) are defined in appendix I, and

$$R = |\mathbf{r} - \mathbf{r}'| = [(\rho(\xi) - \rho'(\xi'))^2 + (z - z')^2 + 2\rho(\xi)\rho'(\xi')(1 - \cos(\phi(\xi) - \phi'(\xi')))]^{\frac{1}{2}} \quad (2.30)$$

The numerical integration of the basis function $f_i(t)$ over the t variable is carried out by a pulse sampling method [7]. That is, selecting $2M$ samples $cf_i(t)$ and it's derivatives are represented by

$$cf_i(t) = \frac{1}{k} \sum_{p=1}^{2M} T_{p+(i-1)2M} \delta(t - t_{p+(i-1)M}), \quad i = 1, 2, \dots, N \quad (2.31.a)$$

$$\frac{d}{dt}(cf_i(t)) = \sum_{p=1}^{2M} T'_{p+(i-1)M} \delta(t - t_{p+(i-1)M}), \quad i = 1, 2, \dots, N \quad (2.31.b)$$

where the specific expressions for T and T' are summerized in appendix II.

Finally, a substitution of (2.31) into (2.18) yields the impedance sub-matrices as

$$(Z_{mn}^{tt})_{ij} = j \sum_{p=1}^{2M} \sum_{q=1}^{2M} [T_p' T_q' (\sin \beta_i \sin \beta_j G_1 + \cos \beta_i \cos \beta_j G_2) - T_p' T_q' G_2] \quad (2.32.a)$$

$$(Z_{mn}^{st})_{ij} = \sum_{p=1}^{2M} \sum_{q=1}^{2M} [T_p' T_q' j(\sin \beta_j G_3) - \frac{m}{kc_i'} T_p' T_q' G_4] \quad (2.32.b)$$

$$(Z_{mn}^{ts})_{ij} = \sum_{p=1}^{2M} \sum_{q=1}^{2M} [T_p' T_q' j(-\sin \beta_i G_5) + \frac{n}{kc_j'} T_p' T_q' G_6] \quad (2.32.c)$$

$$(Z_{mn}^{ss})_{ij} = j \sum_{p=1}^{2M} \sum_{q=1}^{2M} [T_p' T_q' (G_7 - \frac{mn}{k^2 c_i' c_j'} G_8)] \quad (2.32.d)$$

where

$$p' = p + 2M(i - 1) \quad , \quad q' = q + 2M(i - 1) \quad (2.33.a)$$

$$i' = p + M(i - 1) \quad , \quad j' = q + M(i - 1) \quad (2.33.b)$$

2.3. H-field formulation

The magnetic field on the exterior surface of an object can be expressed in terms of it's surface current \mathbf{J} as

$$\hat{n} \times \mathbf{H}^i = \frac{\mathbf{J}(\mathbf{r})}{2} - \frac{1}{4\pi} \int_S \hat{n} \times \mathbf{J}(\mathbf{r}') \times \nabla' \left(\frac{e^{-jkR}}{R} \right) ds' \quad (2.34)$$

where, \mathbf{H}^i is the incident magnetic field, \hat{n} is the unit vector normal to the surface S defined as $\hat{n} = \hat{u}_s \times \hat{u}_t$, and ∇' is the gradient operator defined in the object's source coordinates. A substitution of (2.7) into (2.34) and applying the moment methods, one obtain a matrix equation of the form

$$\sum_{n=-\infty}^{\infty} \sum_{j=1}^N (Y_{mn}^{pq})_{ij} a_{nj}^p = I_{mi}^p \quad m = 0, \pm 1, \pm 2, \dots \quad (2.35)$$

where p, q are either t or s which define four partitioned admittance submatrices $(Y_{mn}^{pq})_{ij}$, a_{nj}^p are current coefficients to be determined, and I_{mi}^p are the excitation vectors defined as,

$$I_{mi}^p = \int_{\mathcal{S}} \mathbf{W}_{mi}^p \cdot (\hat{\mathbf{n}} \times \mathbf{H}^i) ds \quad (2.36)$$

The element of the partitioned submatrices Y_{mn}^{pq} can be written as

$$(Y_{mn}^{tt})_{ij} = G_9 \int_0^t c f_i(t) f_j(t) dt - k^3 \int_0^t c f_i(t) dt \int_0^t c' f_j(t') dt' \\ [\cos \beta' (c' G_{10} - c G_{12}) - (z' - z) \sin \beta' G_{15}] \quad (2.37.a)$$

$$(Y_{mn}^{st})_{ij} = -k^3 \int_0^t c f_i(t) dt \int_0^t c' f_j(t') dt' [c' \sin \beta \cos \beta' G_{13} \\ - c \sin \beta' \cos \beta G_{14} - (z' - z) \sin \beta \sin \beta' G_{15}] \quad (2.37.b)$$

$$(Y_{mn}^{ts})_{ij} = -k^3 \int_0^t c f_i(t) dt \int_0^t c' f_j(t') dt' (z' - z) G_{16} \quad (2.37.c)$$

$$(Y_{mn}^{ss})_{ij} = G_9 \int_0^t c f_i(t) f_j(t) dt - k^3 \int_0^t c f_i(t) dt \int_0^t c' f_j(t') dt' \\ [\cos \beta (c' G_{11} - c G_{17}) - (z' - z) \sin \beta G_{18}] \quad (2.37.d)$$

where;

$$G_9 = \frac{1}{2} \int_0^{2\pi} h(\xi) e^{j(n\xi - m\xi)} d\xi \quad (2.38)$$

$$G_{10} = \frac{1}{4\pi} \int_0^{2\pi} \int_0^{2\pi} p(\xi, \xi') \rho'(\xi') \cos(\phi'(\xi') - \alpha(\xi)) d\xi d\xi' \quad (2.39)$$

$$G_{11} = \frac{1}{4\pi} \int_0^{2\pi} \int_0^{2\pi} p(\xi, \xi') \rho(\xi) \cos(\phi(\xi) - \alpha(\xi)) d\xi d\xi' \quad (2.40)$$

$$G_{12} = \frac{1}{4\pi} \int_0^{2\pi} \int_0^{2\pi} p(\xi, \xi') \cos(\phi'(\xi') - \alpha(\xi)) d\xi d\xi' \quad (2.41)$$

$$G_{13} = \frac{1}{4\pi} \int_0^{2\pi} \int_0^{2\pi} p(\xi, \xi') \rho'(\xi') \sin(\phi'(\xi') - \phi(\xi)) d\xi d\xi' \quad (2.42)$$

$$G_{14} = \frac{1}{4\pi} \int_0^{2\pi} \int_0^{2\pi} p(\xi, \xi') \rho(\xi) \sin(\phi'(\xi') - \phi(\xi)) d\xi d\xi' \quad (2.43)$$

$$G_{15} = \frac{1}{4\pi} \int_0^{2\pi} \int_0^{2\pi} p(\xi, \xi') \sin(\phi'(\xi') - \phi(\xi)) d\xi d\xi' \quad (2.44)$$

$$G_{16} = \frac{1}{4\pi} \int_0^{2\pi} \int_0^{2\pi} p(\xi, \xi') \sin(\alpha'(\xi') - \alpha(\xi)) d\xi d\xi' \quad (2.45)$$

$$G_{17} = \frac{1}{4\pi} \int_0^{2\pi} \int_0^{2\pi} p(\xi, \xi') \rho(\xi) \cos(\alpha'(\xi') - \phi(\xi)) d\xi d\xi' \quad (2.46)$$

$$G_{18} = \frac{1}{4\pi} \int_0^{2\pi} \int_0^{2\pi} p(\xi, \xi') \cos(\alpha'(\xi') - \phi(\xi)) d\xi d\xi' \quad (2.47)$$

with,

$$p(\xi, \xi') = h(\xi)h(\xi')G(\xi, \xi') e^{j(n\xi' - m\xi)} \quad (2.48)$$

$$G(\xi, \xi') = \frac{1 + jkR}{k^3 R^3} e^{-jkR} \quad (2.49)$$

also, $R = |\mathbf{r} - \mathbf{r}'|$ as defined in equation (2.30). A substitution of (2.31) into (2.37) yields the admittance submatrices as

$$(Y_{mn}^{pq})_{ij} = \sum_{n=-\infty}^{\infty} \sum_{p=1}^{2M} T_{p+2M(i-2)} \sum_{q=1}^{2M} T_{q+2M(j-1)} (y_{mn}^{pq})_{vv'} \quad , \quad (2.50.a)$$

$$\begin{aligned} v' &= p+M(i-1) \\ v &= q+M(j-1) \end{aligned} \quad (2.50.b)$$

where the elements of y_{mn}^{pq} are given as

$$(y_{mn}^{tt})_{ij} = \frac{G_9}{k^2 c_i d_i} - \cos \beta_j (kc_j G_{10} + kc_i G_{11}) - k(z_j - z_i) \sin \beta_j G_{12} \quad (2.51.a)$$

$$(y_{mn}^{st})_{ij} = kc_j \sin \beta_i \cos \beta_j G_{13} - kc_i \sin \beta_j \cos \beta_i G_{14} - k(z_j - z_i) \sin \beta_i \sin \beta_j G_{15} \quad (2.51.b)$$

$$(y_{mn}^{ts})_{ij} = k(z_j - z_i) G_{16} \quad (2.51.c)$$

$$(y_{mn}^{ss})_{ij} = \frac{G_9}{k^2 c_i d_i} - \cos \beta_i (kc_j G_{11} - kc_i G_{17}) + k(z_j - z_i) \sin \beta_i G_{18} \quad (2.51.d)$$

2.4. Plane wave excitation and far field

For an arbitrary incident plane wave defined as

$$\mathbf{E}^i = \hat{u}_q k \eta e^{-j\mathbf{k}_i \cdot \mathbf{r}} \quad (2.52.a)$$

$$\mathbf{H}^i = \mathbf{k} \times \hat{u}_q e^{-j\mathbf{k}_i \cdot \mathbf{r}} \quad (2.52.b)$$

The elements of the excitation matrix for the case of the E-field integral equation are given by,

$$V_{mi}^{pq} = k \int_0^t dt c f_i(t) \int_0^{2\pi} h(\xi) (\hat{u}_p \cdot \hat{u}_q) e^{-j(\mathbf{k}_i \cdot \mathbf{r} + m\xi)} d\xi \quad (2.53)$$

and for the H-field integral equation are expressed as

$$I_{mi}^{pq} = k \int_0^t dt \, cf_i(t) \int_0^{2\pi} h(\xi) (\hat{u}_p \times \hat{n}) \cdot (\mathbf{k}_i \times \hat{u}_q) e^{-j(\mathbf{k}_i \cdot \mathbf{r} + m\xi)} d\xi \quad (2.54)$$

where p is either t or s , and q is the polarization of the incident wave. Once the surface current \mathbf{J} is computed, the far field components E_θ and E_ϕ at the far field point (r_r, θ_r, ϕ_r) can be determined as

$$E_q = \frac{-j\omega\mu}{4\pi r_r} e^{-jk_r r_r} F_q(\theta_r, \phi_r) \quad (2.55)$$

where

$$F_q(\theta_r, \phi_r) = \int_s (\mathbf{J} \cdot \hat{u}_q) e^{-j\mathbf{k}_r \cdot \mathbf{r}} ds \quad (2.56)$$

Here k_r is the propagation vector of the plane wave arriving from the field point, λ is the wavelength, r_r is the distance between the origin and the measurement point, and \hat{u}_q is the polarization of the receiving electric dipole at the far field measurement point. The scattering vectors which relate the surface current J to the field point in the free space are defined as

$$R_{ni}^{pq} = k \int_0^t cf_i(t) dt \int_0^{2\pi} h(\xi) (\hat{u}_p \cdot \hat{u}_q^r) e^{j(-\mathbf{k}_r \cdot \mathbf{r} + n\xi)} d\xi \quad (2.57)$$

which gives F_q in the form

$$F_q(\theta_r, \phi_r) = \sum_{n=-\infty}^{\infty} \sum_{j=1}^N R_{ni}^{pq} a_{nj}^p \quad (2.58)$$

with these definitions the elements of R_{ni}^{pq} are given by

$$R_{ni}^{t\theta} = \sum_{p=1}^{2M} T_{p+2M(I-1)} [\sin \beta_i \cos \theta_r (\cos \phi_r G_{20} + \sin \phi_r G_{21}) - \cos \beta_i \sin \theta_r G_{19}] \quad (2.59.a)$$

$$R_{ni}^{s\theta} = \sum_{p=1}^{2M} T_{p+2M(I-1)} [-\cos \theta_r (\cos \phi_r G_{23} - \sin \phi_r G_{22})] \quad (2.59.b)$$

$$R_{ni}^{t\phi} = \sum_{p=1}^{2M} T_{p+2M(I-1)} [\sin \beta_i (\cos \phi_r G_{21} - \sin \phi_r G_{20})] \quad (2.59.c)$$

$$R_{ni}^{s\phi} = \sum_{p=1}^{2M} T_{p+2M(I-1)} [\cos \phi_r G_{22} + \sin \phi_r G_{23}] \quad (2.59.d)$$

in which by selecting

$$f(\rho, \xi) = h(\xi) e^{jn\xi} e^{-jk_r \cdot r(\xi)} \quad (2.60)$$

the functions G 's are given by

$$G_{19} = \int_0^{2\pi} f(\rho, \xi) d\xi \quad (2.61)$$

$$G_{20} = \int_0^{2\pi} f(\rho, \xi) \cos \phi(\xi) d\xi \quad (2.62)$$

$$G_{21} = \int_0^{2\pi} f(\rho, \xi) \sin \phi(\xi) d\xi \quad (2.63)$$

$$G_{22} = \int_0^{2\pi} f(\rho, \xi) \cos \alpha(\xi) d\xi \quad (2.64)$$

$$G_{23} = \int_0^{2\pi} f(\rho, \xi) \sin \alpha(\xi) d\xi \quad (2.65)$$

Once the scattered field is determined the scattering cross section can be computed according to

$$\frac{\sigma^{pq}}{\lambda^2} = \frac{1}{4\pi^3} \left| \frac{2\pi r_r E_{\rho q}^s(\mathbf{J})}{\eta} \right|^2 \quad (2.66)$$

2.5. Transformation

For objects of rectangular cross-section, the required transformation is given by [59]

$$\frac{dZ}{d\zeta} = B \frac{[(\zeta^2 - a^2)(\zeta^2 - a^{-2})]^{\frac{1}{2}}}{(1 + \zeta^2)^2} \quad \begin{array}{l} Z = x + iy \\ \zeta = u + iv \end{array} \quad (2.67)$$

which transform the region outside the cross-section of the scatterer in the Z -plane into the upper half of the ζ -plane, with the boundary transforming into the real axis. A transformation of the form $\zeta = -\tan\frac{\tau}{2}$, with $\tau = \chi + i\xi$ transforms the half-plane region into a (χ, ξ) region outside a circle with the boundary itself being the circle. In the above, B is a constant which depends upon the scale and orientation of the rectangle. The required metric coefficient of the transformation for the rectangular cross-section has the form of

$$\left| \frac{dZ}{d\tau} \right| = h(\xi) = \left| \frac{b}{2l} (2 + 4 \cos^2 2\alpha - 8 \cos 2\alpha \cos 2\xi + 2 \cos 4\xi)^{\frac{1}{4}} \right| \quad (2.68)$$

where, α is a constant which depends on the width to length ratio of the rectangle and $2b$ is the width of the rectangle. As the cross-section of the scatterer deviates from a square, the parameter α changes from its initial value of 45° for a square to zero for a line segment. This corresponds to the presence of the second harmonic namely, 2ξ in the scale factor which relates the geometrical properties of the coordinates (χ, ξ) and the behavior of the solution. In terms of the transformation coordinate the cross-sectional contour of the rectangle is defined by $\chi = 0$ for $0 \leq \xi \leq 2\pi$ and its coordinates may be obtained from

$$x = \frac{b}{2l} \left[\cos \xi + \sum_{m=1}^{\infty} D_m \cos (2m - 1)\xi \right] \quad (2.69.a)$$

$$y = \frac{b}{2l} \left[\sin \xi - \sum_{m=1}^{\infty} D_m \sin (2m - 1)\xi \right] \quad (2.69.b)$$

$$\rho(\xi) = [x(\xi)^2 + y(\xi)^2]^{\frac{1}{2}} \quad (2.69.c)$$

$$\phi(\xi) = \tan^{-1} \left[\frac{y(\xi)}{x(\xi)} \right] \quad (2.69.d)$$

Here, l is a constant and is defined as,

$$l = E - f^2 Q \quad , \quad f^2 = 1 - f^2 \quad , \quad f = \sin \alpha \quad (2.70)$$

and f is the root of the following transcendental equation

$$(E - f^2 Q)a = (E' - f^2 Q')b \quad (2.71)$$

where, $2a$ is the length of the rectangle and other terms are in the forms

$$E = \int_0^{\frac{\pi}{2}} \sqrt{1 - f^2 \sin^2 \xi} \, d\xi \quad (2.72.a)$$

$$E' = \int_0^{\frac{\pi}{2}} \sqrt{1 - f'^2 \sin^2 \xi} \, d\xi \quad (2.72.b)$$

$$Q = \int_0^{\frac{\pi}{2}} \frac{d\xi}{\sqrt{1 - f^2 \sin^2 \xi}} \quad (2.72.c)$$

$$Q' = \int_0^{\frac{\pi}{2}} \frac{d\xi}{\sqrt{1 - f'^2 \sin^2 \xi}} \quad (2.72.d)$$

The constants D_m are defined as

$$D_m = -\frac{a_m}{2m-1} \quad (2.73)$$

and a_m are given in terms of Legendre polynomials as

$$a_0 = 1 \quad a_1 = -\mu \quad , \mu = \cos 2\alpha \quad (2.74.a)$$

$$a_m = P_m(\mu) - 2\mu P_{m-1}(\mu) + P_{m-2}(\mu) \quad (2.74.b)$$

or can be obtained from the recursive relation given by

$$(m+1)a_{m+1} - (2m-1)\mu a_m + (m-2)a_{m-1} = 0. \quad (2.74.c)$$

2.6. Numerical Results

Numerical integration techniques such as the Gauss Quadrature, composite Simpson and Trapezoidal rules were selected for better modeling of the object's surface and in turns to investigate the numerical error which arises due to the lack of convergence of the solution [60]. The simplest modeling strategy is the utilization of a composite quadrature formulae which divides the integration interval into subintervals, and applies the Simpson or Trapezoidal rules on each pair of consecutive subintervals. This type of integration is more convenient for techniques such as surface patch modeling. The second quadrature technique is the Gauss quadrature method which employs unequally spaced optimal points, determined by properties of the orthogonal polynomials.

The most widely applied quadrature formulas are those which approximate the integral by a linear combination of weighted functions as

$$\iint f(\xi, \xi') d\xi d\xi' = \sum_{l=1}^N \sum_{k=1}^M W_l W_k f(\xi_l, \xi_k) \quad (2.75)$$

The integration of the ξ dependent line integrals are carried out by selecting Trapezoidal rule over m subintervals, Simpson's rule over $2m$ subintervals, and the Gauss quadrature technique. Table 2.1 and 2.2 summarize sample results obtained for a conducting square plate of thickness $t = 0.0317\lambda$ and cross section $A = 1.0\lambda^2$, for a normal incident plane wave at broadside. The computed results indicate that a reasonable accuracy can be reached by selecting at least 40 sample points. The numerical results of the scattered field obtained from Simpson and Trapezoidal rules overshoot by the selection of 40 sample points. This is due to improperly locating the sample points at the corners of the plate, where the surface current is singular. This study leads to the selection of the Gauss quadrature method due to the faster convergence of line integrals and better solution stabilities at lower frequencies.

The integration along the t -coordinate of the surface current ($f_i(t)$) is carried out by utilizing a trapezoidal integration technique. To improve the accuracy, each triangle function is simulated by at least four pulses or more. A study was conducted to investigate the accuracy of the purposed numerical integration scheme along the generating curve, and also the number of linear basis functions required to represent the t -directed surface current. To improve the accuracy, for a fixed length of the t -contour per wavelength, one may increase the number of segmentations, subject to the round off error. This will increase the size of the moment matrix and subsequently the computation time. Alternately, the number of pulses that represent the triangle function can be increased rather than the number of linear functions. As a result, the t -directed surface current can be modeled by a fixed number of triangular functions per wavelength, which sets up a criteria for the current sampling selections. However, increasing the number of pulses increases the computation time of the matrix elements. On the other

Table 2.1

<i>NIP</i>	10	20	30	40	50	60
Gauss Quad	9.0471	9.1444	9.9144	10.050	10.191	10.263
Simp's Rule	8.213	9.223	9.445	10.884	10.508	10.547
Trap's Rule	8.608	9.182	10.103	10.698	10.534	10.631

Table 2.1 : Radar cross-section of a square plate of size $L = 1.0\lambda$ and $t = 0.03\lambda$ for modes = 1,2,3, number of points on the generating curve = 13, number of pulses for $f_i(t) = 4$.

Table 2.2

<i>NIP</i>	10	20	30	40	50	60
Gauss Quad	-20.431	-18.601	-17.230	-16.418	-16.195	-16.044
Simp's Rule	-21.845	-17.120	-16.162	-15.942	-15.466	-15.381
Trap's Rule	-20.737	-16.746	-15.942	-15.761	-15.356	-15.302

Table 2.2 : Same as table 2.1 except $L = 0.2\lambda$.

hand, it results in a smaller matrix size, and also leads to a better representation of curved surfaces by small piecewise segments.

In order to examine the dependence of the solution accuracy on the number of pulses, the case of a conducting cube of size $L = 0.75 \lambda$ is considered. The cube is illuminated by an axially incident plane wave polarized along the x -axis, and the computed patterns are illustrated in Fig. 2.2. The number of integration points along the \hat{s} vector and also the number of linear basis function are kept constant. However, each triangle was modeled by different number of pulses along the generating curve and a summary of the results are given in table 2.3. The generating curve was subdivided according to the required number of pulses. As shown in Fig 2.2, in either plane, the solution accuracy is poor with four pulses, but improves initially by increasing the number of pulses until 8 pulses, and remains unchanged there after.

Table 2.3

<i>NP</i>	<i>No of triangles</i>	<i>No of pulses</i>	<i>No of Gauss</i>	<i>CPU* (sec.)</i>
19	8	4	40	53.
28	8	6	40	107.
37	8	8	40	172.
46	8	10	40	245.

Table 2.3. Parameters used in computing the back scattering of a cube of size $L = 0.75 \lambda$ in Fig. 2.2. The CPU times are given for the Amdahl main frame. * not an optimized value.

The present computations show that the solution accuracy can be improved by either increasing the number of pulses per triangle, or by increasing the number of basis functions. In order to select four pulses to represent each triangle there should be at least 10 sample points per wavelength, or the total sample points NP may be obtained from

$$NP = \frac{10 t_{\max}}{\lambda} + 1 \quad (2.76)$$

For instance, dividing the generating curve by 12 subsegment, the number of linear expansion function, i.e. triangular functions, will be equal to five if 4 pulses are selected. Their number will reduce to three triangular functions if they are simulated by 6 pulses.

The above formulation together with the transformation relationships reduced the integral equation to a matrix equation for the current coefficients. The procedure used in these steps is similar to that used for bodies of revolution [7] and omitted here for brevity. However, the transformation introduces the metric coefficient $h(\xi)$ into the integrals involving the functions G . Since $h(\xi)$ is a transcendental function, the selected entire domain functions in the ξ -coordinate are not orthogonal and, consequently due to their coupling the matrix equation does not separate for individual modes. In other words, the resulting matrix involves all modes of the ξ -coordinate. Thus, in contrast to bodies of revolution where one solves several small matrices for individual modes n , in the present case one has to handle a large matrix involving all the modes. In the following sub-sections we investigate the consequences of such a mode coupling to the solution accuracy and provide a few representative results.

To illustrate the versatility and the accuracy of the formulation, it was first applied to rotationally symmetric objects such as spheres and finite cylinders [61], [62].

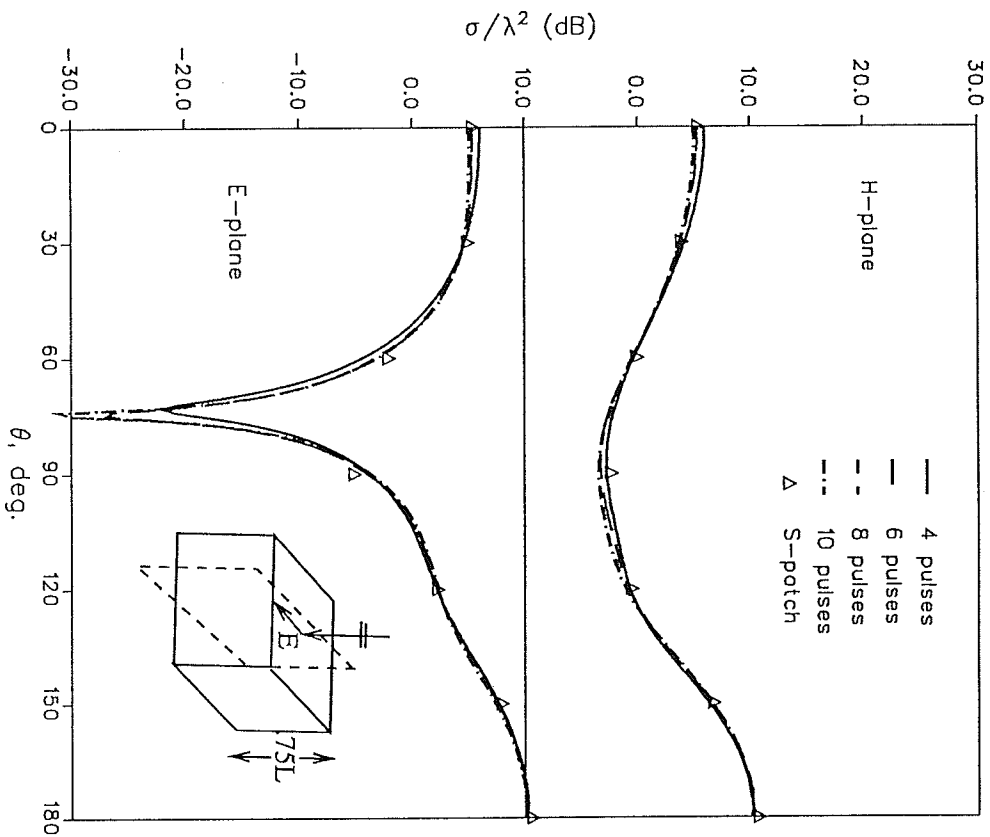


Fig. 2.2 : Bistatic scattering pattern of a conducting cube of $L/\lambda = .75$ for a normal incident plane wave.

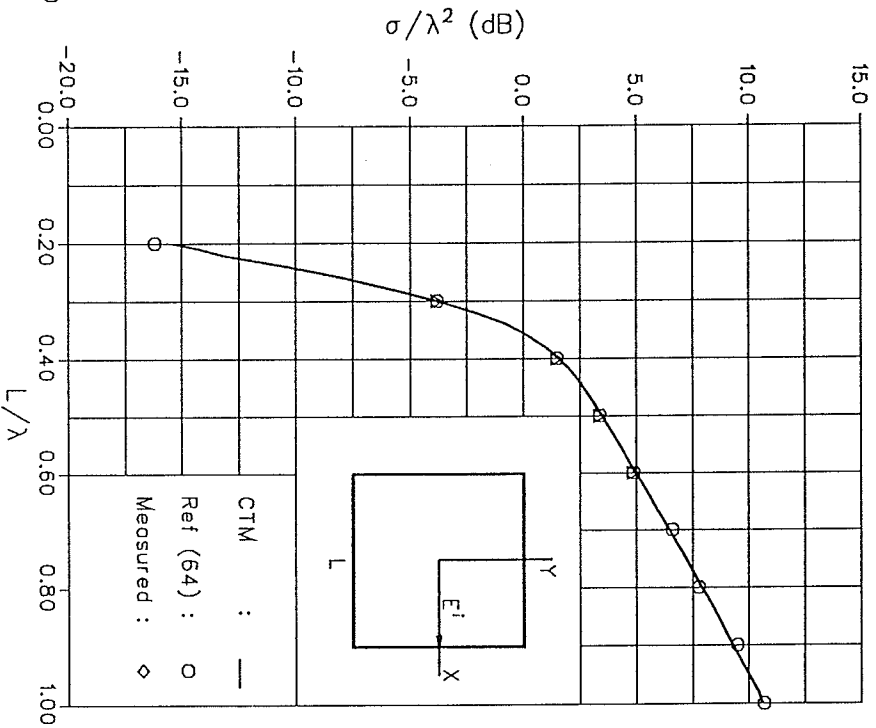


Fig. 2.3 : Back scattering cross-section of a conducting square plate of thickness $t=0.3017\lambda$ for a normal incident plane wave.

The results were compared with analytic and numerical results of computer codes based on a formulation for bodies of revolution to examine the accuracies. Upon obtaining satisfactory results for these special cases, it was then applied to more complex structures such as square plates and cubes.

2.6.1. Objects with square cross-section

The required transformation for the objects of square cross-section is given by [63]

$$\frac{dZ}{d\tau} = \frac{b}{2l} (\cos 2\tau)^{\frac{1}{2}}, \quad \tau = \chi + i \xi \quad (2.77)$$

which gives a metric coefficient of the form

$$h(\xi) = 2c (\sin^2 \alpha - \sin^2 \xi)^{\frac{1}{2}} \quad (2.78)$$

where $c = \frac{b}{2l}$, $2b$ is the side of the square, $l = 0.423607$ is a constant and $\alpha = 45^\circ$ for the square cross section. In generating the coordinate points x and y and their derivatives with respect to ξ , 6 and 8 terms were found to be sufficient in (2.69) to obtain a 3 digit of accuracy. These series converge rather rapidly and in turns show the perturbation of square cross sections from bodies of circular cross-section.

Fig. 2.3 depicts the back scattering cross-section of a square plate of thickness 0.0317λ and a side length of $1. \lambda$ at the normal incidence from broadside. For this geometry, numerical results were obtained by selecting five triangular functions to represent the currents along the t -direction each of which were simulated by four impulses. In the s -direction up to six Fourier terms in the variable ξ were selected. But, it was found that only $n = 1$ term was sufficient to give satisfactory results. The computed results were compared with sinusoidal reaction formulation of Wang [64]. It was also found that for the selected normal incidence the odd modes were dominant. Since

the modes are coupled, with five triangular functions and six Fourier terms, the resulting matrix is a 60X60 matrix. However, because only the $n = 1$ term was dominant, by neglecting all coupling terms the ratio of $n = 1$ to $n = 3$ terms was calculated to be 0.06. It reduced to 0.02 when all coupling terms were included. Consequently, using a single term, i.e. $n = 1$ mode, gave results in good agreement with those of Wang [64].

The cube is one of the important basic geometries and is investigated next. Its scattering cross section for various sizes are shown in Fig 2.4. The computed results are compared with the surface patch modeling of Yaghjian [66] and measured values of Cotes extracted from the same paper. The integration along the circumference of all given examples are carried out by selecting a sixty point Gauss quadrature along the \hat{s} -vector, and the triangular functions are represented by four pulses.

Figs 2.2 and 2.4.a show the bistatic scattering patterns of cubes having base areas of $A = 0.5625 \lambda^2$ and $2.25 \lambda^2$. The incident field is an x -polarized plane wave and the t -directed current is modeled by nine and fourteen triangular functions for each set. It was found that, the first mode, $n = 1$, generates numerical results in the principle planes which are in excellent agreement with the reported results. However, in any other plane such as the $\phi = 45^\circ$ plane, at least $n = 1,2,3$ modes are needed for the solution to converge. The significance of the coupling modes can be found by comparing the magnitude of the current coefficients of the first mode with those of the higher order ones. Table 2.4 summarizes the selected current coefficients of the same cube, size $L = 1.5\lambda$, obtained in the 45° plane.

Table 2.4

J^p	$n = 1$	$n = 2$	$n = 3$	$n = 4$	$n = 5$
\hat{t}_{c1}	3.012671	0.07023049	1.215371	0.06502385	0.5079499
\hat{t}_{e1}	3.264293	0.03016119	1.181672	0.22739110	2.1409570
\hat{t}_{e2}	3.783195	0.49287900	3.387275	0.46566710	1.2284570
\hat{t}_{c2}	3.051406	0.10167890	0.919404	0.09412193	0.4678771
\hat{s}_{c1}	0.621875	0.00710966	0.551912	0.04258902	0.0399983
\hat{s}_{e1}	0.383892	0.14780400	2.809430	0.37489670	0.1001972
\hat{s}_{e2}	4.864019	0.12193560	2.347867	0.31822910	2.3467800
\hat{s}_{c2}	1.211659	0.03470639	0.4284188	0.04245604	0.1997056

Table 2.4. Magnitude of current coefficients (c-center, e-edge defined in Fig. 1.) of a conducting cube of size $L = 1.5 \lambda$ for modes = 1,2,3,4,5, No of points on the generating t curve = 31, No of pulses for $f_i(t) = 4$, No of integration points for Gauss quadrature for G functions = 60.

Two observations can be made. One is the existence of the mode coupling between the even and the odd modes, and the other is the effect of the off diagonal terms on the solution. An extensive study of the current coefficients reveals that, for the selected incident field, odd modes are dominant and couple strongly on the object's surface. The order of the coefficient magnitudes for $n = 1$ and $n = 3$ modes are the same. But, decreases approximately by a factor of five for the next higher odd mode ($n = 5$). It is found that for an axially incident wave the contribution of the even modes to the scattered field is insignificant. This effect is primarily due to the excitation which does not generate the even modes as is evident from the magnitude of their coefficients. The ratio of the current coefficients magnitudes for the $n = 2$ and $n = 1$ modes is less than 0.07.

The significance of the mode coupling was studied by solving the problem using both full and the diagonal matrices. It was observed that by neglecting the off diagonal elements the change in the magnitude of the odd mode coefficients, i.e. Z_{11} is less than

one percent of that of a full matrix solution. On the other hand, the magnitudes of the even modes changed drastically. The order of change was as much as 10 times their magnitudes. In this sense, retaining only the diagonal elements of the operator is not sufficient, and the basis functions do not approach asymptotic forms of the eigenfunctions of the integral operators. Only, for small size objects, i.e., less than 1λ in size, that the diagonal elements replicate the full matrix results with reasonable accuracy, thus offering time reduction in the required computations.

The dependence of the mode coupling on the size of the object for square cross-sections, was investigated by selecting larger cube sizes. Figs. 2.4.b and 2.4.c show the scattering patterns of cubes having base areas of $A = 9\lambda^2$ and $25\lambda^2$. To generate the first set, twenty nine triangular basis functions were selected, and the second sets were generated by utilizing forty nine linear basis functions. Each triangle was modeled by four impulses. A comparison of the generated results with the reported ones in the literature showed that the contribution of the first mode, $n = 1$, is adequate for the selected incident field. However, extra modes were included to verify the convergence and insure the solution accuracy. Each pattern was generated by including additional modes, i.e., $n = 2,3$, and as one can observe, bistatic patterns obtained using $n = 1,2,3$ modes have generated numerical results in close agreements with the reported data. Thus for a normal incidence of the plane wave the mode coupling is not significant and results can be obtained accurately using the first two to three modes.

The effect of coupling of the modes and their contribution to the surface current was also studied. Fig. 2.5 shows the magnitudes of each mode along the central lines on top surface of a square plate of 1.0λ in size and thickness of 0.0317λ . The current modes are scaled by the transformed radius of the square and a spline method, with continuous second derivatives, is used between the sample points. Again, the first mode, $n = 1$ has the largest magnitudes and the higher order modes decrease rapidly in magnitude. A comparison of the results in Fig. 2.5 shows that the current distributions

follow the edge behavior consistent with incident wave polarization.

As a final example, Fig. 2.6 depicts the back scattering cross-section of a conducting rectangular box of square cross-section having a base area of $1. \lambda^2$ and height 0.5λ , for the normal incidence on the top surface. Here, nine triangular functions in the t -direction were selected. Again, $n = 1$ mode was found to be sufficient to give results in good agreement, for both E- and H-field formulations, with those of Tsai [65], obtained using a surface patch modeling.

2.6.2. Rectangular prism

In order to study the effect of mode coupling as a result of the surface perturbation from a circle, the object's cross-sectional contour was changed to a rectangular shape with an aspect ratio of 0.5.

Fig. 2.7 illustrates the back scattering cross-section of a rectangular plate, $L \times 0.5L$ and thickness, $t = 0.0317\lambda$ illuminated by both x - and y -polarized plane waves. The transformation constants for this geometry are $l = 0.2843074$, and $\alpha = 35.95625^\circ$, and 10 terms in (2.69) were adequate to give the coordinate points with 4 figures of accuracy. The back scattering data were obtained by selecting three expansion functions each modeled by six impulses to represent the \hat{t} -current such that the edge current was modeled by a nonvanishing half-triangle. The generating curve was selected along the width of the rectangle in order to minimize the number of linear basis functions needed to model the \hat{t} -directed current. Such a choice results in smaller size submatrices for each current mode and leads to a substantial reduction in the computer time to fill the elements of the matrix and its solution. The computed results are compared with the surface patch technique of Tsai [65]. For the selected cross-section the first mode reasonably replicates the back scattering cross-section for the y -polarized incident wave. However, it fails to generate satisfactory results for the

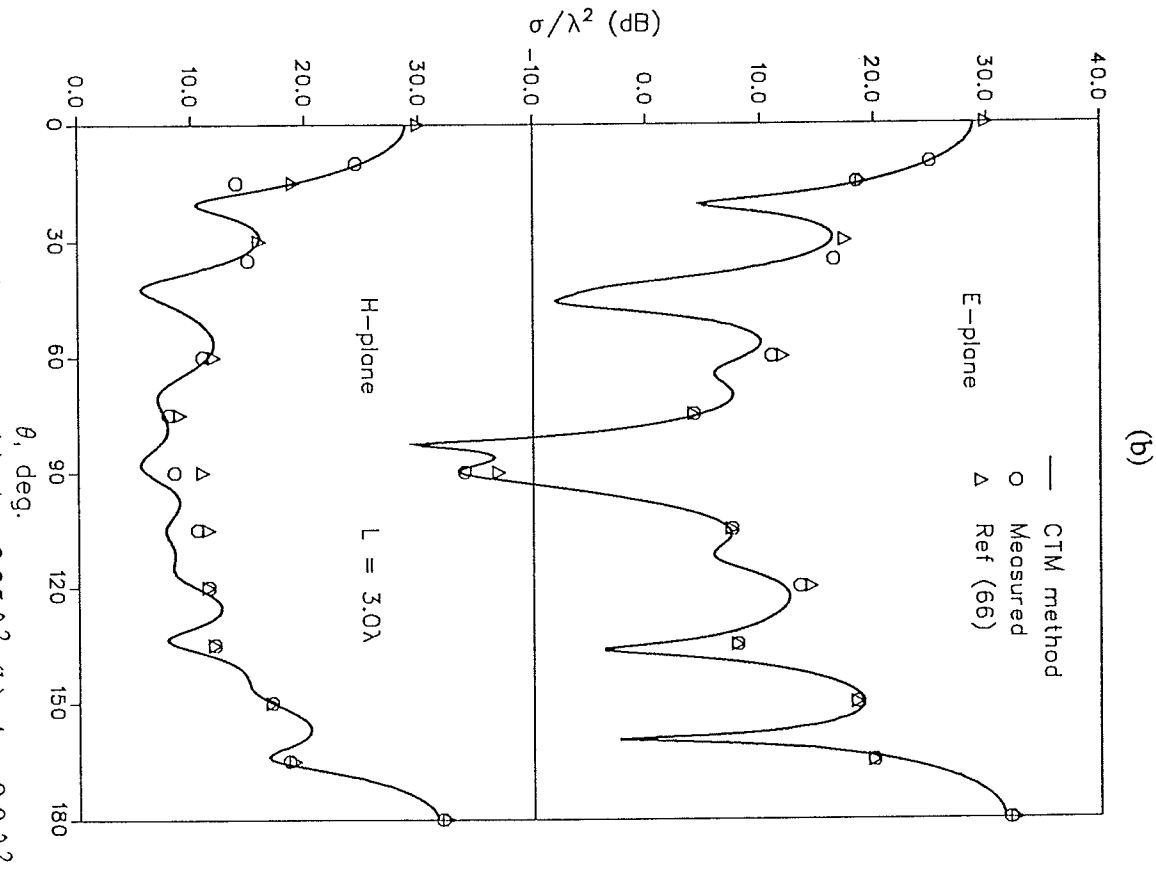
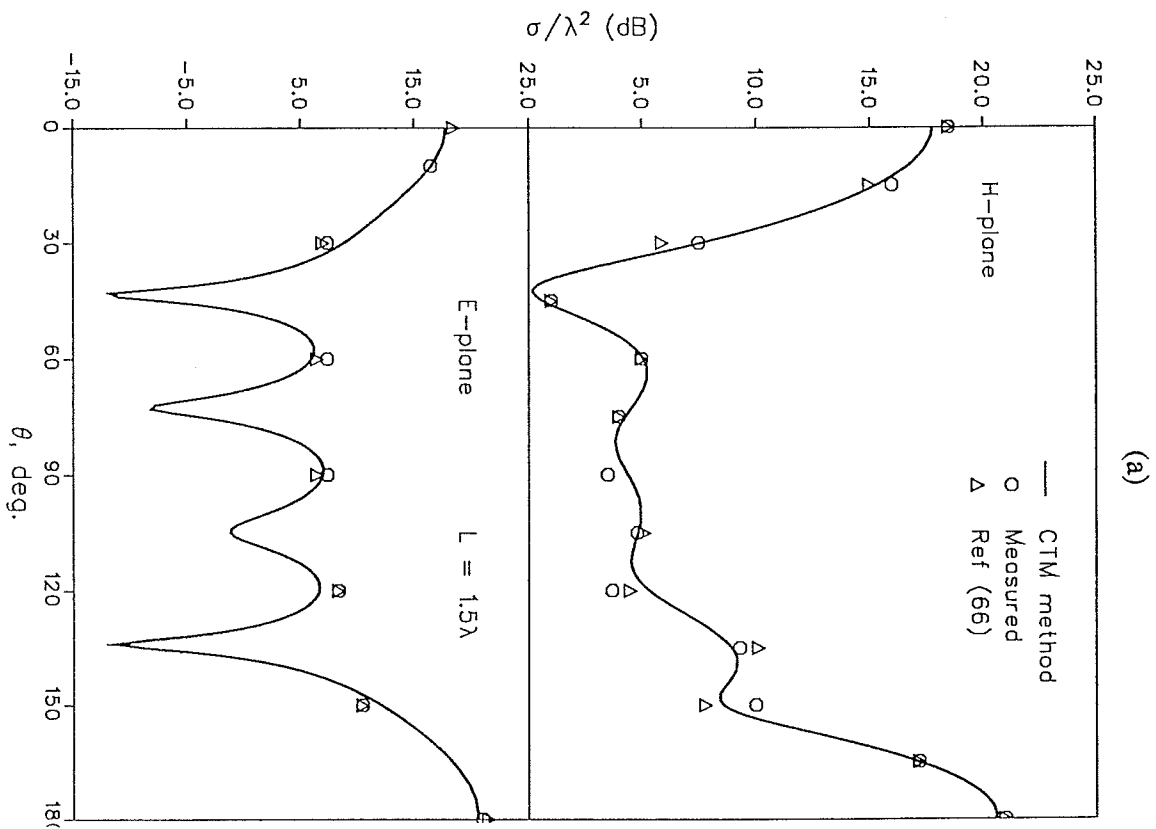


Fig. 2.4 : Bistatic scattering patterns of a conducting cube for a normal incident plane wave, (a). $A = 2.25 \lambda^2$, (b). $A = 9.0 \lambda^2$.

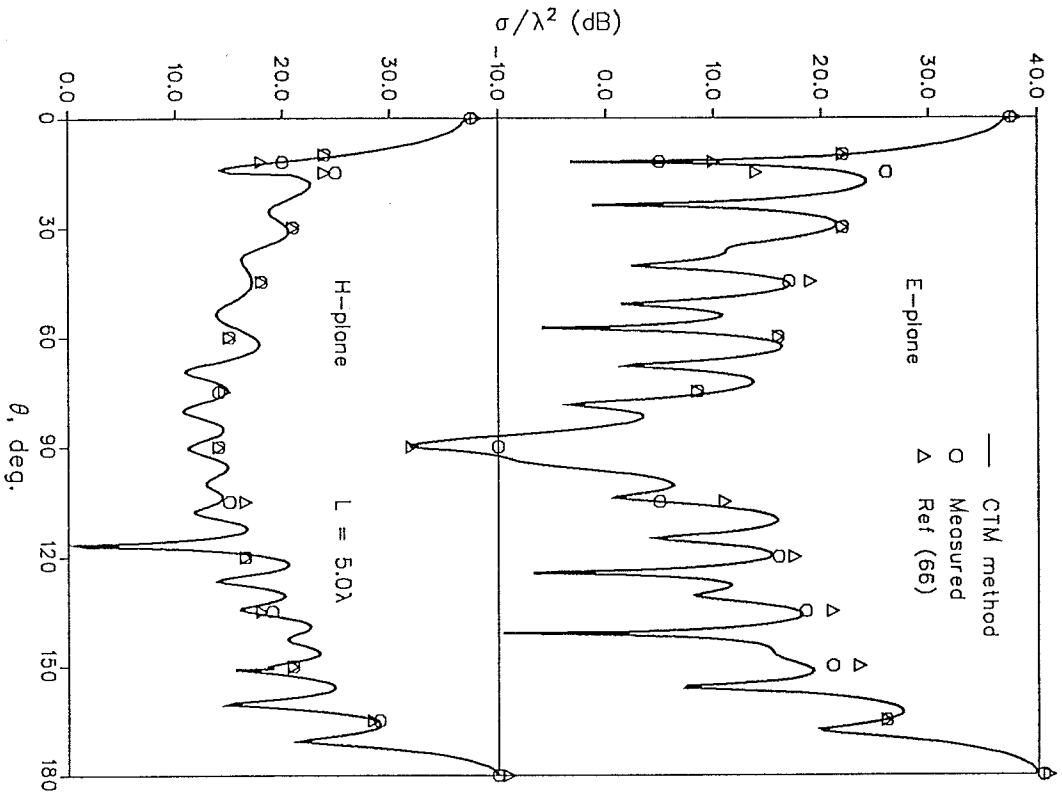


Fig. 2.4.c : Bistatic scattering patterns of a conducting cube, for a normal incident plane wave, same polarization as Fig. 2.4.a.

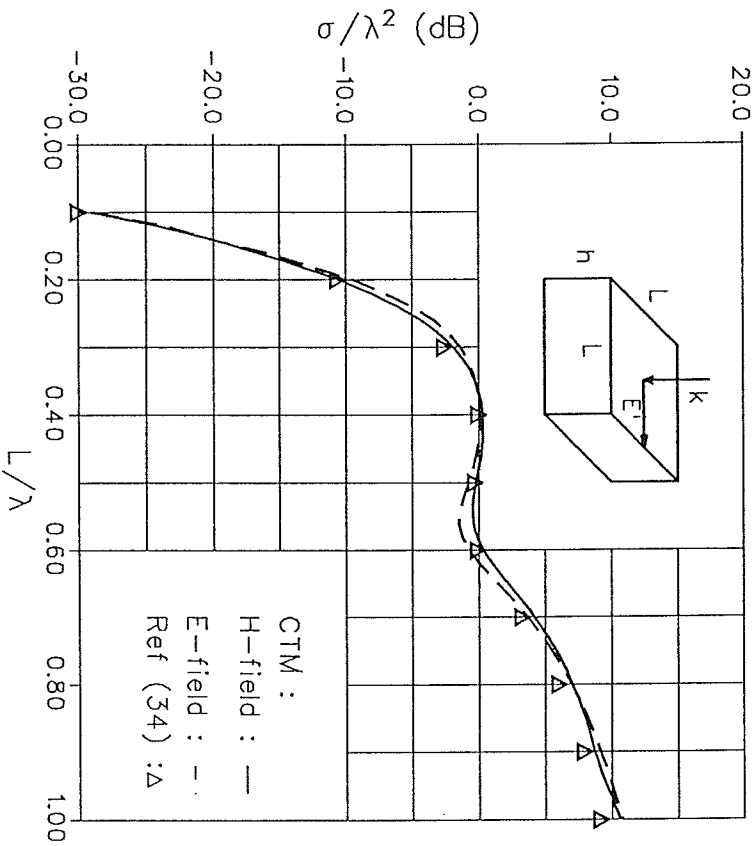


Fig. 2.6. : Back scattering cross-section of conducting rectangular box of $h=0.5\lambda$ for normal incidence.

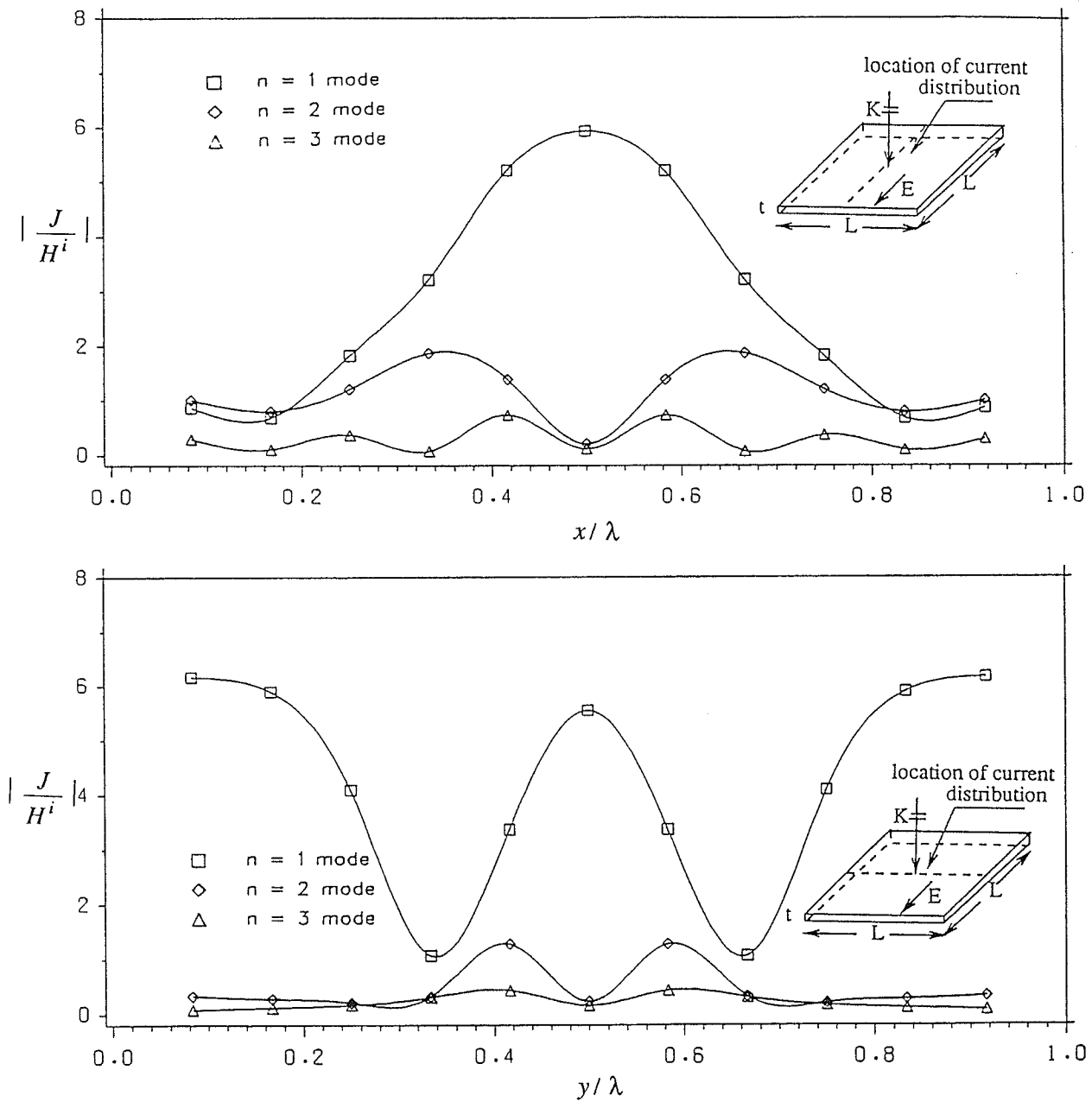


Fig. 2.5 : Auxiliary current distributions on the surface of conducting plate of $L = 1.0\lambda$ and thickness $t = 0.3017\lambda$, for a normal incident plane wave.

x -polarized case. For this case, the mode coupling was found to be strong and at least three modes, i.e. $n = 1, 2$ and 3 were necessary to generate a convergent result. However, the results using the first five modes, for $n = 1$ to 5 , were also obtained and shown in the figure, to indicate the solution convergence.

Fig. 2.8 illustrates the back scattering patterns of a thick rectangular plate of size $L \times 0.25L$, illuminated by a plane wave at broadside. Here, the transformation constants are $l = 0.1771517$, $\alpha = 27.9091847^\circ$, and 12 terms in (2.69) were selected. To represent the \hat{t} -current two expansion functions each modeled by six impulses were selected. Here, due to an extensive deformation of the cross-section from a circle, the mode coupling is more pronounced and up to five Fourier modes were required for the solution to converge. Also, as expected, from Figs 2.7 and 2.8, the polarization parallel to the length of the rectangle yields higher radar cross-sections than the one along its width.

As a final example, the back scattering patterns of a more general prism, i.e. a thick plate are presented in Fig. 2.9. The geometry under consideration is a conducting box with $2\lambda \times 1\lambda \times 1\lambda$ dimensions and illuminated by a normally incident plane wave at different sides. The patterns were obtained by selecting 14 linear functions along the \hat{t} -direction. From Fig. 2.9 one can observe that, as the size of the geometry increases, more standing wave patterns appear. Also, as the aspect ratio changes to 0.5 at least three modes, i.e. $n = 1, 2, 3$ are required for the solution to converge. Similarly, as the electrical size of the object increases two additional current modes were necessary to improve the accuracy.

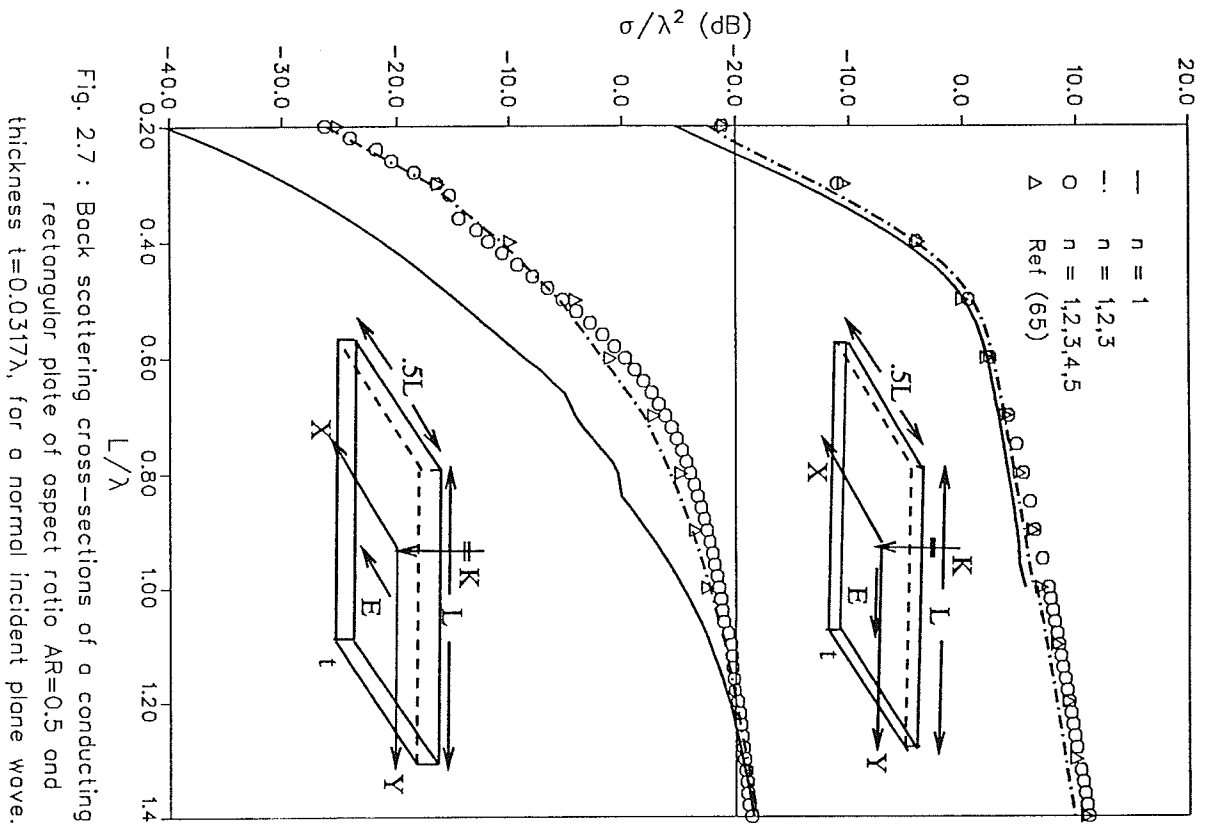


Fig. 2.7 : Back scattering cross-sections of a conducting rectangular plate of aspect ratio $AR=0.5$ and thickness $t=0.0317\lambda$, for a normal incident plane wave.

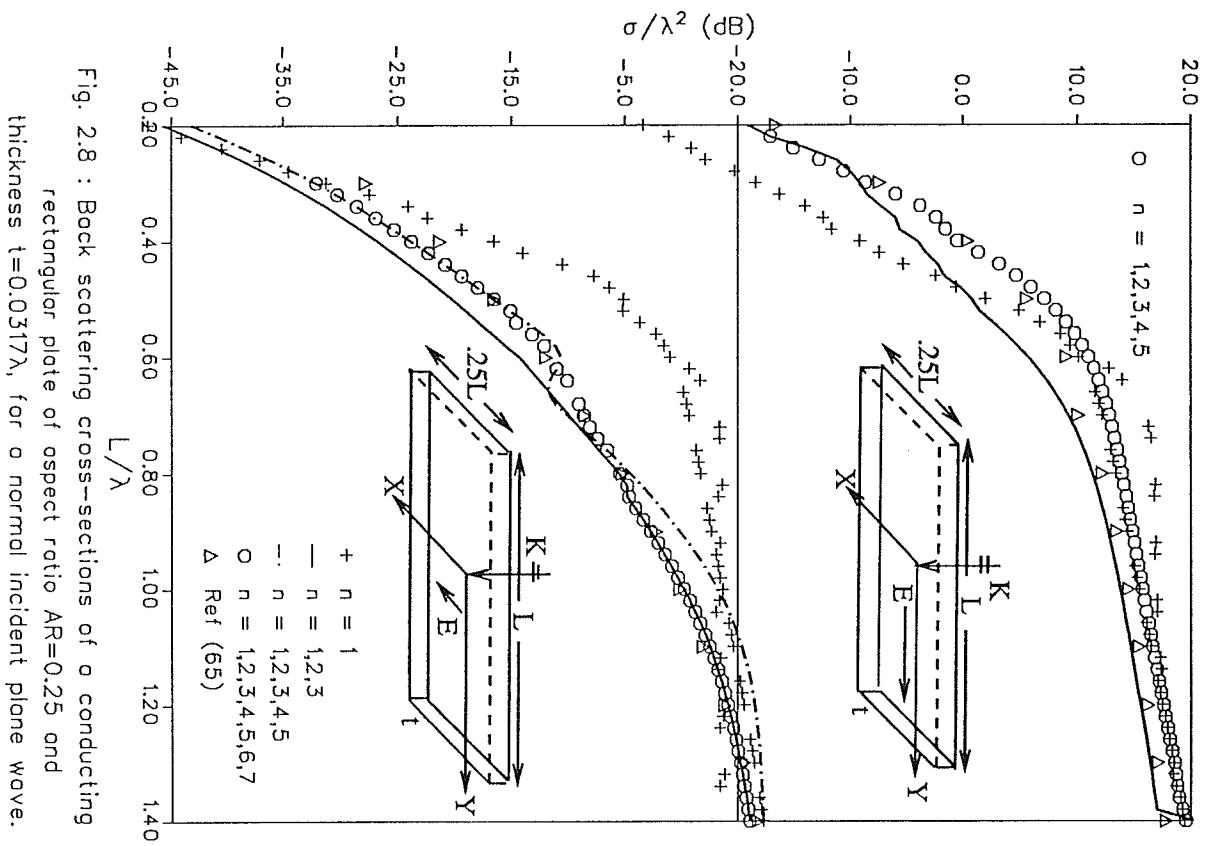


Fig. 2.8 : Back scattering cross-sections of a conducting rectangular plate of aspect ratio $AR=0.25$ and thickness $t=0.0317\lambda$, for a normal incident plane wave.

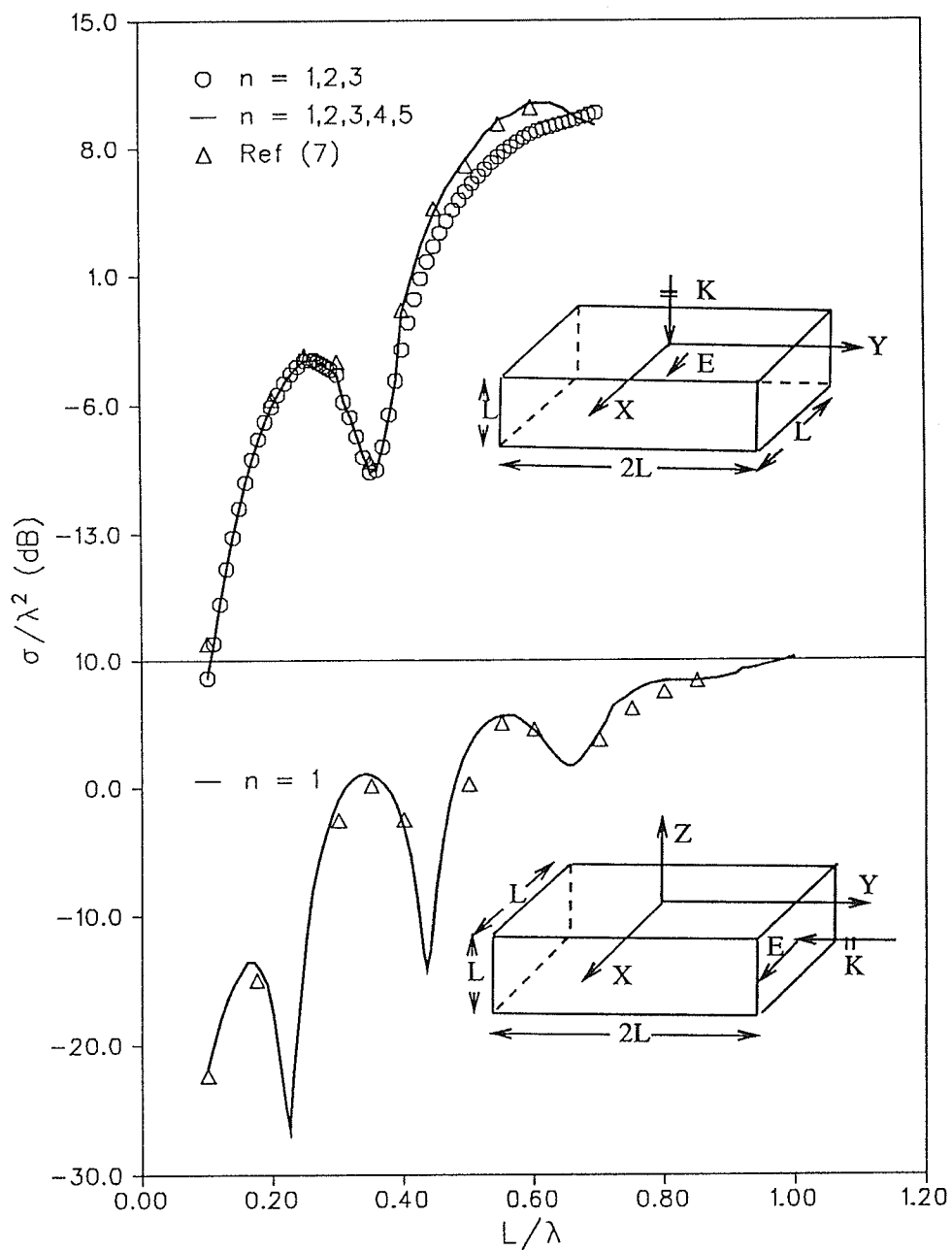


Fig. 2.9 : Back-scattering cross-sections of a conducting rectangular box of aspect ratio $AR = 0.5$ and height $h = 1. \lambda$, for a normal incident plane wave.

2.6.3. Effect of the incidence angle

Next, the solution of the integral operator was extended to arbitrary incident angles and its effect on the mode coupling was investigated. The degree of coupling and the effect of individual modes on the scattered field changes considerably, as the angle of incidence changes from the broadside direction to 90 degrees.

Figs. 2.10 illustrates the strength of the various modes and their effects on the scattered field of a square plate of size $L = 1.0 \lambda$ and thickness, $t = 0.1 \lambda$, illuminated by a plane wave of arbitrary incidence angle. As it was mentioned earlier, for the broadside incidence, the $n = 1$ mode has the highest contribution to the scattered field and higher order modes do not have significant contribution to the scattered field. However, as the angle of incidence changes from zero to 90 degrees the strength of the even modes increase and eventually the $n = 0$ mode becomes the dominant one. This trend can be observed from Figs 2.10.a to 2.10.b, where the contribution of the $n = 0, 2$ modes increases significantly, whereas the contribution of the odd modes to the scattered field decreases. The degree of contribution by even and the odd modes eventually reaches the same level. However, convergent solutions for highly oblique incidence of the plane wave, at angles between 60 and 90 degrees, are still obtainable by using the first five modes, Fig. 2.11.

2.7. Conclusions

The E- and H-field integral equations were used to develop a formulation for numerical solution of scattering by conducting objects of arbitrary cross-section. A moment method was then used to generate matrix equations for determining the surface currents. To develop these matrix equations a coordinate transformation was used. Initially, on the object's surface two orthogonal tangent vectors \hat{t} , \hat{s} were defined, where

t corresponded to its counter part for bodies of revolution. In the plane containing the \hat{s} vector the object's cross section was mapped conformally onto a circle to develop an analytic expression for the s vector. To apply the moment method triangular basis functions were selected along the \hat{t} vector and entire domain Fourier type basis functions were used in the cross-section. The resulting matrix equation was then a generalized form of that used for bodies of revolutions, in which current modes were coupled. The method was then applied to study the scattering by conducting plates and prisms.

It was found that for the cube sizes of less than 1λ , if illuminated by an axially incident wave, the mode coupling is not significant and selected basis set approaches the forms of the eigenfunctions of the operator. However, as the incident angle was changed from the normal to an arbitrary direction of incidence, the coupling was increased significantly and the solution required all current modes for a reasonable accuracy. The analysis was also extended to objects of rectangular cross-sections. It was found that the scattered field was quite sensitive to the number of the selected modes and usually 3 modes were required to provide convergent solutions for the aspect ratio of 0.5. Further deformation of the cross-section necessitated additional modes for the solution to converge, which in turns increased the size of the moment matrix. As a result the computer time increased rapidly. Thus the present method is most economical for bodies that are slightly non-cylindrical, such as objects with a square cross-section. The method extends the solution of bodies of revolution to arbitrary objects and provides a means for accurate computation of the scattering from arbitrary shape objects. It however requires a coordinate transformation.

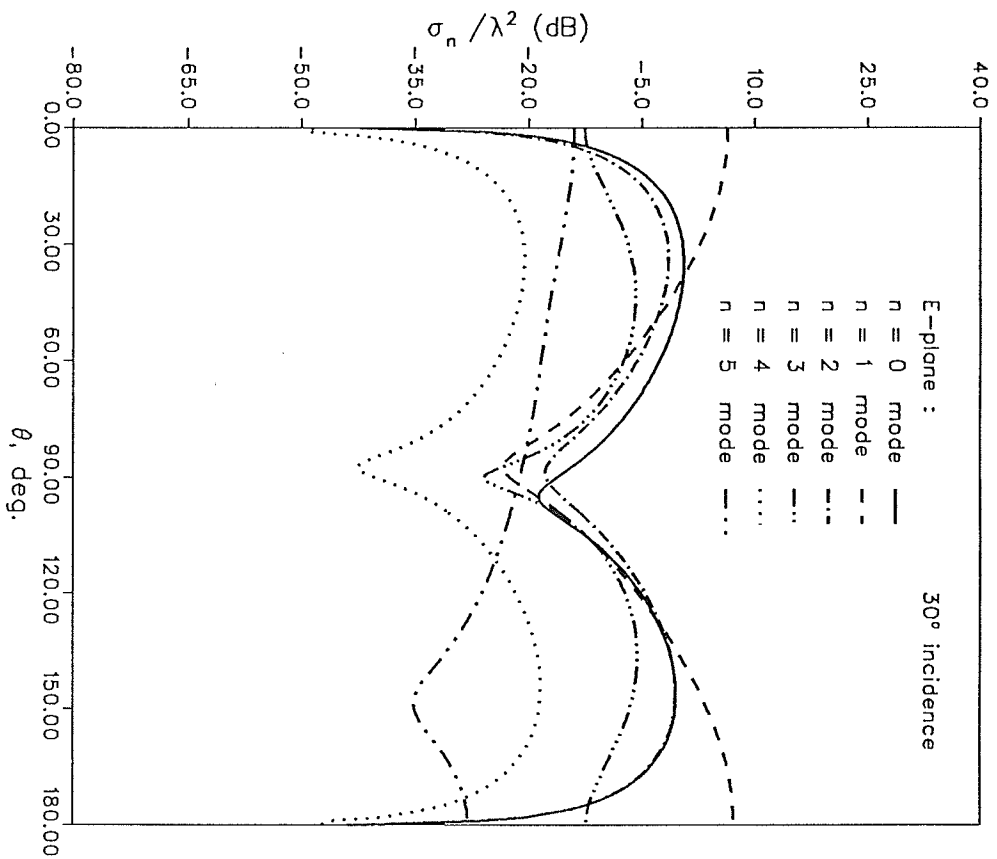
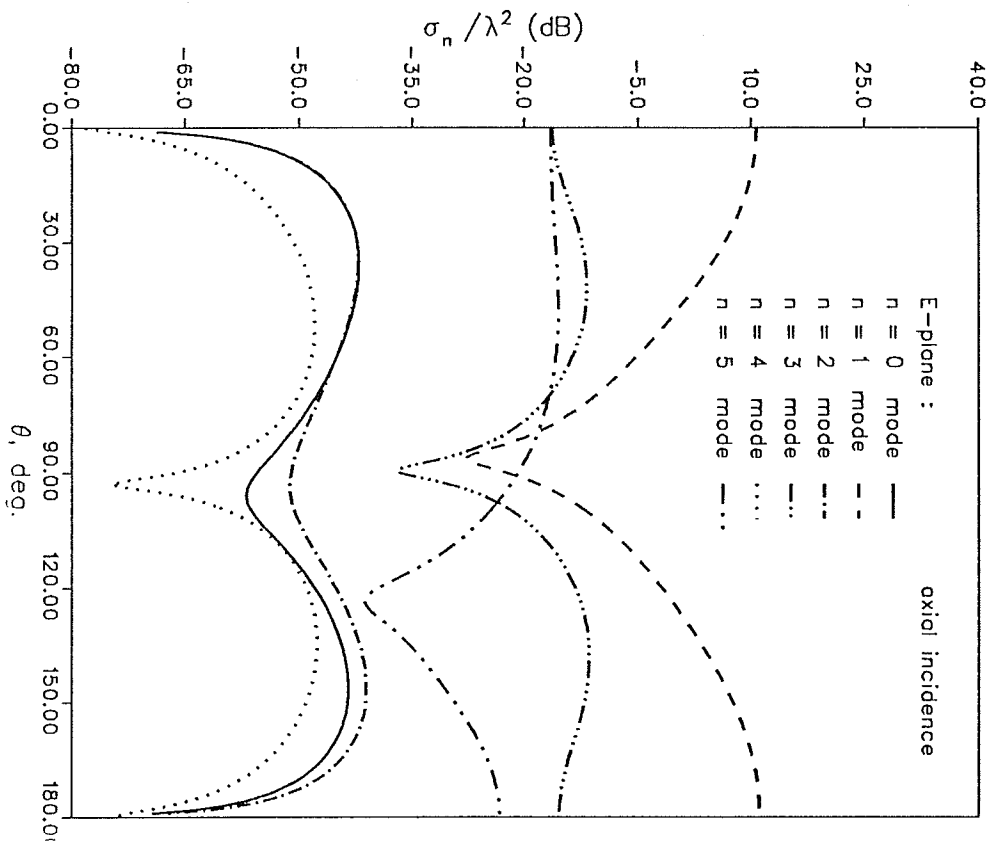


Fig. 2.10.a : Contribution of various modes to the bistatic scattering cross-section of a conducting square plate of side length $L = 1.0 \lambda$ and thickness $t = 0.1 \lambda$ for a plane wave incidence.

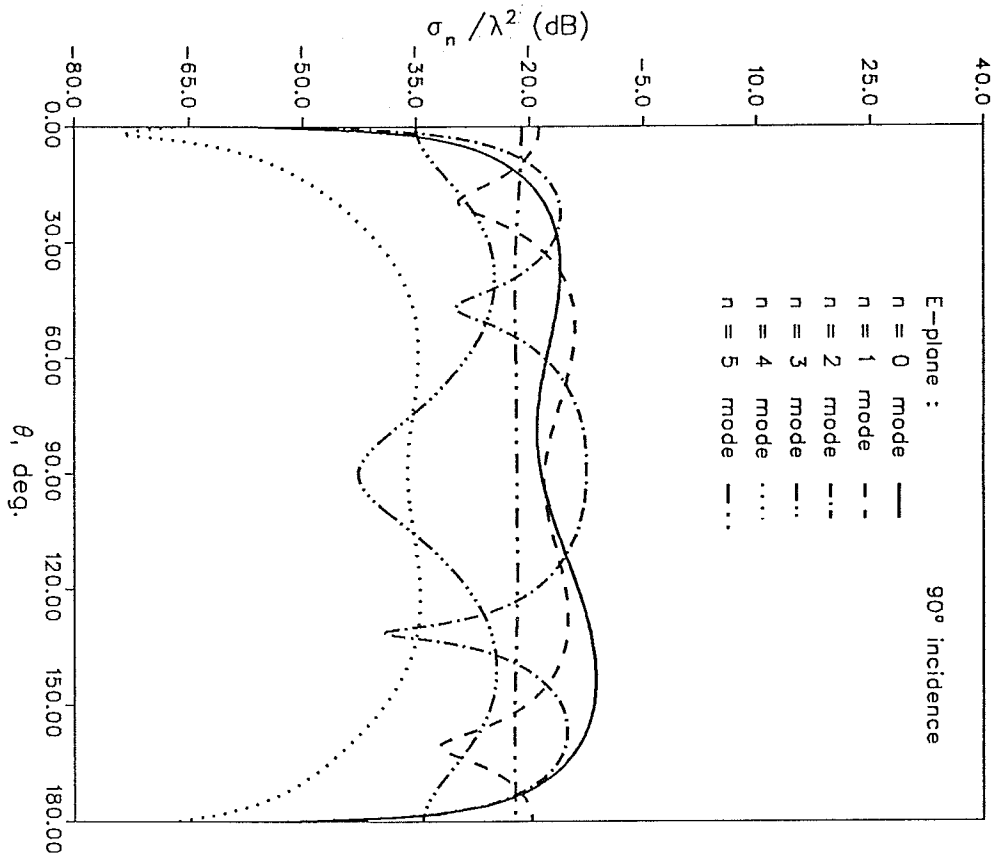
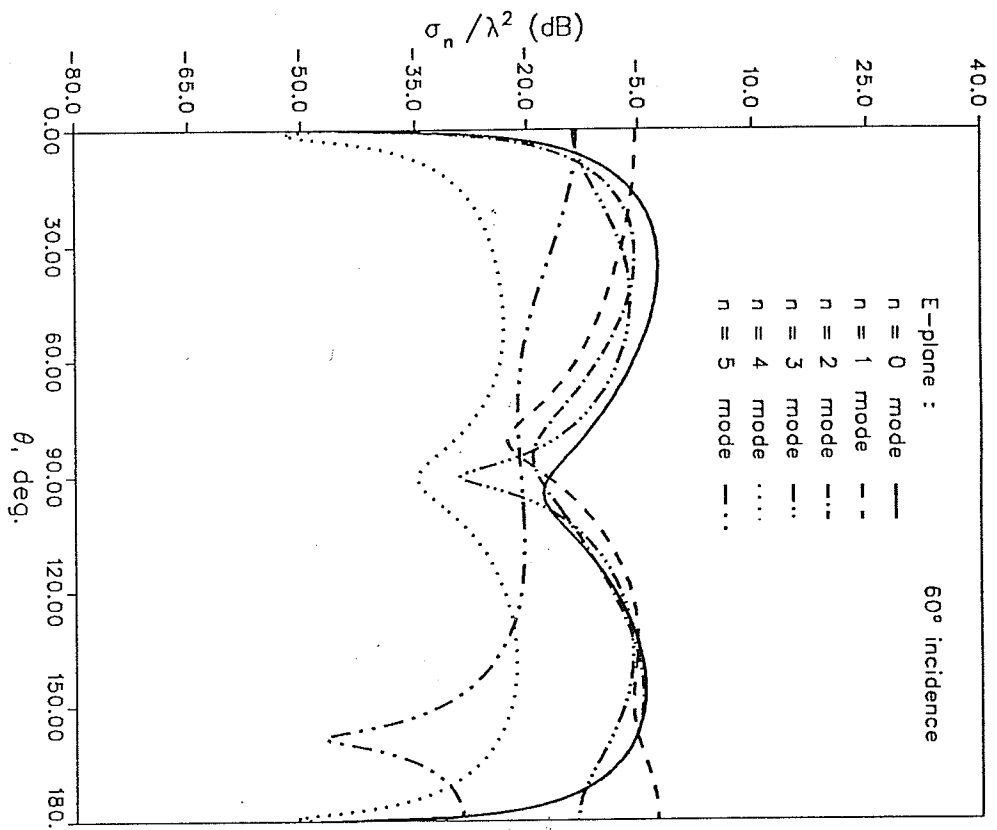


Fig. 2.10.b : Contribution of various modes to the bistatic scattering cross-section of a conducting square plate of side length $L = 1.0 \lambda$ and thickness $t = 0.1 \lambda$, for a plane wave incidence.

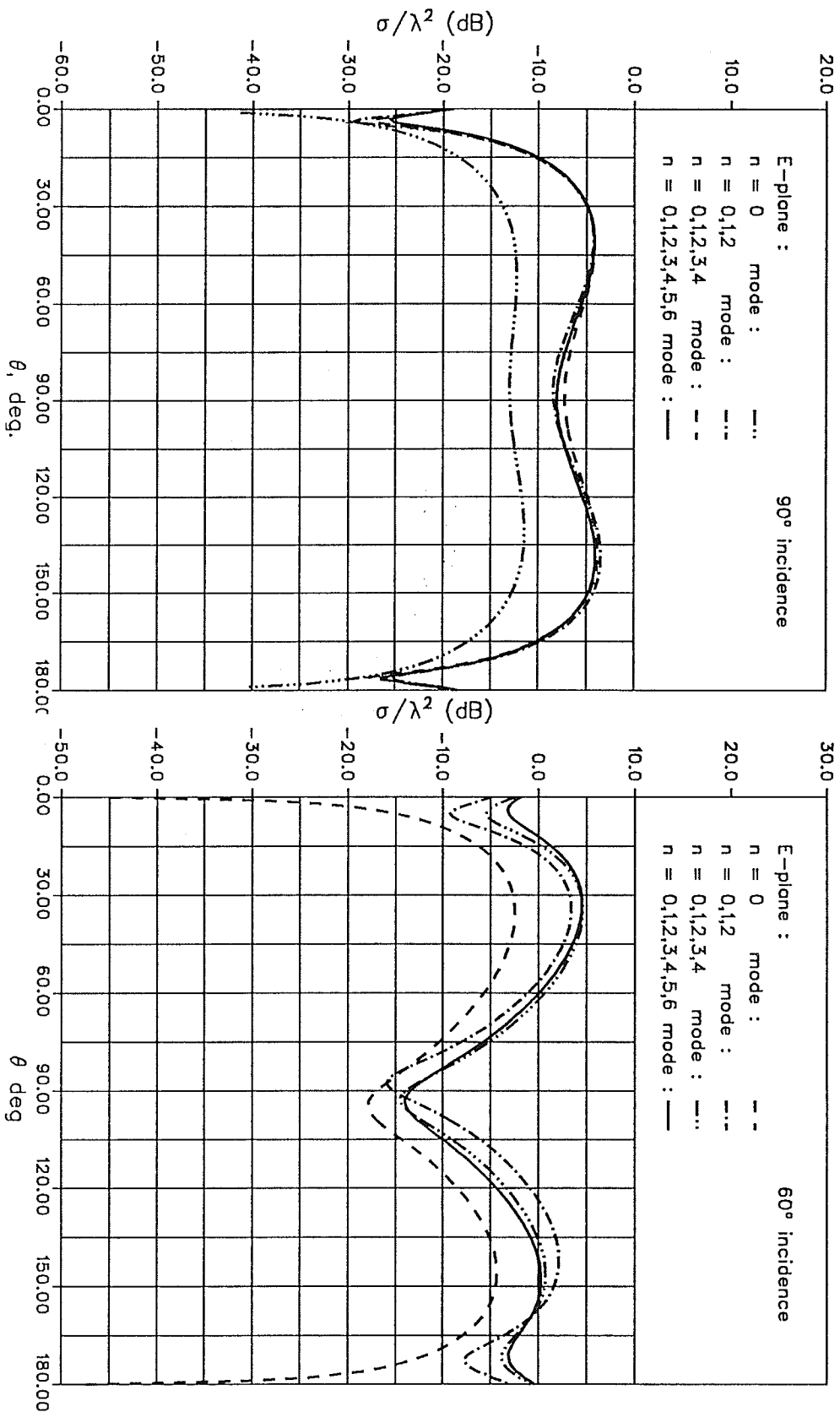


Fig. 2.11 : Bistatic scattering cross-section of a conducting square plate of side length $L = 1.0\lambda$ and thickness $t = 0.1\lambda$, for a oblique incident plane wave.

Chapter 3

Direct Method

3.1. Introduction

In the last chapter a numerical formulation was introduced to study the scattering from bodies of arbitrary cross-section. The purposed technique was based on a coordinate transformation from object's coordinates to new ones in order to utilize entire domain cylindrical modes. It was geometry dependent and as the cross-section of the object deviated from a cylinder by virtue of its aspect ratio, a larger number of modes were required for the solution to converge. Also the formulation required an analytical mapping function in order to relate the coordinates of the two spaces. The formulation presented in this chapter, does not require any coordinate transformation and therefore can be used for any objects of arbitrary shape. However, it usually needs more Fourier modes to converge. In this method the surface of the structure is geometrically represented by two orthogonal contours; generated respectively by intersection of the objects surface with the $x-z$ and $x-y$ planes. Similar to the conformal transformation method the hybrid basis functions are selected. However, the basis functions are expanded in the physical coordinate of the object, to represent the surface current.

Since the coordinate system is not separable for arbitrary objects, the selected basis functions are not the eigenfunctions of the integral operator, leading to the coupled current modes on the surface. Consequently, in using moment method to reduce integral equations to a matrix equation, the resulting matrix contains coefficients of all basis functions.

The general formulation of the E- and H-field integral equations are identical to the ones used in chapter two. Similar to the *CTM* technique, two orthogonal unit vectors \hat{t} , and \hat{s} are defined on the object's surface. The \hat{t} vector is defined along a contour that is the intersection of the $x-z$ plane with the surface of the object. The \hat{s} vector on the other hand, is along the corresponding contour in the $x-y$ plane, such that $\hat{n} = \hat{s} \times \hat{t}$, where \hat{n} is the unit normal of the surface. The surface integral equations are then reduced to a matrix equation by using the moment methods [7]. To accomplish this, sub-domain triangular basis functions are selected to represent the current dependence on the \hat{t} -vector and entire domain Fourier functions of the azimuthal angle ϕ are used to describe the \hat{s} -dependence of the surface current. However, as indicated above the latter functions are coupled on the objects surface and the resulting matrix equations include all current coefficients in a single equation.

Although, the formulation presented here is applicable to any arbitrary conducting object, solutions are provided only for simple geometries such as cubes and rectangular prisms in order to compare the present method with the *CTM* formulations. In the following sections the matrix formulation of each integral equation is presented.

3.2. Matrix formulation

For the sake of continuity, the notations are retained the same as those in chapter two. In order to obtain the moment matrix the total current can be decomposed on the object's surface as

$$\mathbf{J}(\mathbf{r}) = \hat{u}_t J^t(t, \phi) + \hat{u}_s J^s(t, \phi) \quad (3.1)$$

where, \hat{t} and \hat{s} define the proper orthogonal unit vectors on the object's surface as defined in (2.5) and (2.6). J^t and J^s denote their corresponding current components, expressed as

$$J^p = \sum_{n=-\infty}^{\infty} \sum_{j=1}^N a_{nj}^p J_{nj}^p \quad , \quad p = t \text{ or } s \quad (3.2)$$

The constants a_{nj}^p are current coefficients to be determined and J_{nj}^p are the basis functions defined by

$$\mathbf{J}_{nj}^p = \hat{u}_p f_j(t) e^{jn\phi} \quad (3.3)$$

The required weighting functions have the form of

$$\mathbf{W}_{mi}^p = \hat{u}_p f_i(t) e^{-jm\phi} \quad (3.4)$$

In equation (3.3), t represents the arc length along a selected generating curve of the structure, $f_i(t)$ is an overlapping triangle basis function defined in (2.31), n and m are the indices of the Fourier modes expanded along the circumference of the object, and ϕ is the azimuthal angle. A substitution of the current expansion (3.1) into the integral operators and after some manipulations, the general matrix equation takes the form

$$\sum_{n=-\infty}^{\infty} \sum_{j=1}^N (T_{mn}^{pq})_{ij} a_{nj}^p = E_{mi}^p \quad m = 0, \pm 1, \pm 2, \dots \quad (3.5)$$

where E_{mi}^p is the excitation vector, $(T_{mn}^{pq})_{ij}$ is either the impedance or admittance submatrices depending whether an electric or magnetic integral equation is used. The superscripts p and q denote either t or s which define four partitioned submatrices.

For the E-field operator, the following explicit expressions can be obtained for the elements of the partitioned sub-matrices $(Z_{mn}^{pq})_{ij}$

$$(Z_{mn}^{tt})_{ij} = j \sum_{p=1}^{2M} \sum_{q=1}^{2M} [T_p' T_q' (\sin \beta_i \sin \beta_j G_1 + \cos \beta_i \cos \beta_j G_2) - T_p' T_q' G_2] \quad (3.6.a)$$

$$(Z_{mn}^{st})_{ij} = \sum_{p=1}^{2M} \sum_{q=1}^{2M} [T_p' T_q' j (\sin \beta_j G_3) - \frac{m}{k \rho_{i'}} T_p' T_q' G_4] \quad (3.6.b)$$

$$(Z_{mn}^{ts})_{ij} = \sum_{p=1}^{2M} \sum_{q=1}^{2M} [T_p' T_q' j (-\sin \beta_i G_5) + \frac{n}{k \rho_{j'}} T_p' T_q' G_6] \quad (3.6.c)$$

$$(Z_{mn}^{ss})_{ij} = j \sum_{p=1}^{2M} \sum_{q=1}^{2M} [T_p' T_q' (G_7 - \frac{mn}{k^2 \rho_i \rho_{j'}} G_8)] \quad (3.6.d)$$

where

$$p' = p + 2M(i - 1) \quad , \quad q' = q + 2M(i - 1) \quad (3.7.a)$$

$$i' = p + M(i - 1) \quad , \quad j' = q + M(i - 1) \quad (3.7.b)$$

and, G's are the ϕ dependent line integrals defined as;

$$G_1 = \int_0^{2\pi} \int_0^{2\pi} F(\phi, \phi') \cos(\phi' - \phi) d\phi d\phi' \quad (3.8.a)$$

$$G_2 = \int_0^{2\pi} \int_0^{2\pi} F(\phi, \phi') d\phi d\phi' \quad (3.8.b)$$

$$G_3 = \int_0^{2\pi} \int_0^{2\pi} F(\phi, \phi') \sin(\phi' - \alpha) d\phi d\phi' \quad (3.8.c)$$

$$G_4 = \int_0^{2\pi} \int_0^{2\pi} \rho(\phi') G(r, r') L(\phi, \phi') e^{j(n\phi' - m\phi)} d\phi d\phi' \quad (3.8.d)$$

$$G_5 = \int_0^{2\pi} \int_0^{2\pi} F(\phi, \phi') \sin(\alpha' - \phi) d\phi d\phi' \quad (3.8.e)$$

$$G_6 = \int_0^{2\pi} \int_0^{2\pi} \rho(\phi) G(r, r') L'(\phi, \phi') e^{j(n\phi' - m\phi)} d\phi d\phi' \quad (3.8.f)$$

$$G_7 = \int_0^{2\pi} \int_0^{2\pi} F(\phi, \phi') \cos(\alpha' - \alpha) d\phi d\phi' \quad (3.8.g)$$

$$G_8 = \int_0^{2\pi} \int_0^{2\pi} G(r, r') L(\phi, \phi') L'(\phi, \phi') e^{j(n\phi' - m\phi)} d\phi d\phi' \quad (3.8.h)$$

with,

$$F(\phi, \phi') = \rho(\phi)\rho(\phi') G(r, r') e^{j(n\phi' - m\phi)} \quad (3.9)$$

$$L(\phi, \phi') = -\frac{1}{\rho} (\sin \phi \sin^2 \alpha + \cos \phi \cos^2 \alpha) \quad (3.10)$$

$$G(r, r') = \frac{e^{-jkR}}{kR} \quad (3.11)$$

and

$$R = |r - r'| = [(\rho - \rho')^2 + (z - z')^2 + 2\rho\rho'(1 - \cos(\phi - \phi'))]^{1/2} \quad (3.12)$$

Similarly, for the H-field integral equation the admittance matrix takes the form of

$$(Y_{mn}^{pq})_{ij} = \sum_{n=-\infty}^{\infty} \sum_{p=1}^{2M} T_{p+2M(i-2)} \sum_{q=1}^{2M} T_{q+2M(j-1)} (Y_{mn}^{pq})_{vv'} \quad (3.13.a)$$

$$\begin{aligned} v' &= p + M(i-1) \\ v &= q + M(j-1) \end{aligned} \quad (3.13.b)$$

where the elements of y_{mn}^{pq} are given as

$$(Y_{mn}^{uu})_{ij} = \frac{G_9}{k^2 \rho_i d_i} - \cos \beta_j (k \rho_j G_{10} + k \rho_i G_{11}) - k(z_j - z_i) \sin \beta_j G_{12} \quad (3.14.a)$$

$$(Y_{mn}^{st})_{ij} = k \rho_j \sin \beta_i \cos \beta_j G_{13} - k \rho_i \sin \beta_j \cos \beta_i G_{14} - k(z_j - z_i) \sin \beta_i \sin \beta_j G_{15} \quad (3.14.b)$$

$$(Y_{mn}^{ts})_{ij} = k(z_j - z_i) G_{16} \quad (3.14.c)$$

$$(y_{mn}^{ss})_{ij} = \frac{G_9}{k^2 \rho_i d_i} - \cos \beta_i (k \rho_j G_{11} - k \rho_i G_{17}) + k(z_j - z_i) \sin \beta_i G_{18} \quad (3.14.d)$$

Here, functions G 's are defined as,

$$G_9 = \frac{1}{2} \int_0^{2\pi} \rho(\phi) e^{j(n\phi - m\phi)} d\phi \quad (3.15.a)$$

$$G_{10} = \frac{1}{4\pi} \int_0^{2\pi} \int_0^{2\pi} p(\phi, \phi') \rho'(\phi') \cos(\phi' - \alpha) d\phi d\phi' \quad (3.15.b)$$

$$G_{11} = \frac{1}{4\pi} \int_0^{2\pi} \int_0^{2\pi} p(\phi, \phi') \rho(\phi) \cos(\phi - \alpha) d\phi d\phi' \quad (3.15.c)$$

$$G_{12} = \frac{1}{4\pi} \int_0^{2\pi} \int_0^{2\pi} p(\phi, \phi') \cos(\phi' - \alpha) d\phi d\phi' \quad (3.15.d)$$

$$G_{13} = \frac{1}{4\pi} \int_0^{2\pi} \int_0^{2\pi} p(\phi, \phi') \rho'(\phi') \sin(\phi' - \phi) d\phi d\phi' \quad (3.15.e)$$

$$G_{14} = \frac{1}{4\pi} \int_0^{2\pi} \int_0^{2\pi} p(\phi, \phi') \rho(\phi) \sin(\phi' - \phi) d\phi d\phi' \quad (3.15.f)$$

$$G_{15} = \frac{1}{4\pi} \int_0^{2\pi} \int_0^{2\pi} p(\phi, \phi') \sin(\phi' - \phi) d\phi d\phi' \quad (3.15.g)$$

$$G_{16} = \frac{1}{4\pi} \int_0^{2\pi} \int_0^{2\pi} p(\phi, \phi') \sin(\alpha' - \alpha) d\phi d\phi' \quad (3.15.h)$$

$$G_{17} = \frac{1}{4\pi} \int_0^{2\pi} \int_0^{2\pi} p(\phi, \phi') \rho(\phi) \cos(\alpha' - \phi) d\phi d\phi' \quad (3.15.i)$$

$$G_{18} = \frac{1}{4\pi} \int_0^{2\pi} \int_0^{2\pi} p(\phi, \phi') \cos(\alpha' - \phi) d\phi d\phi' \quad (3.15.j)$$

and,

$$p(\phi, \phi') = \rho(\phi)\rho(\phi')G(r, r') e^{j(n\phi' - m\phi)} \quad (3.16)$$

$$G(r, r') = \frac{1 + jkR}{k^3 R^3} e^{-jkR} \quad (3.17)$$

also, $R = |\mathbf{r} - \mathbf{r}'|$ as defined in equation (3.12).

3.3. Excitation matrix

For an arbitrary incident plane wave the i^{th} elements of the excitation vector are defined as

$$V_{mi}^{pq} = k \int_0^t \rho f_i(t) dt \int_0^{2\pi} (\hat{\mathbf{a}}_p \cdot \hat{\mathbf{a}}_q) e^{-j(\mathbf{k}_r \cdot \mathbf{r} + m\phi)} \rho d\phi \quad (3.18)$$

where p is either t or s , and q is the polarization of the incident wave. Using a $2M$ impulse approximation for the triangle functions $f_i(t)$, the elements of V_{mi}^{pq} for the x - and y -polarized incident wave can be defined as;

$$V_{mi}^{tx} = \sum_{p=1}^{2M} T_{p+2M(I-1)} \sin \beta_i G_{19} \quad (3.19.a)$$

$$V_{mi}^{sx} = \sum_{p=1}^{2M} T_{p+2M(I-1)} (-G_{22}) \quad (3.19.b)$$

$$V_{mi}^{ty} = \sum_{p=1}^{2M} T_{p+2M(I-1)} \sin \beta_i G_{20} \quad (3.19.c)$$

$$V_{mi}^{sy} = \sum_{p=1}^{2M} T_{p+2M(I-1)} G_{21} \quad (3.19.d)$$

where,

$$f(\rho, \phi) = \rho(\phi) e^{-jm\phi} e^{-jk_t \cdot r} \quad (3.20)$$

and the functions G 's are given by

$$G_{19} = \int_0^{2\pi} f(\rho, \phi) \cos \phi \, d\phi \quad (3.21.a)$$

$$G_{20} = \int_0^{2\pi} f(\rho, \phi) \sin \phi \, d\phi \quad (3.21.b)$$

$$G_{21} = \int_0^{2\pi} f(\rho, \phi) \cos \alpha \, d\phi \quad (3.21.c)$$

$$G_{22} = \int_0^{2\pi} f(\rho, \phi) \sin \alpha \, d\phi \quad (3.21.d)$$

The scattering matrix takes the same form as equation (3.18), in which k_r replaces k_t and the Fourier mode $-m$ replaces n . Once the current coefficients a_{ni}^p are found the scattering cross section can be obtained in term of the scattering matrices R_{ni}^{pq} as

$$\frac{\sigma^{pq}}{\lambda^2} = \frac{1}{16\pi^3} \left| \sum_{n=-\infty}^{\infty} R_{ni}^{pq} a_{ni}^p \right|^2 \quad (3.22)$$

3.4. Numerical results

Based on the above formulations a complete program is developed to compute the scattered field of conducting objects of arbitrary shape. To examine its validity and accuracy, it was first used to generate both bistatic and back scattering data for a conducting sphere. The results were compared with the analytic data and satisfactory agreement were obtained. Representative results for a few selected objects are provided

below.

3.4.1. cube

For conducting cubes in the resonance region, scattering data is available in literature that are obtained both experimentally and numerically. Since, it has sharp corners it makes the surface currents singular, affecting the solution accuracy. It is therefore used as the first example to evaluate the proposed method. The evaluation of the ϕ -dependent integrals is carried out by a sixty point Gauss-quadrature and selecting four impulses for triangular basis functions.

Figs. 3.1 illustrate the bistatic scattering patterns of a conducting cube of 0.75λ in size, illuminated by an axially incident plane wave. Also shown for comparison are the results of the conformal transformation method (CTM), and the experimental results of McGahan extracted from [66]. The incident field is an x -polarized plane wave and 9 triangular functions are used along the t -vector. For the s -dependence three Fourier modes, i.e. $n = 1, 2, 3$ are required for the solution to converge. The first mode was however adequate to generate the back and forward scattering data accurately. But, the bistatic patterns required two additional Fourier modes to converge. In addition, the pattern in the 45° plane required at least five Fourier modes, in order to converge. For the principle plane patterns the CTM technique required only the $n = 1$ mode. This means that at least two additional modes are required by the present method to yield accurate data, which result in larger matrix sizes and subsequently, more computer time.

Fig. 3.2 shows the radar cross section of a conducting cube, having a side length of 1.0λ , for a normal incident plane wave. Here, again nine triangular functions in the t -direction were selected. The computed results are compared with those of Tsai, obtained using a surface patch modeling and measured values of Ryan [65]. Three

Fourier modes, i.e. $n = 1,2,3$ were selected which resulted in a 54×54 matrix size.

3.4.2. plate

Fig. 3.3 depicts the back scattering cross-section of a square plate of thickness 0.0317λ and a side length of 1.0λ , illuminated by a normally incident plane wave from the broadside direction. The t -dependence is represented by five triangular functions. In the s -direction up to three Fourier terms in the variable ϕ were needed for the solution to converge. The computed results are compared with the sinusoidal reaction formulation of Wang [64].

Fig. 3.4 shows the back scattering patterns of a rectangular plate of the same thickness as the square plate, but having an aspect ratio of 0.5, illuminated from the broadside direction. Only three triangular basis functions were sufficient to represent the t -current and six impulses were selected to model each triangle. Here, the computed results of the first $n = 1$ mode, and $n = 1,2,3$ modes are presented. Surprisingly, the $n = 1$ mode replicates the results quite accurately for the frequency range higher than $\frac{L}{\lambda} = 0.5$. For comparison the numerical results of Tsai [65], obtained using the surface patch technique, is also included.

In contrast to the coordinate transformation method (*CTM*), the selected Fourier modes here, are not periodic on each surface and do not incorporate the singularity of the edge current. Consequently, for the selected geometries more Fourier modes are needed for the solution to converge. For instance, to obtain the bistatic patterns of geometries such as cubes of size less than 1.0λ , at least three modes, i.e., $n = 1,2,3$ are required to obtain a reasonable accuracy. For the back scattering cases, usually one mode is sufficient, for the selected objects. As the size of the scatterer increases, more Fourier modes become necessary to incorporate the effect of the edge currents. In this respect, the two techniques are different, since the coordinate transformation method

requires additional Fourier type modes when the objects cross-section deviates from a circle.

In order to show the mode coupling and their physical effect on the scattered field, individual current modes are plotted on the object's surface. Fig. 3.5 shows the current distributions on a square plate of size $L = 0.6\lambda$ and thickness $t = 0.0317\lambda$. Three Fourier modes are plotted to show, in turn, the coupling and also the convergence of the solution. Each current mode is scaled by the proper length of the contour t and a cubic spline method with continuous second derivatives is used to interpolate between the sample points. The dominant mode is the $n = 1$ mode, which has the largest contribution to the scattered field. The $n = 2$ mode does not contribute to the computation of the scattered field, since the source of excitation is symmetric on the plate's surface. The third mode, i.e., $n = 3$ mode is present, but it is not as dominant. However, it describes the behavior of the edge current. Also presented, is the total current on the plate. From Fig. 3.5, one can observe that the edge behavior of the surface current has appeared by including the additional modes, which is confined to the area near the edge. Also, the J' component of the surface current exhibits the standing wave pattern which is the behavior of the current for the applied field.

The contribution of the individual modes and their effect to the scattered field are investigated for different angles of incident, i.e., $0^\circ, 30^\circ, 60^\circ, 90^\circ$, and selected results for two incident angles are presented in Figs. 3.6 and 3.7. The geometry under consideration is a thick plate of a base area $A = 1.0\lambda^2$ and the thickness of $t = 0.1\lambda$. Again, 7 linear expansion functions in the t -direction are selected and a sixty point Gauss quadrature is used. These computations illustrate the existence of the coupling among the odd modes for the axially incident wave. The dominant mode is the $n = 1$ mode and the contribution of the even modes to the scattered field is practically nonexistent. The generated moment matrix is diagonally dominant, and the interaction among the off diagonal elements is weak.

The order of the coupling and contribution of each mode, change drastically as the incident angle deviates from the broadside to the edge on incidence. The amplitudes of the even modes increase and eventually the dominant mode becomes the zero order mode ($n = 0$). Also, the mode convergence is slower, and for the selected geometry up to six modes are required to yield satisfactory results, for an end fire incidence. In this case, selection of six modes results in a 84×84 moment matrix.

3.5. Conclusions

A method was presented to study the electromagnetic scattering from conducting bodies of arbitrary shape using both Electric and Magnetic field surface integral equations. It was an extension of the method used for bodies of revolution to geometries of arbitrary shape. In this method the physical structure of the objects were geometrically represented by two contours; one along the $x-z$ plane and the other along the $x-y$ plane. Hybrid basis functions was selected to model the surface currents by virtue of the current decomposition on the surface. Subsectional basis functions were selected to model the current in the $x-z$ plane, and Fourier basis functions were selected to model the current in the plane normal to $x-z$ plane. A moment method was then used to generate matrix equations for determining the surface currents. The method was then applied to study the scattering from various conducting objects such as plates and prisms. The convergence and accuracy of the formulations were compared with the coordinate transformation method. It was found that for the selected basis functions the mode coupling was present and was related to the size of the scatterer, and also to the angle of incidence. However, the coupling was found to be independent of the geometry's aspect ratio. For the broadside illumination of the selected configurations normally three coupled modes were adequate to provide an acceptable results in agree-

ment with the *CTM* method. However additional modes, i.e., 4 and 5, were needed to obtain the convergence of the solutions for the edge on incidence. Consequently, the size of the moment matrix increased which resulted in a drastic rise in the computer time. Thus, at the present time, the formulation is useful mostly for geometries, whose physical size is of the order of a wavelength.

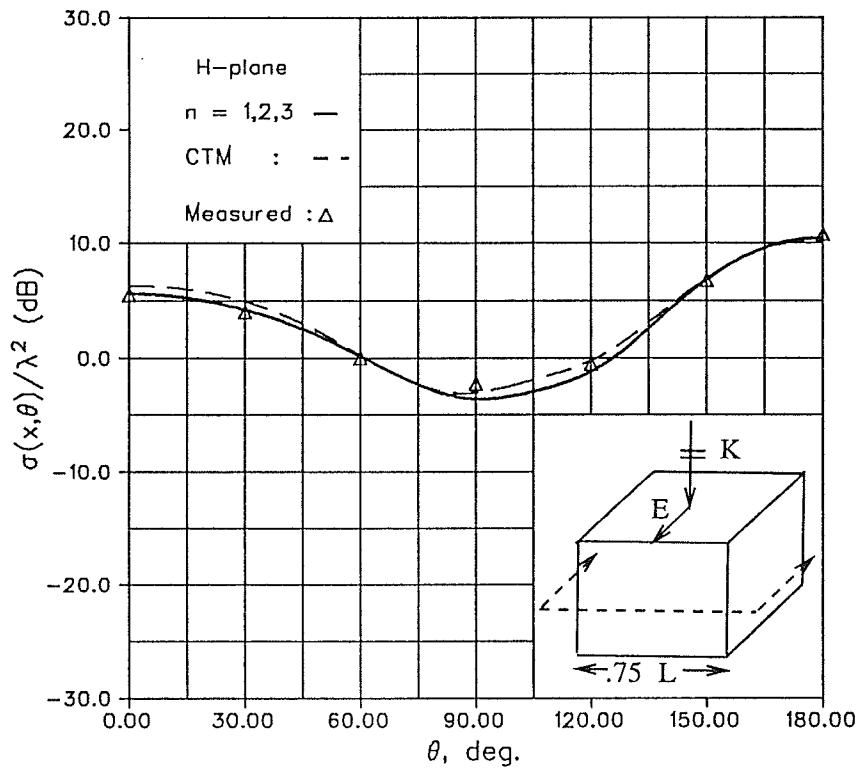
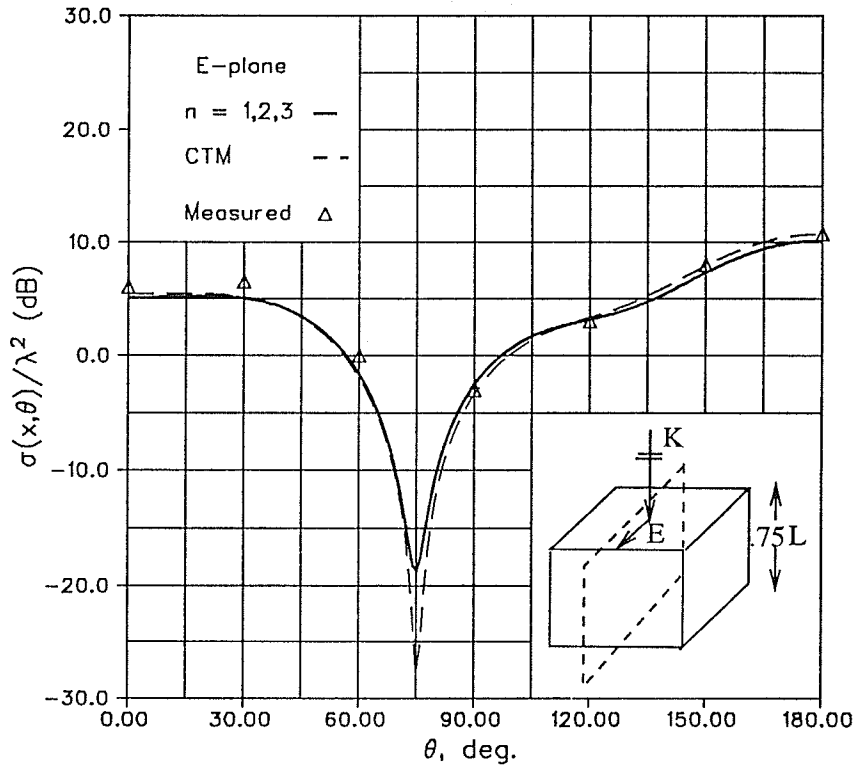


Fig. 3.1.a : Bistatic scattering patterns of a conducting cube of $L/\lambda = 0.75$ for a normal incident plane wave.

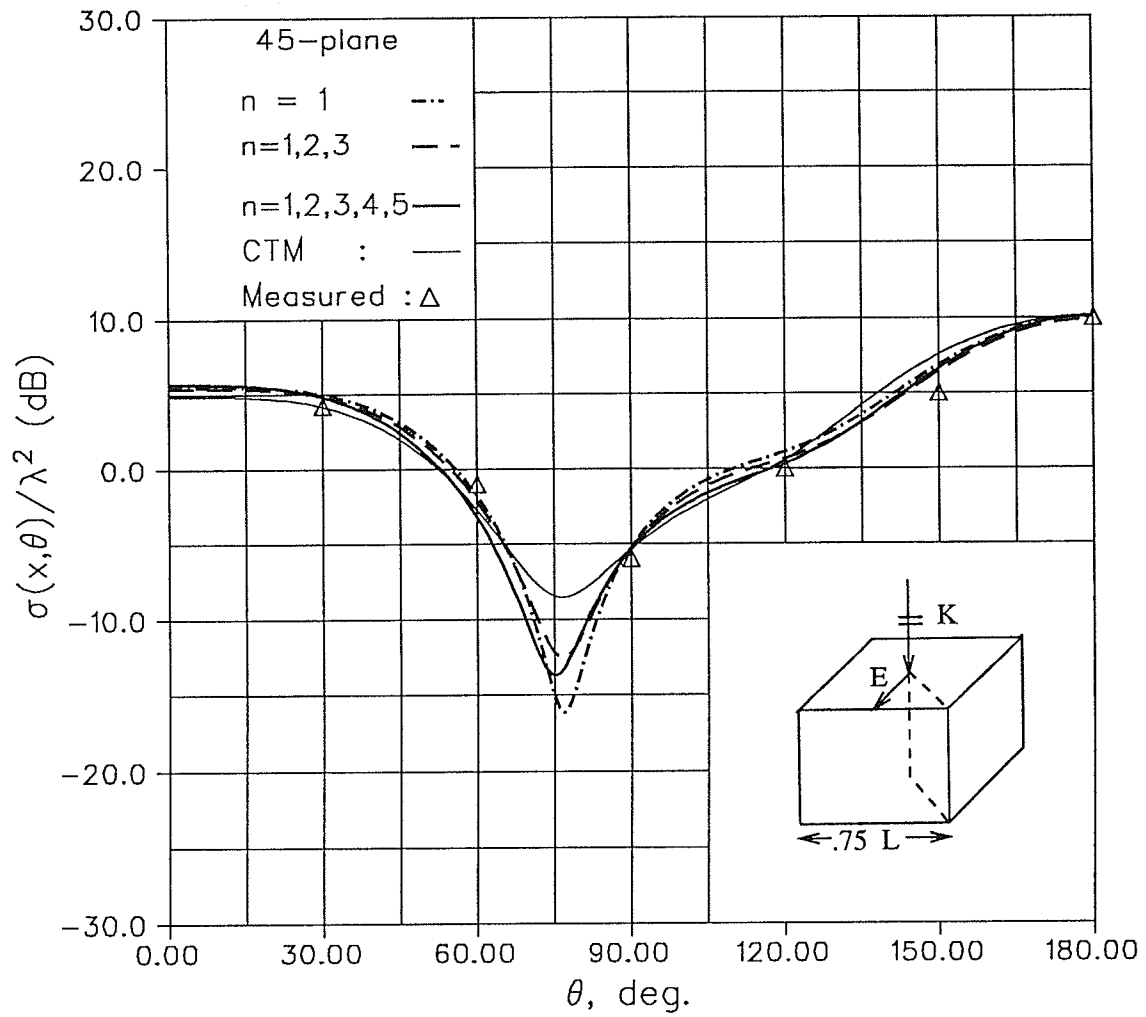


Fig. 3.1.b : Bistatic scattering pattern of a conducting cube of $L/\lambda = .75$ for a normal incident plane wave.

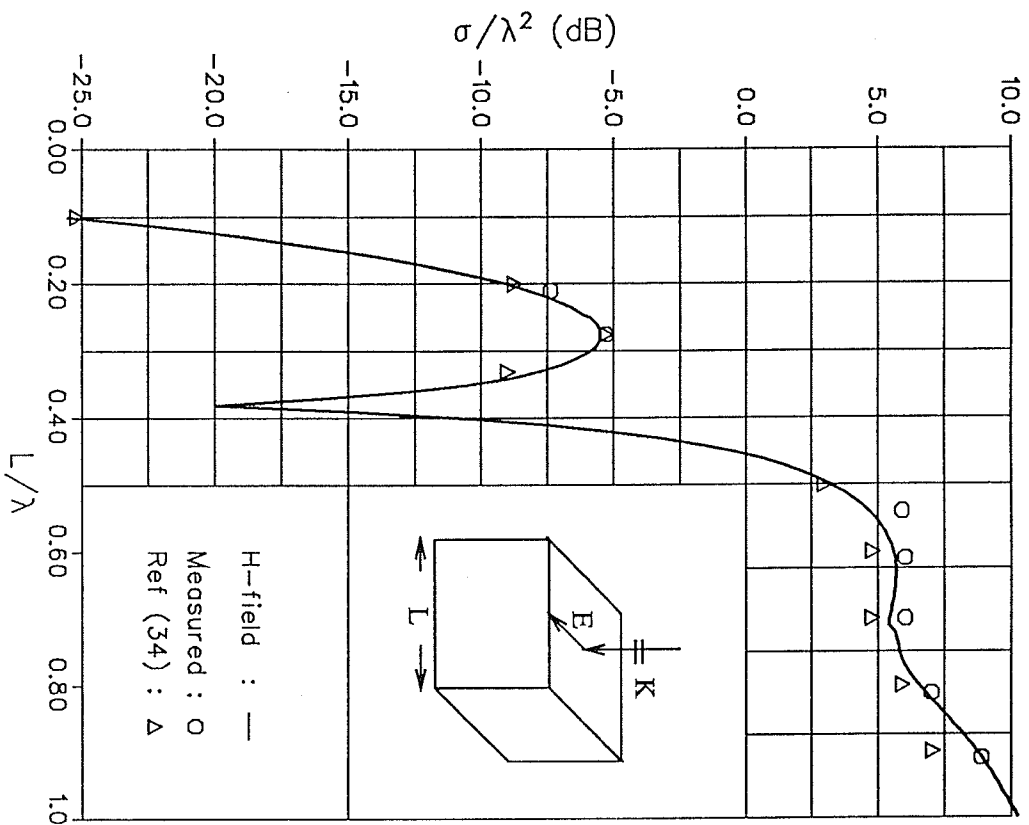


Fig. 3.2 : Back scattering cross-section of a conducting cube of sidelength L , for a normal incident plane wave.

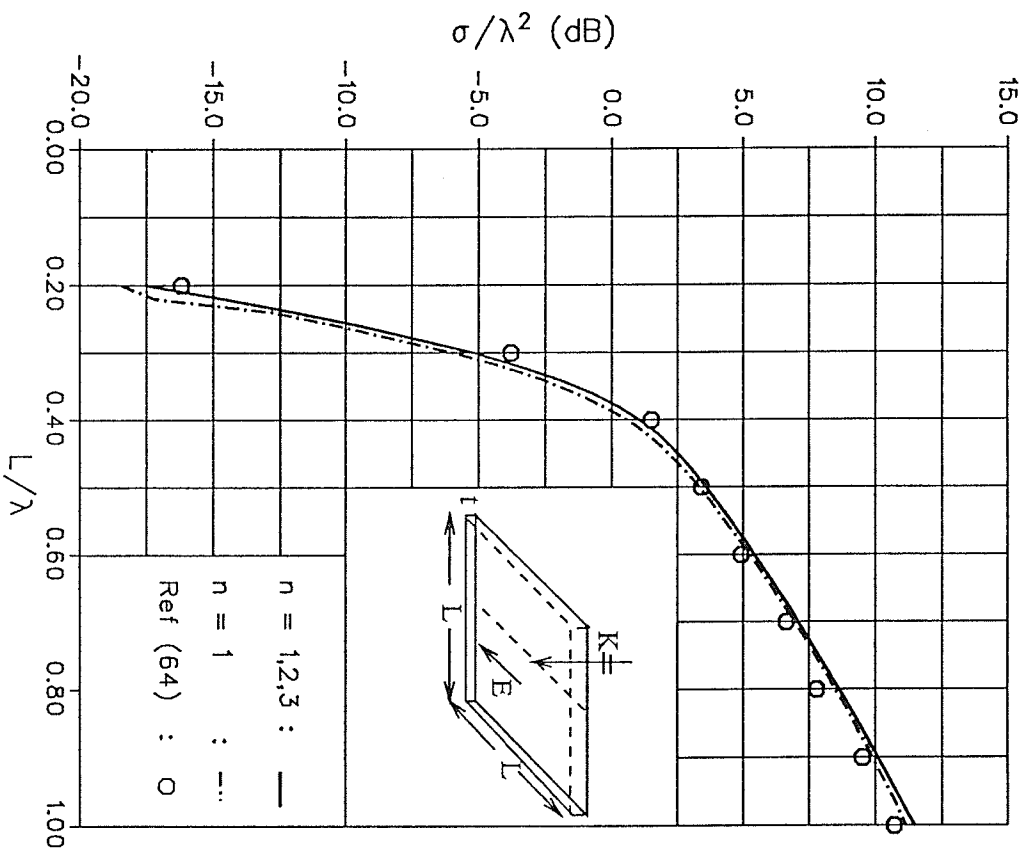


Fig. 3.3 : Back scattering cross-section of a conducting square plate of thickness $t=0.0317\lambda$, for a normal incident plane wave.

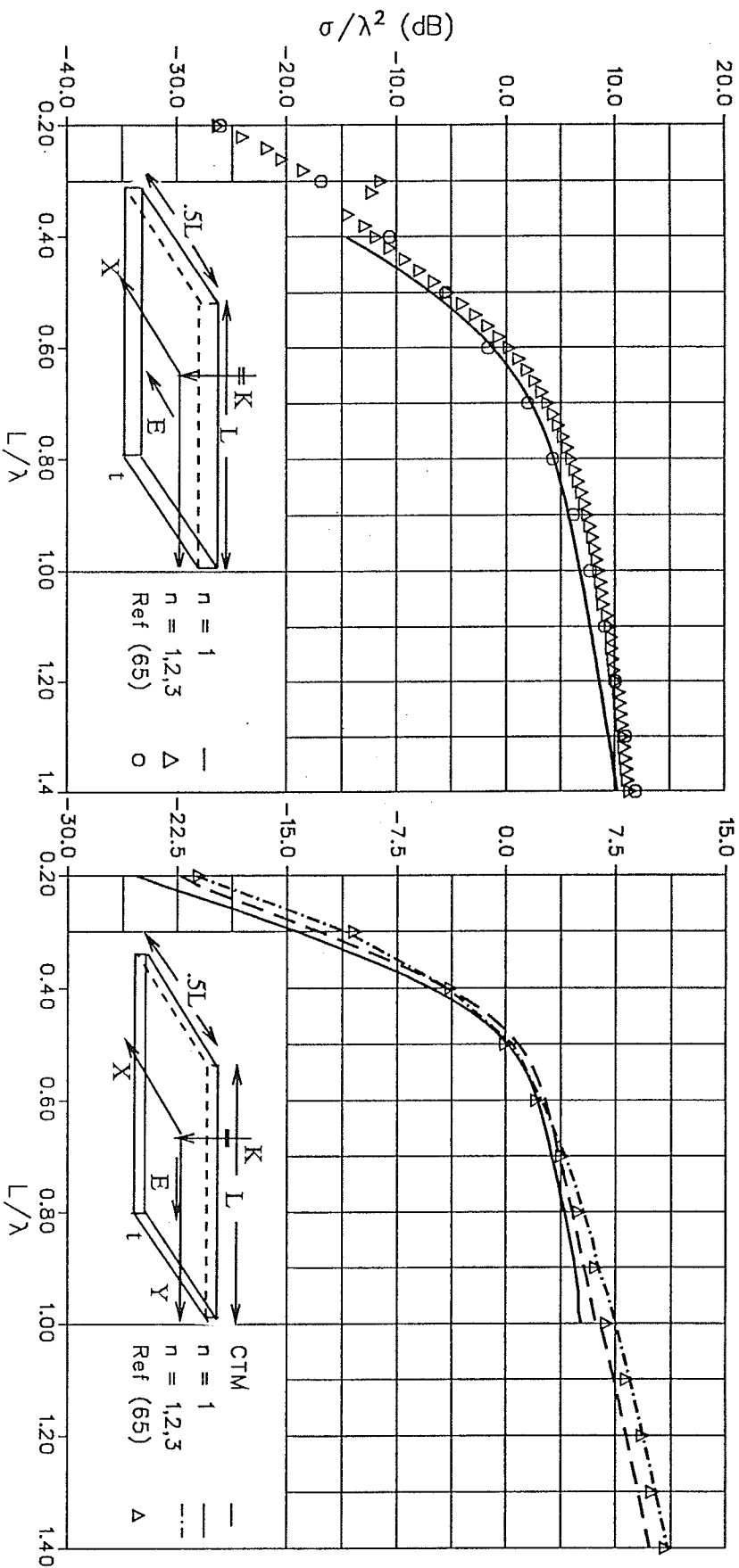


Fig. 3.4 : Back scattering cross-sections of a conducting rectangular plate of aspect ratio $AR = 0.5$ and thickness $t = 0.0317\lambda$, for a normal incident plane wave

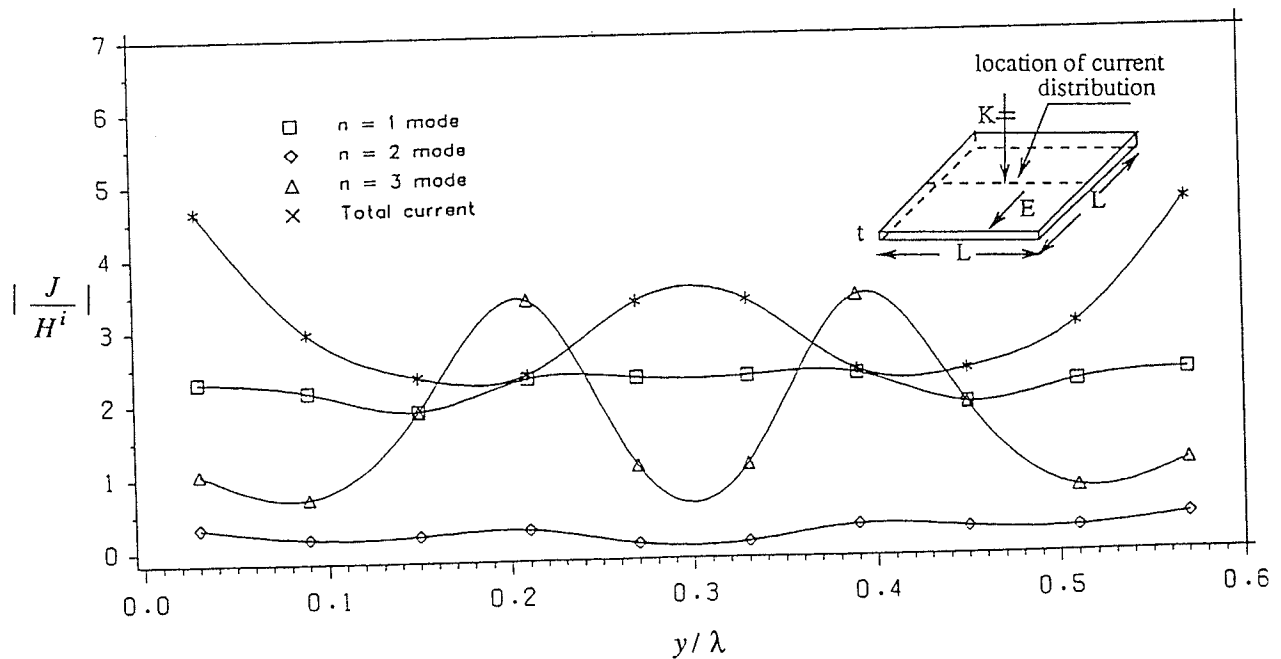
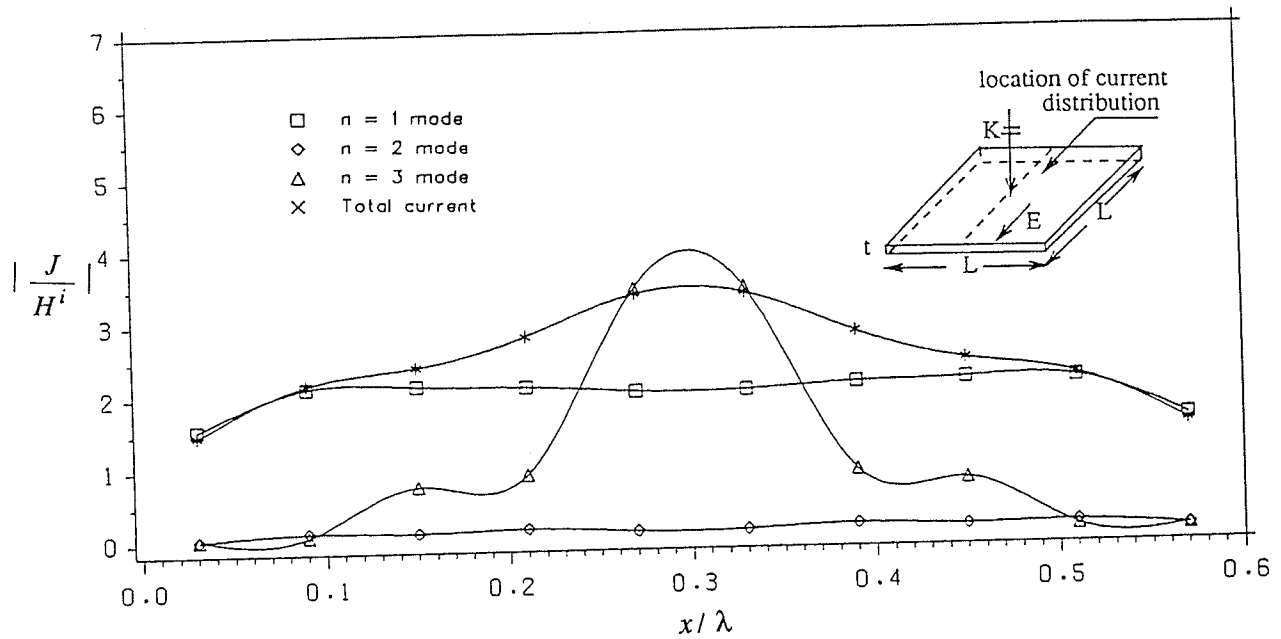


Fig. 3.5 : Current distributions on the surface of conducting plate of $L = 0.6\lambda$ and thickness $t = 0.0317\lambda$, for a normal incident plane wave.

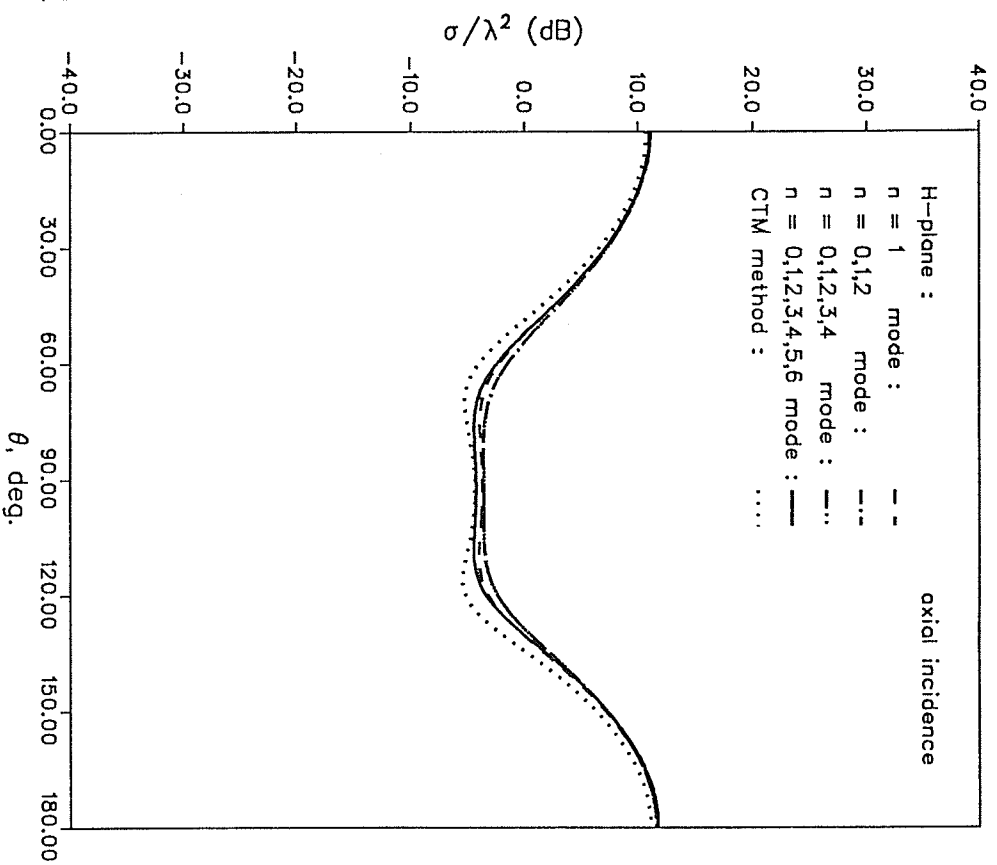
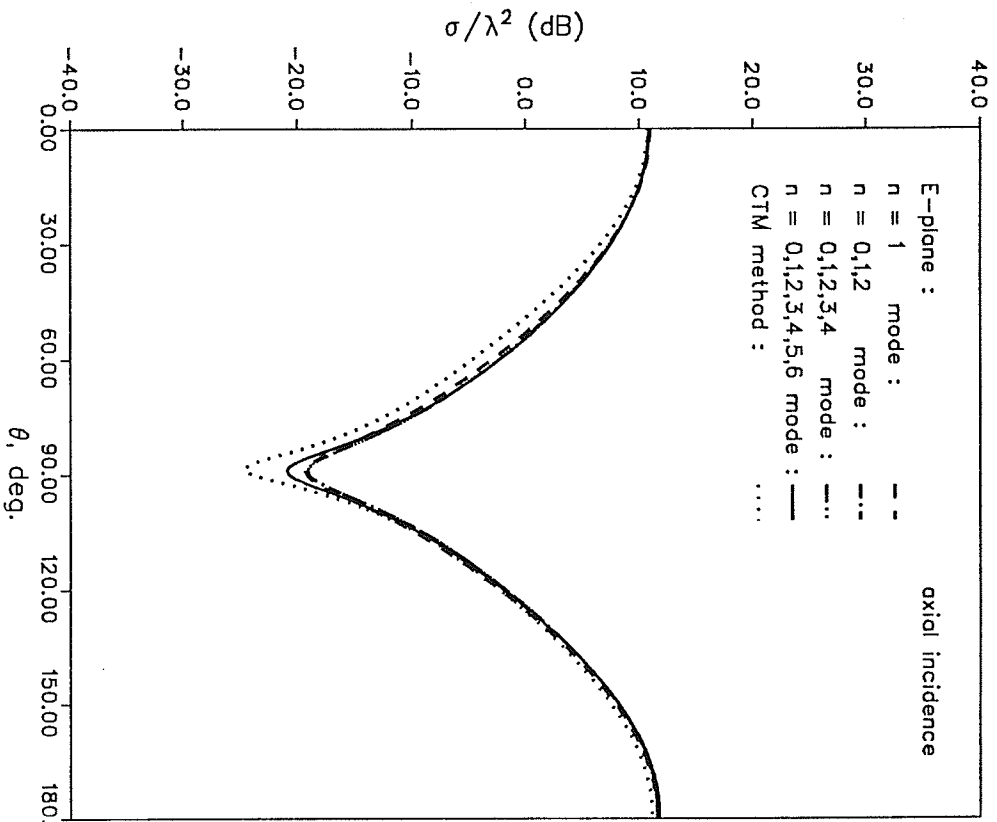


Fig. 3.6.a : Bistatic scattering cross-sections of a conducting square plate of side length $L = 1.0 \lambda$ and thickness $t = 0.1 \lambda$, for a normal incident plane wave.

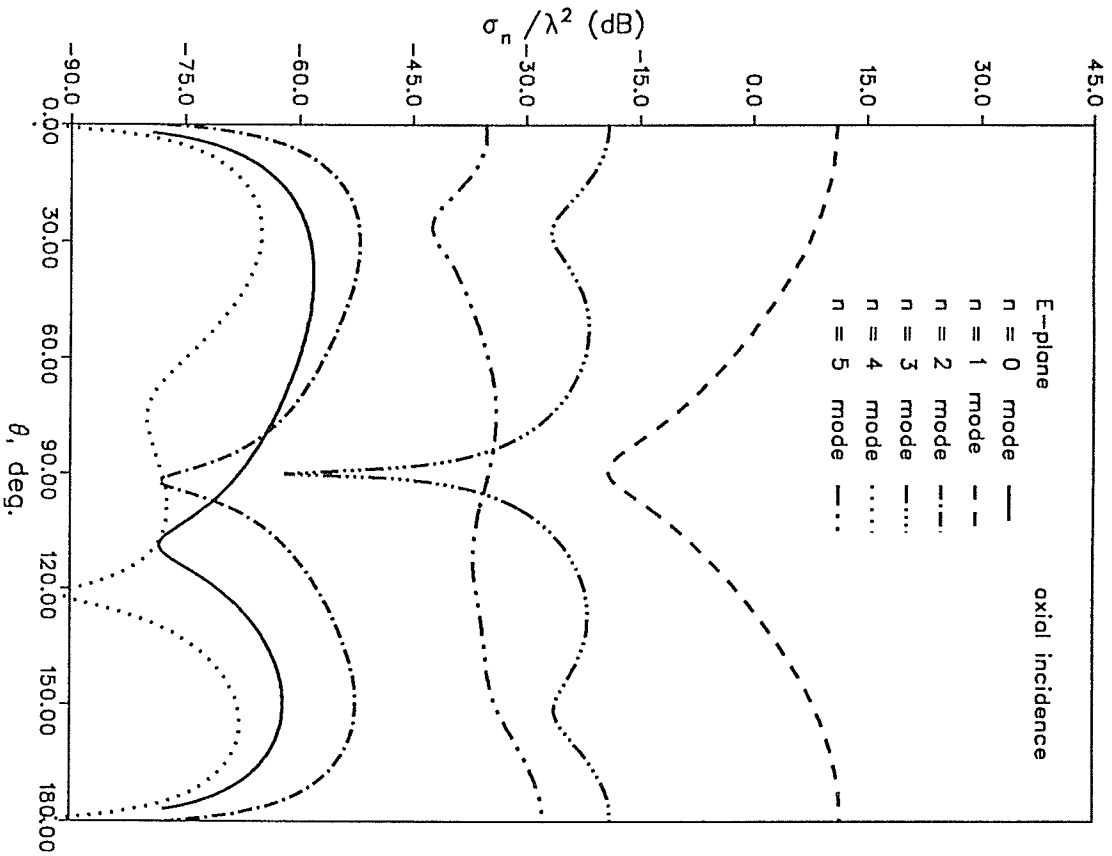
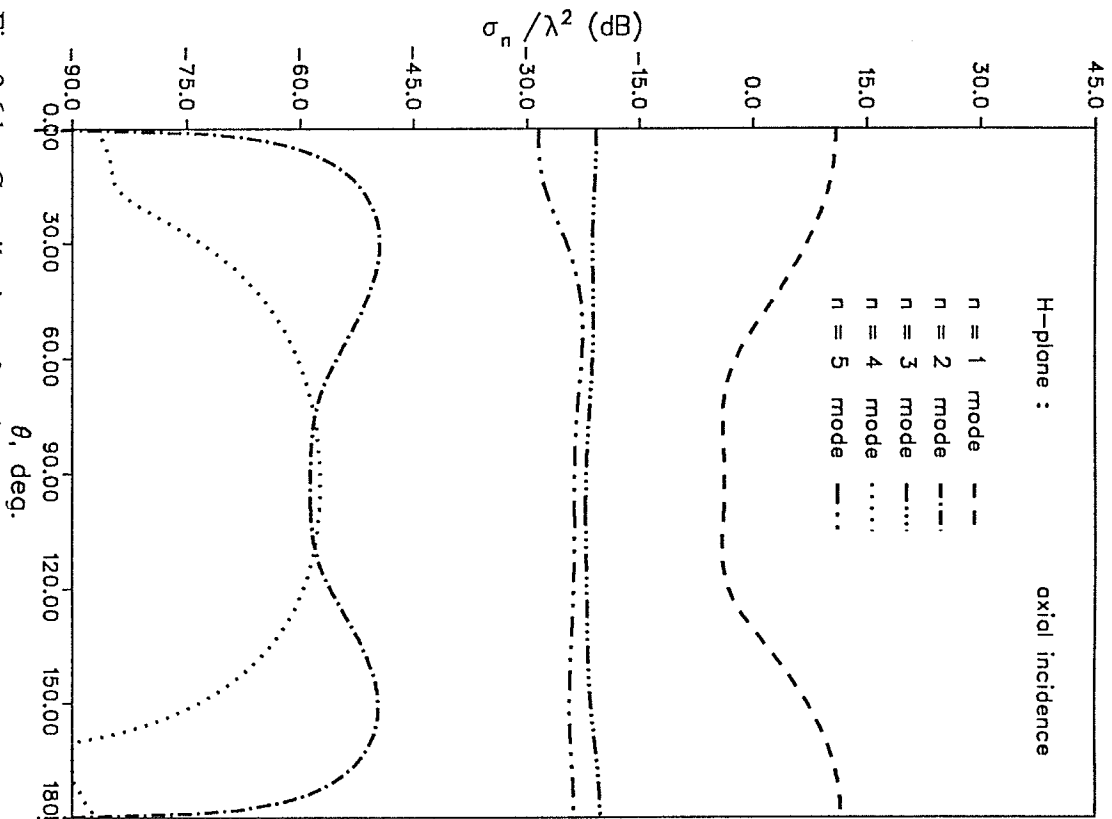


Fig. 3.6.b : Contribution of various modes to the bistatic scattering cross-section of a conducting square plate of side length $L = 1.0 \lambda$ and thickness $t = 0.1 \lambda$ for a plane wave incidence.

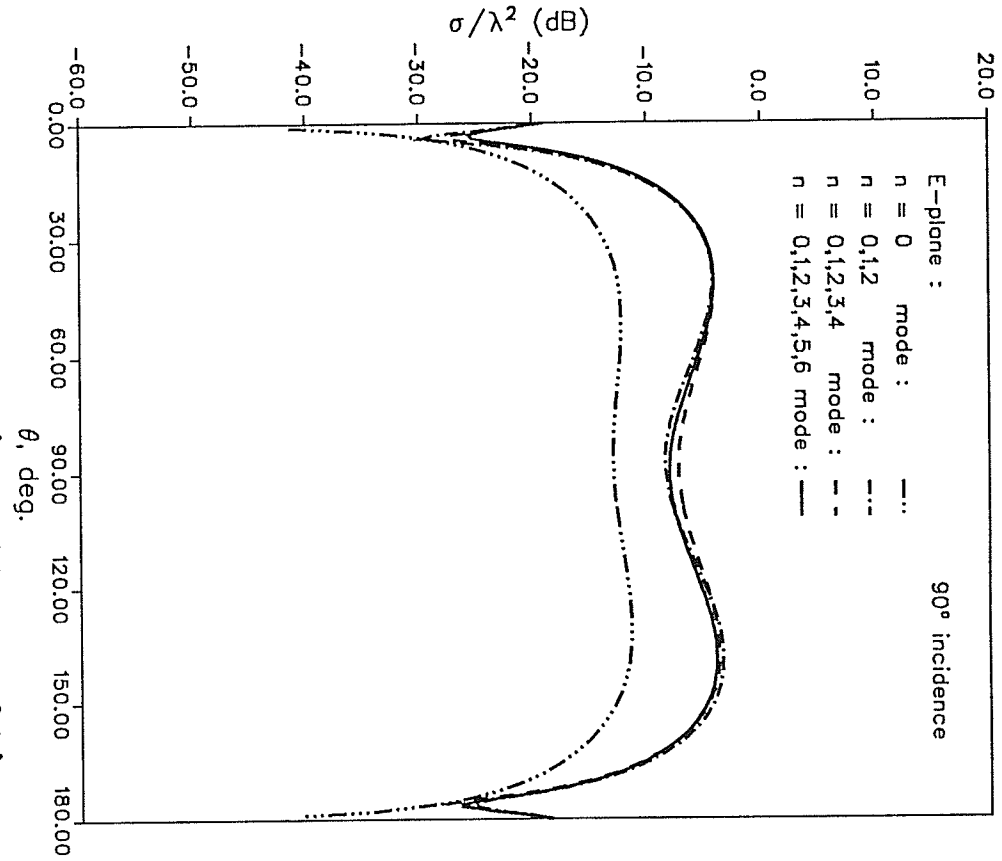
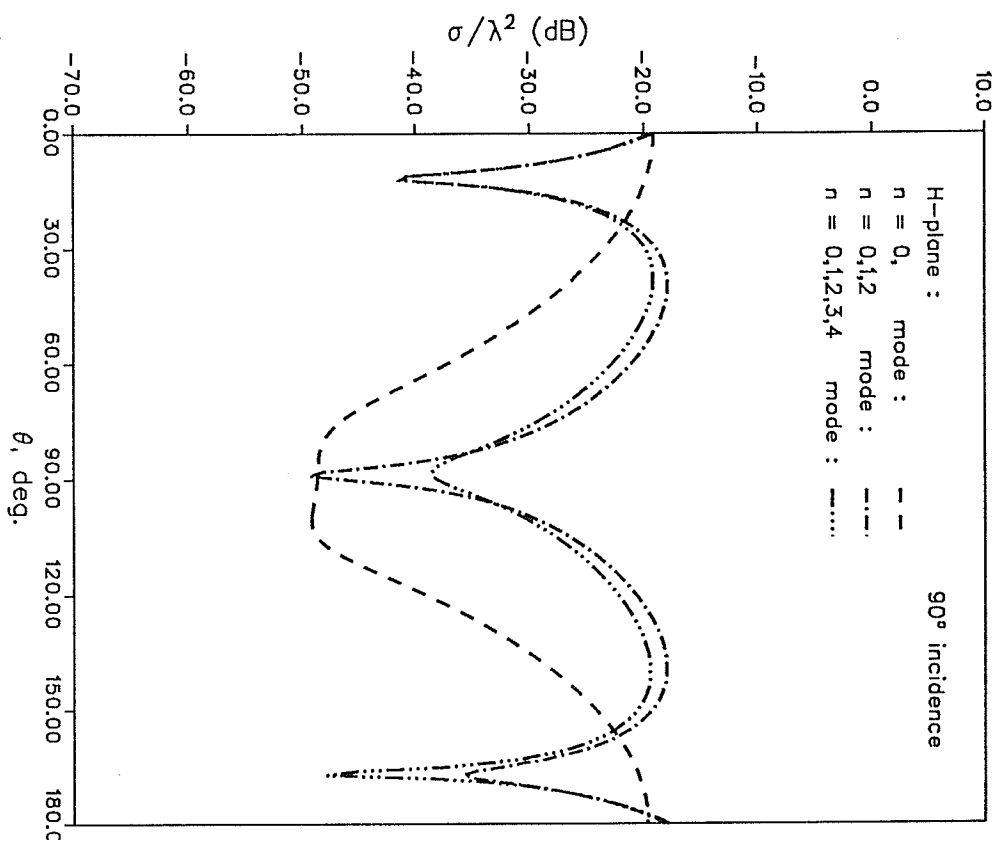


Fig. 3.7.a : Bistatic scattering cross-section of a conducting square plate of side length $L = 1.0 \lambda$ and thickness $t = 0.1 \lambda$, for a oblique incident plane wave.

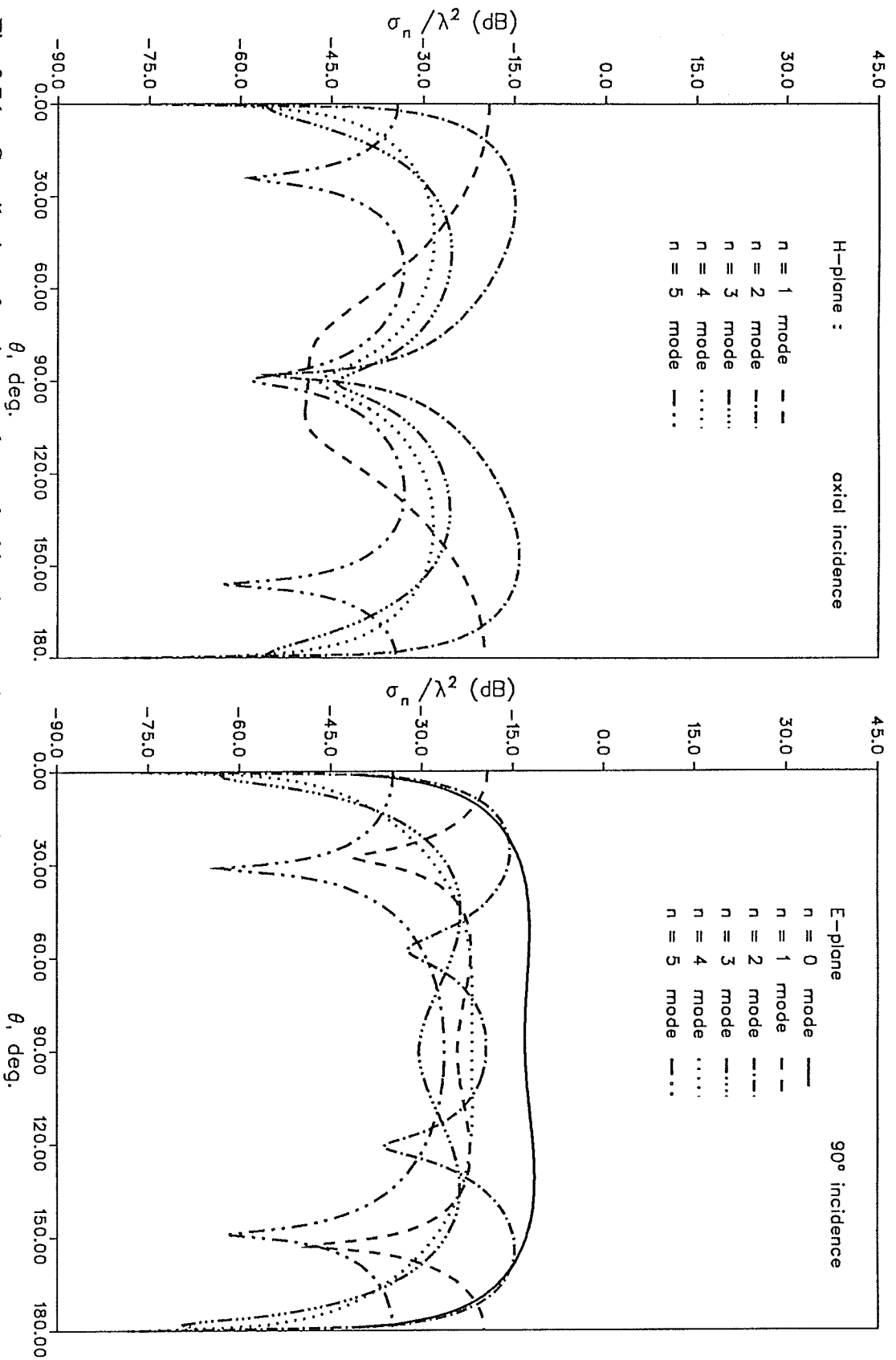


Fig. 3.7.b : Contribution of various modes to the bistatic scattering cross-section of a conducting square plate of side length $L = 1.0 \lambda$ and thickness $t = 0.1 \lambda$ for a plane wave incidence.

Chapter 4

Scattering from dielectric objects

4.1. Introduction

The electromagnetic problems involving three-dimensional dielectric structures have found continuing interest from investigators in both areas of radar scattering and antennas. Classical solutions involving expansions in terms of cylindrical, spherical and spheroidal wave functions, exist only for a limited classes of geometries, where separation of variables may be invoked. As a result, problems extensively investigated in the past are the scattering from dielectric spheres, in the form of Mie series [41], and spheroids in terms of spherical Legendre expansions [43]. With the advent of numerical techniques based on the moment methods, two different methods have been developed successfully to solve the scattering from dielectric bodies of arbitrary shape. They are formulated using, the volume, and surface integral equations.

The volume integral equation formulation was first presented by Richmond [67], [68], for investigation of two-dimensional structures. Lately, in using this method several authors [44]-[54], have utilized different basis functions together with the method of moment to investigate three dimensional dielectric structures. In this method, the scattered field is expressed in terms of an equivalent volume distribution of the polarization electric current, which exists in the dielectric, and radiates in free space. Utilizing the free space Green function, a combined volume and surface integral equations can be obtained to relate the unknown current density to the known incident field.

The surface integral equation formulation has been used by several authors to investigate the scattering properties of both two- and three-dimensional objects. It was initially applied to two-dimensional dielectrics of arbitrarily cross-section [69], [70] and finite dielectric cylinders [43], and recently to bodies of revolution [47], [48]. In this method, the original problem is reduced to two equivalent ones, involving the external and internal media. The scattered fields inside and outside of the dielectric medium are then expressed in terms of unknown equivalent electric and magnetic currents on the dielectric surface and radiating in an unbounded medium. These currents are determined by solving a set of coupled integral equations, which are developed by an application of the boundary conditions on the tangential components of the total fields.

The above two formulations have their own distinct advantage or disadvantages. For instance, the surface formulation is feasible for homogeneous dielectrics and is more efficient when the geometry is large. Whereas, the volume formulation is effective when the object is thin, in the form of a slab [52]. However, the size of the moment matrix increases rapidly with the object's size in the volume formulation. At the present time, the practical applications of numerical techniques, as applied to dielectric media, are limited to small objects, since they require extensive computer memory and time.

In this chapter the surface integral equation is adopted for investigation of arbitrary dielectric objects. An application of the boundary conditions leads to a set of four integral equations in which, a linear combination of them results in a coupled pair of equations that are solved numerically. Both the coordinate transformation method (*CTM*) and the direct method (*DM*), which were used previously for conducting bodies of arbitrary shape, are extended to treat dielectric bodies of arbitrary shape. The magnetic and electric field operators are, consequently, the same as those developed in chapter two and three for the conducting objects. By selecting different boundary con-

ditions, five different formulations of the surface integral equation can be obtained, which are solved by utilizing hybrid type basis functions. The technique is applied to study the radar cross-section of complex geometries such as, dielectric cubes and prisms. Because of a large computer time requirement, the method is most useful for investigation of small objects.

4.2. Analysis

The required formulation may be found from the equivalence principle. Fig. 4.1 illustrates the general problem, where an electromagnetic field propagating in the medium of permittivity ϵ_e and permeability μ_e is incident upon the surface of a homogeneous dielectric object of permittivity ϵ_d and permeability μ_d . The unknown fields in the exterior region consist of the scattered fields \mathbf{E}^s , \mathbf{H}^s , and in the interior region is the diffracted fields \mathbf{E}^d , \mathbf{H}^d , respectively. According to the equivalence principle, the boundary equations can be specified as;

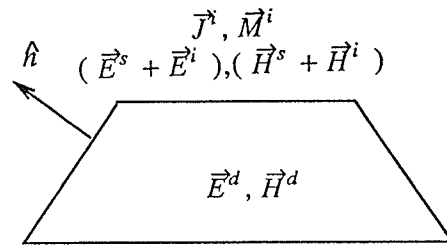
$$-\hat{n} \times \mathbf{E}_e^- = \hat{n} \times \mathbf{E}^i \quad \text{just inside } S \quad (4.1)$$

$$-\hat{n} \times \mathbf{H}_e^- = \hat{n} \times \mathbf{H}^i \quad \text{just inside } S \quad (4.2)$$

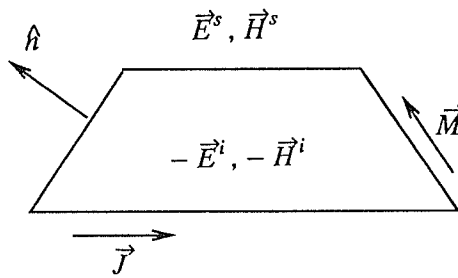
$$-\hat{n} \times \mathbf{E}_d^+ = 0 \quad \text{just outside } S \quad (4.3)$$

$$-\hat{n} \times \mathbf{H}_d^+ = 0 \quad \text{just outside } S \quad (4.4)$$

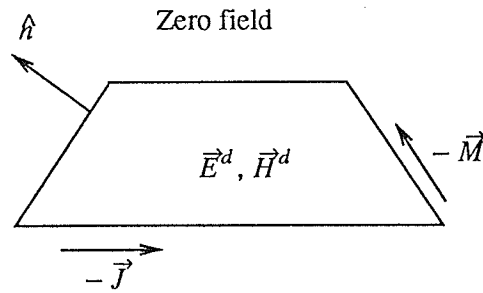
where \hat{n} is the unit vector normal to the surface S , the subscript e and d refer to the free space and the dielectric regions, superscript i indicates the incident field, and $-$, $+$ refer to the field just inside and outside S due to the equivalent surface currents \mathbf{J} and \mathbf{M} given by



(a)



(b)



(c)

Fig. 4.1. : (a) Original problem. (b) outside equivalence. (c) inside equivalence.

$$\mathbf{J} = \hat{n} \times \mathbf{H} \quad (4.5.a)$$

$$\mathbf{M} = \mathbf{E} \times \hat{n} \quad (4.5.b)$$

In order to obtain the equivalent electric and magnetic surface currents and subsequently the scattered field, one requires the reduction of equations (4.1) to (4.4) to a pair of suitable equations for these unknowns. A traditional preference is a linear combination of (4.1) and (4.4), or, a linear combination of (4.2) and (4.4) which can be written as

$$-\hat{n} \times [\mathbf{E}_e^- + \alpha \mathbf{E}_d^+] = \hat{n} \times \mathbf{E}^i \quad (4.6.a)$$

$$-\hat{n} \times [\mathbf{H}_e^- + \beta \mathbf{H}_d^+] = \hat{n} \times \mathbf{H}^i \quad (4.6.b)$$

where α and β are complex constants. The choice of $\alpha = \beta = 1$ has been used by several authors; Poggio and Miller, Chang and Harrington, and Wu, and the resulting expression is called the *PMCHW* formulation [47]. A selection of $\alpha = -\frac{\epsilon_d}{\epsilon_e}$, $\beta = -\frac{\mu_d}{\mu_e}$ results in the formulation purposed by Müller [71]. These two formulations are used by Mautz and Harrington to solve the scattering from homogeneous dielectric bodies of revolution. Other linear combinations are also available such as, the *E*-, *H*-, and *C*-field formulations. They are used by Kishk and Shafai [72], to solve the scattering from homogeneous and lossy dielectric bodies of revolution. A selection of (4.1) and (4.3) results in the *E*-field formulation given by,

$$-\hat{n} \times \mathbf{E}_e^- = \hat{n} \times \mathbf{E}^i \quad (4.7.a)$$

$$-\hat{n} \times \mathbf{E}_d^+ = 0 \quad (4.7.b)$$

and a selection of (4.2) and (4.4) results in the *H*-field formulation as;

$$-\hat{n} \times \mathbf{H}_e^- = \hat{n} \times \mathbf{H}^i \quad (4.8.a)$$

$$-\hat{h} \times \mathbf{H}_d^+ = 0 \quad (4.8.b)$$

A linear combination of (4.1) and (4.2) together with a linear combination of (4.3) and (4.4) results in the C -field formulation which is;

$$-\hat{h} \times \left[\gamma \frac{\mathbf{E}_e^-}{\eta_e} + \mathbf{H}_e^- \right] = \hat{h} \times \left[\gamma \frac{\mathbf{E}_e^i}{\eta_e} + \mathbf{H}_e^i \right] \quad (4.9.a)$$

$$-\hat{h} \times \left[\gamma \frac{\mathbf{E}_d^+}{\eta_e} + \mathbf{H}_d^+ \right] = 0 \quad (4.9.b)$$

where, γ is a positive real weighting factor, and the electric field operator should be divided by the intrinsic impedance of the exterior medium to equalize the dimensions of the electric and magnetic field operators. Each set of the above coupled surface integral equations is adequate to determine the surface currents \mathbf{J} and \mathbf{M} .

4.3. Matrix Formulation

The evaluation of the equivalent surface currents \mathbf{J} and \mathbf{M} may be achieved through an application of the moment methods. This involves expanding the unknown currents, along two orthogonal tangent vectors \hat{t} and \hat{s} on the dielectric surface, in terms of appropriate basis function, such as

$$\mathbf{J} = \sum_{n=-\infty}^{\infty} \sum_{j=1}^N a_{nj}^p J_{nj}^p \quad (4.10.a)$$

$$\mathbf{M} = \eta_e \sum_{n=-\infty}^{\infty} \sum_{j=1}^N b_{nj}^p J_{nj}^p \quad (4.10.b)$$

where, p is either t , or s on the object's surface, as defined by equations (2.5) and (2.6), a_{nj}^p and b_{nj}^p are current expansion coefficients to be determined and J_{nj}^p are the products of the hybrid basis functions, i.e., the entire domain and subdomain basis functions, as defined in the previous chapters.

In order to simplify the generation of the moment matrix for the formulations of (4.5) to (4.9), one should note that, the operator for determining \mathbf{E} from \mathbf{M} is the negative of the operator for determining \mathbf{H} from \mathbf{J} . Also, the operator that gives \mathbf{H} from \mathbf{M} is equivalent to the operator that gives \mathbf{E} from \mathbf{J} when it is divided by the square of the intrinsic impedance of the region.

In view of the above considerations together with the boundary conditions and the current expansions of (4.10), the integral equation can be reduced to a general matrix equation of the form

$$\sum_{n=-\infty}^{\infty} \sum_{j=1}^N (T_{mng}^{pq})_{ij} c_{nj}^p = E_{mi}^p \quad m = 0, \pm 1, \pm 2, \dots \quad (4.11)$$

where $(T_{mng}^{pq})_{ij}$ is a square matrix representing the impedance and admittance submatrices, c_{nj}^p is a column matrix for the unknown coefficients \mathbf{J} and \mathbf{M} , g is either e or d , and E_{mi}^p is the excitation column matrix. In the following sections the required boundary conditions and the corresponding matrices are provided.

4.3.1. *PMCHW* and *Müller* matrices

In this section, the general matrix formulation for the *PMCHW* and *Müller* solutions is presented. The reduction of the integral equations to a matrix equation follows the boundary conditions given by,

$$\left[-\frac{1}{\eta_e} \mathbf{E}_e(\mathbf{J}) + \frac{1}{\eta_e} \mathbf{H}_e^-(\mathbf{M}) - \frac{\alpha}{\eta_e} \mathbf{E}_d(\mathbf{J}) + \frac{\alpha}{\eta_e} \mathbf{H}_d^+(\mathbf{M}) \right]_{\text{tan}} = \frac{1}{\eta_e} \mathbf{E}_{\text{tan}}^i \quad (4.12.a)$$

$$-\hat{\mathbf{h}} \times \left[\mathbf{H}_e^-(\mathbf{J}) + \frac{1}{\eta_e^2} \mathbf{E}_e(\mathbf{M}) + \beta \mathbf{H}_d^+(\mathbf{J}) + \frac{\beta}{\eta_d^2} \mathbf{E}_d(\mathbf{M}) \right] = \hat{\mathbf{h}} \times \mathbf{H}^i \quad (4.12.b)$$

Utilizing the above boundary conditions and procedures for application of the moment methods, one can develop a matrix equation for the unknown current coefficients as,

$$\sum_{n=-\infty}^{\infty} \begin{bmatrix} (Y_{mne}^{st} + \alpha Y_{mnd}^{st}) & (Y_{mne}^{ss} + \alpha Y_{mnd}^{ss}) & (Z_{mne}^{tt} + \alpha \eta_r Z_{mnd}^{tt}) & (Z_{mne}^{ts} + \alpha \eta_r Z_{mnd}^{ts}) \\ (-Y_{mne}^{tt} - \alpha Y_{mnd}^{tt}) & (-Y_{mne}^{ts} - \alpha Y_{mnd}^{ts}) & (Z_{mne}^{st} + \alpha \eta_r Z_{mnd}^{st}) & (Z_{mne}^{ss} + \alpha \eta_r Z_{mnd}^{ss}) \\ (Z_{mne}^{st} + \frac{\beta}{\eta_r} Z_{mnd}^{st}) & (Z_{mne}^{ss} + \frac{\beta}{\eta_r} Z_{mnd}^{ss}) & (Y_{mne}^{tt} + \beta Y_{mnd}^{tt}) & (Y_{mne}^{ts} + \beta Y_{mnd}^{ts}) \\ (-Z_{mne}^{tt} - \frac{\beta}{\eta_r} Z_{mnd}^{tt}) & (-Z_{mne}^{ts} - \frac{\beta}{\eta_r} Z_{mnd}^{ts}) & (Y_{mne}^{st} + \beta Y_{mnd}^{st}) & (Y_{mne}^{ss} + \beta Y_{mnd}^{ss}) \end{bmatrix}^* \begin{bmatrix} b_n^t \\ b_n^s \\ a_n^t \\ a_n^s \end{bmatrix} = \begin{bmatrix} V_m^t \\ V_m^s \\ I_m^t \\ I_m^s \end{bmatrix} \quad m = 0, \pm 1, \pm 2, \dots \quad (4.12.c)$$

4.3.2. E-field matrix

Using the equivalence principle and applying the boundary conditions on the surface of the dielectric object, results in the following equations for the E -field formulation,

$$\frac{1}{\eta_e} \left[-\mathbf{E}_e^-(\mathbf{J}) + \mathbf{H}_e^-(\mathbf{M}) \right]_{\text{tan}} = \frac{1}{\eta_e} \mathbf{E}_{\text{tan}}^i \quad (4.13.a)$$

$$\frac{1}{\eta_e} \left[-\mathbf{E}_d^+(\mathbf{J}) + \frac{1}{\eta_e} \mathbf{H}_d^+(\mathbf{M}) \right]_{\text{tan}} = 0 \quad (4.13.b)$$

A substitution of the current expansion functions into (4.13) and an application of the moment method gives the required matrix equation of the E -field formulation as,

$$\sum_{n=-\infty}^{\infty} \begin{bmatrix} Z_{mne}^{tt} & Z_{mne}^{ts} & Y_{mne}^{st} & Y_{mne}^{ss} \\ Z_{mne}^{st} & Z_{mne}^{ss} & -Y_{mne}^{tt} & -Y_{mne}^{ts} \\ \eta_r Z_{mnd}^{tt} & \eta_r Z_{mnd}^{ts} & Y_{mnd}^{st} & Y_{mnd}^{ss} \\ \eta_r Z_{mnd}^{st} & \eta_r Z_{mnd}^{ss} & -Y_{mnd}^{tt} & -Y_{mnd}^{ts} \end{bmatrix} * \begin{bmatrix} a_n^t \\ a_n^s \\ b_n^t \\ b_n^s \end{bmatrix} = \begin{bmatrix} V_m^t \\ V_m^s \\ [0] \\ [0] \end{bmatrix} \quad m = 0, \pm 1, \dots \quad (4.13.c)$$

4.3.3. H-field matrix

Following the same procedure as discussed for the E -field formulation, one can obtain the required boundary conditions for the H -field solution

$$-\hat{h} \times [\mathbf{H}_e^-(\mathbf{J}) + \frac{1}{\eta_e^2} \mathbf{E}_e^-(\mathbf{M})] = \hat{h} \times \mathbf{H}^i \quad (4.14.a)$$

$$-\hat{h} \times [\mathbf{H}_d^+(\mathbf{J}) + \frac{1}{\eta_e^2} \mathbf{E}_d^+(\mathbf{M})] = 0 \quad (4.14.b)$$

in which the matrix equation takes the following form,

$$\sum_{n=-\infty}^{\infty} \begin{bmatrix} Y_{mne}^{tt} & Y_{mne}^{ts} & Z_{mne}^{st} & Z_{mne}^{ss} \\ Y_{mne}^{st} & Y_{mne}^{ss} & -Z_{mne}^{tt} & -Z_{mne}^{ts} \\ Y_{mnd}^{tt} & Y_{mnd}^{ts} & \frac{1}{\eta_r} Z_{mnd}^{st} & \frac{1}{\eta_r} Z_{mnd}^{ss} \\ Y_{mnd}^{st} & Y_{mnd}^{ss} & -\frac{1}{\eta_r} Z_{mnd}^{tt} & -\frac{1}{\eta_r} Z_{mnd}^{ts} \end{bmatrix} * \begin{bmatrix} a_n^t \\ a_n^s \\ b_n^t \\ b_n^s \end{bmatrix} = \begin{bmatrix} I_m^t \\ I_m^s \\ [0] \\ [0] \end{bmatrix} \quad m = 0, \pm 1, \dots \quad (4.14.c)$$

4.3.4. C-field matrix

The boundary conditions for the case of C -field formulation can be expressed as,

$$\frac{\gamma}{\eta_e} [-\mathbf{E}_e^-(\mathbf{J}) + \mathbf{H}_e^-(\mathbf{M})]_{\tan} - \hat{h} \times [\mathbf{H}_e^-(\mathbf{J}) + \frac{1}{\eta_e^2} \mathbf{E}_e^-(\mathbf{M})] = \frac{\gamma}{\eta_e} \mathbf{E}_{\tan}^i + \hat{h} \times \mathbf{H}^i \quad (4.15.a)$$

$$\frac{Y}{\eta_e} [-\mathbf{E}_d^+(\mathbf{J}) + \mathbf{H}_d^+(\mathbf{M})]_{\tan} - \hat{n} \times [\mathbf{H}_d^+(\mathbf{J}) + \frac{1}{\eta_2} \mathbf{E}_d^+(\mathbf{M})] = 0 \quad (4.15.b)$$

and final C -field matrix takes the form

$$\sum_{n=-\infty}^{\infty} \begin{bmatrix} (\gamma Z_{mne}^{tt} + Y_{mne}^{tt}) & (\alpha Z_{mne}^{ts} + Y_{mne}^{ts}) & (\gamma Y_{mne}^{st} + Z_{mne}^{st}) & (\gamma Y_{mne}^{ss} + Z_{mne}^{ss}) \\ (\gamma Z_{mne}^{st} + Y_{mne}^{st}) & (\gamma Z_{mne}^{tt} + Y_{mne}^{tt}) & (-\gamma Y_{mne}^{ss} - Z_{mne}^{ss}) & (-\gamma Y_{mne}^{ts} - Z_{mne}^{ts}) \\ (\gamma \eta_r Z_{mnd}^{tt} + Y_{mnd}^{tt}) & (\gamma \eta_r Z_{mnd}^{ts} + Y_{mnd}^{ts}) & (\gamma Y_{mnd}^{st} + \frac{1}{\eta} Z_{mnd}^{st}) & (\gamma Y_{mnd}^{ss} + \frac{1}{\eta} Z_{mnd}^{ss}) \\ (\gamma \eta_r Z_{mnd}^{st} + Y_{mnd}^{st}) & (\gamma \eta_r Z_{mnd}^{ts} + Y_{mnd}^{ts}) & (-\gamma Y_{mnd}^{tt} - \frac{1}{\eta} Z_{mnd}^{tt}) & (-\gamma Y_{mnd}^{ts} - \frac{1}{\eta} Z_{mnd}^{ts}) \end{bmatrix}^* = \begin{bmatrix} a_n^t \\ a_n^s \\ b_n^t \\ b_n^s \end{bmatrix} = \begin{bmatrix} \alpha V_m^t + I_m^t \\ \alpha V_m^s + I_m^s \\ [0] \\ [0] \end{bmatrix} \quad m = 0, \pm 1, \pm 2, \dots \quad (4.15.c)$$

In the above equations, the subscript \tan refers to the tangential components of the electric fields due to \mathbf{J} and \mathbf{M} , m and n are the Fourier modes indices, $\eta_r = \frac{\eta_d}{\eta_e}$,

$\eta_d = \sqrt{\frac{\mu_d}{\epsilon_d}}$, $\eta_e = \sqrt{\frac{\mu_e}{\epsilon_e}}$, and V_m^p and I_m^p are the excitation vectors defined as

$$V_{mi}^p = \frac{1}{\eta_e} \iint_s \mathbf{J}_{mi}^p \cdot \mathbf{E}^i ds \quad (4.16.a)$$

$$I_{mi}^p = \iint_s \mathbf{W}_{mi}^p \cdot \hat{n} \times \mathbf{H}^i ds \quad (4.16.b)$$

and the matrix elements are given by

$$(Y_{mng}^{pq})_{ij} = - \iint_s \mathbf{W}_{mi}^p \cdot \hat{n} \times \mathbf{H}_g (J_{nj}^q) ds \quad (4.17.a)$$

$$(Z_{mng}^{pq})_{ij} = - \frac{1}{\eta_g} \iint_s \mathbf{W}_{mi}^p \cdot \mathbf{E}_g (J_{nj}^q) ds \quad (4.17.b)$$

Here, p, q are either t or s , and g is e or d which denotes radiation in either μ_e, ϵ_e , or μ_d, ϵ_d medium.

The Y and Z submatrices are the same as those of chapter two or three, depending on the formulations (*CTM*, or *direct method*) used in the analysis. The solution of each matrix equation gives the unknown current coefficients, which are then used to determine the equivalent electric and magnetic currents and subsequently, the scattered field outside S .

4.4. Scattered field

The solution of the above matrix equations provides both electric and magnetic current distributions on the dielectric objects. Once they are computed the field external to the object can be determined, which at far distances, i.e., at a point (r_r, θ_r, ϕ_r) is given by

$$E_q = \frac{-j \omega \mu_e}{4 \pi r_r} e^{-jk_r r} F_q(\theta_r, \phi_r) \quad (4.18.a)$$

with

$$F_q(\theta_r, \phi_r) = \int_s (\mathbf{J} \cdot \hat{u}_q \pm \frac{1}{\eta_e} \mathbf{M} \cdot \hat{u}_q) e^{-j\mathbf{K}_e \hat{r}_r \cdot \hat{r}} ds \quad (4.18.b)$$

where k_r is the propagation vector of the plane wave arriving from the field point, λ is the wavelength, r_r is the distance between the origin and the measurement point, \hat{u}_q is the polarization of the receiving electric dipole (θ , or ϕ) at the far field measurement point, and + or -, given in (4.18.b), stands for θ and ϕ polarizations, respectively. The steps leading to these field computations are similar to those of chapter two and three, and omitted here for brevity. Finally, the scattering cross-section can be defined in terms of the scattered field as,

$$\frac{\sigma^{pq}}{\lambda^2} = 4 \pi r_r^2 \frac{|E_{pq}^s|^2}{|E^i|^2} \quad (4.18.c)$$

where E^i is the incident field as defined previously.

4.5. Numerical results

In order to verify the validity of the software, it was first applied to rotationally symmetric dielectric objects. The far scattered fields of geometries, such as dielectric sphere (Fig. 4.2), and finite cylinder were obtained and compared with those of the Mie series and numerical results of Mautz and Harrington [47]. All formulations were found to give satisfactory results in agreement with the reported data.

Next, the above matrix formulation in conjunction with the *CTM* method is applied to bodies of square cross-section. The required coordinate transformation of objects of square cross-section was formulated in chapter 2. A cube of size $L = 0.2 \lambda$, with different permittivities was investigated and the preliminary results for $\epsilon_r = 4, 9$ are shown in Fig. 4.3. In all cases, presented here, the integration of the Green's function is carried out using a Gauss Legendre quadrature formula of order 40 and the parameter γ is selected to be 0.2 which is an optimum value, as discussed in [73]. The computed far scattered fields, obtained with 6 expansion functions in the t -direction and modeled by four pulses in both interior and exterior regions are compared with the surface and volume integral formulations of [52]. The results for all five formulations are presented. Their accuracy seems satisfactory and predict both the forward and backward-scattering patterns with small differences in the E - and H -planes. The *Müller* solution has predicted the E -plane pattern quite accurately for the entire angular range. But, it has demonstrated discrepancy in the H -plane with other formulations specially, for the forward scattering, i.e. $\phi = 180^\circ$, where it differs by about 1.0 *dB* from other

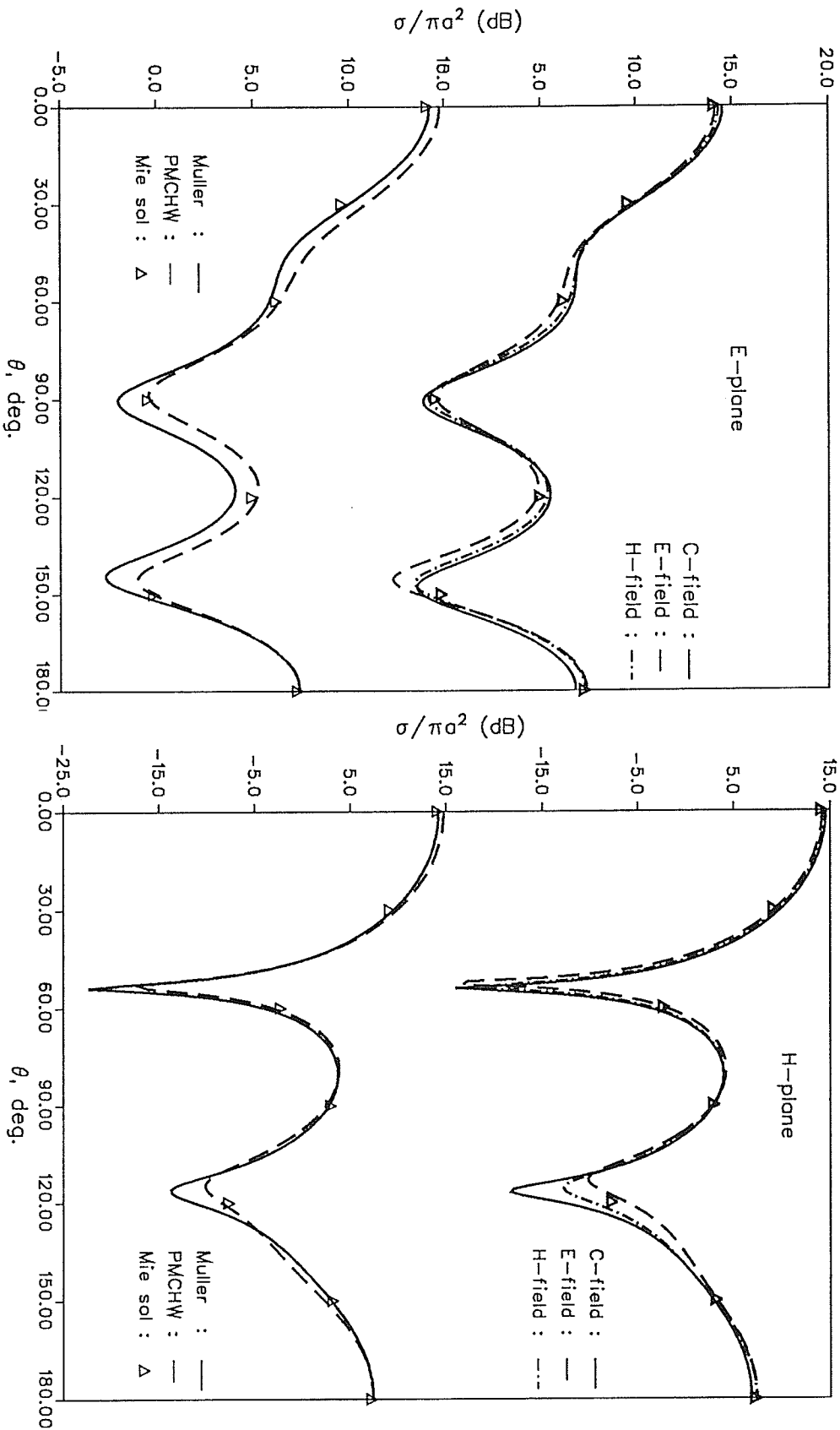


Fig. 4.2.a : E- and H-plane scattering patterns for a dielectric sphere, $ka = 3$, $\epsilon_r = 4$, for a normal incident plane wave.

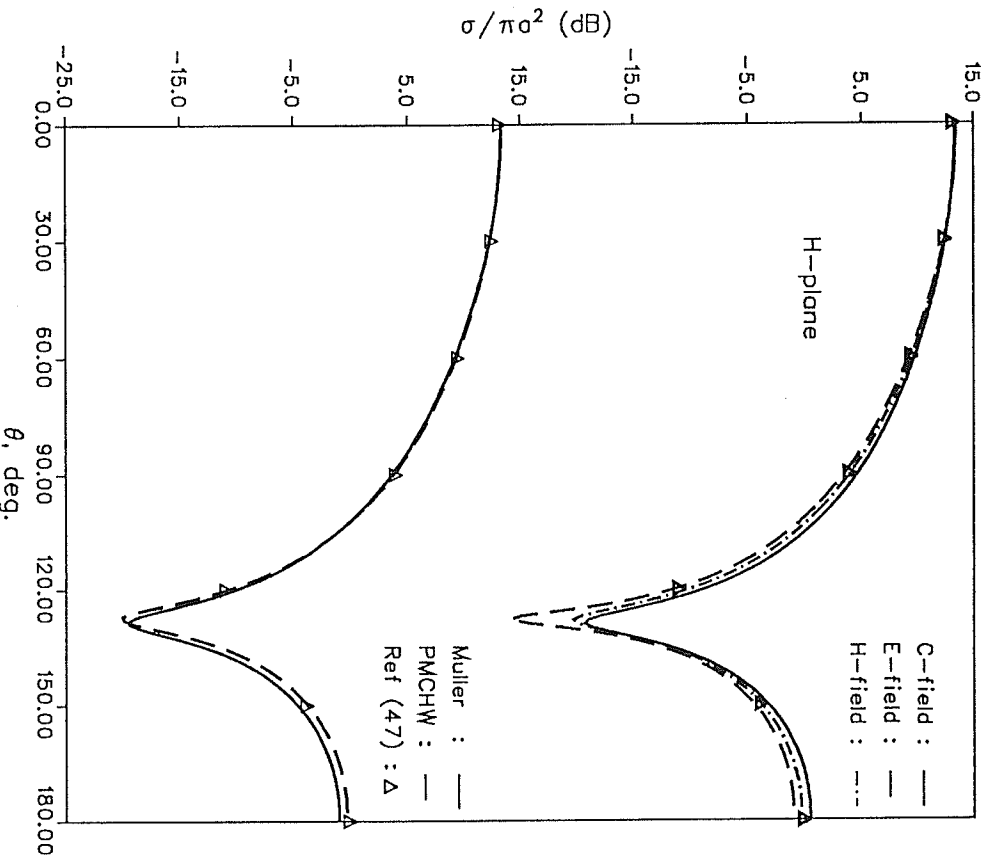
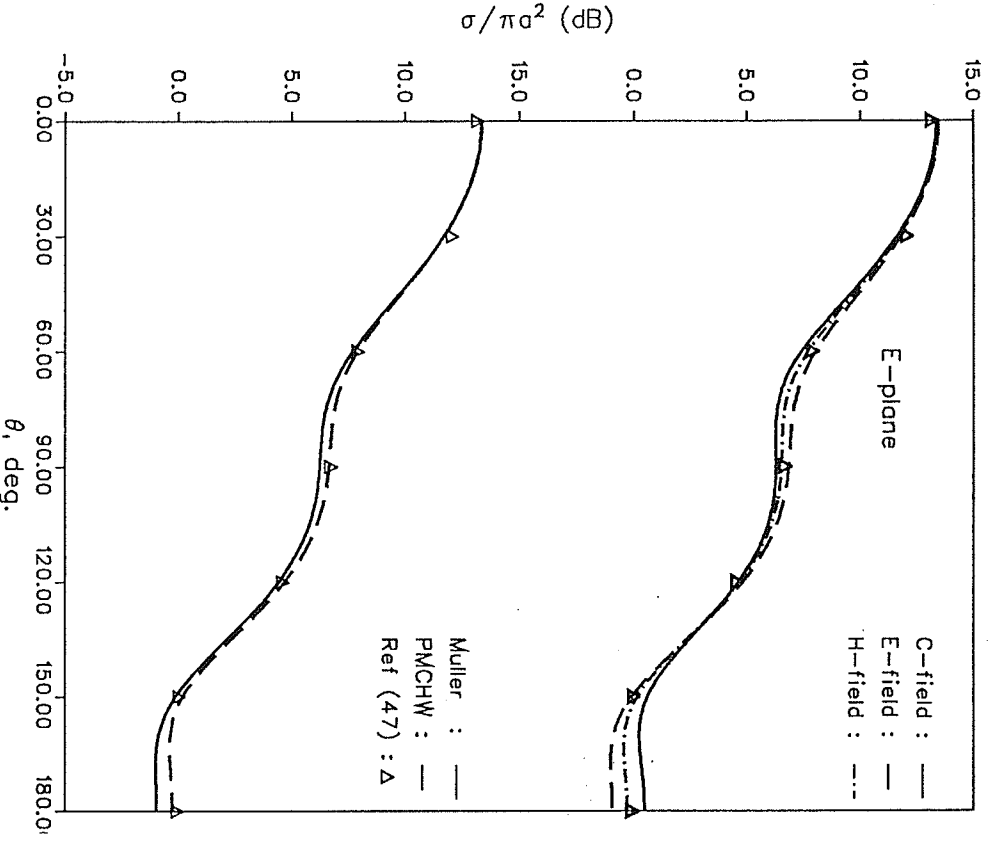


Fig. 4.2.b : E- and H-plane scattering patterns for a dielectric cylinder of radius, $a = 0.25\lambda$, height $h = 2a$, and $\epsilon_r = 4$, for a normal incident plane wave.

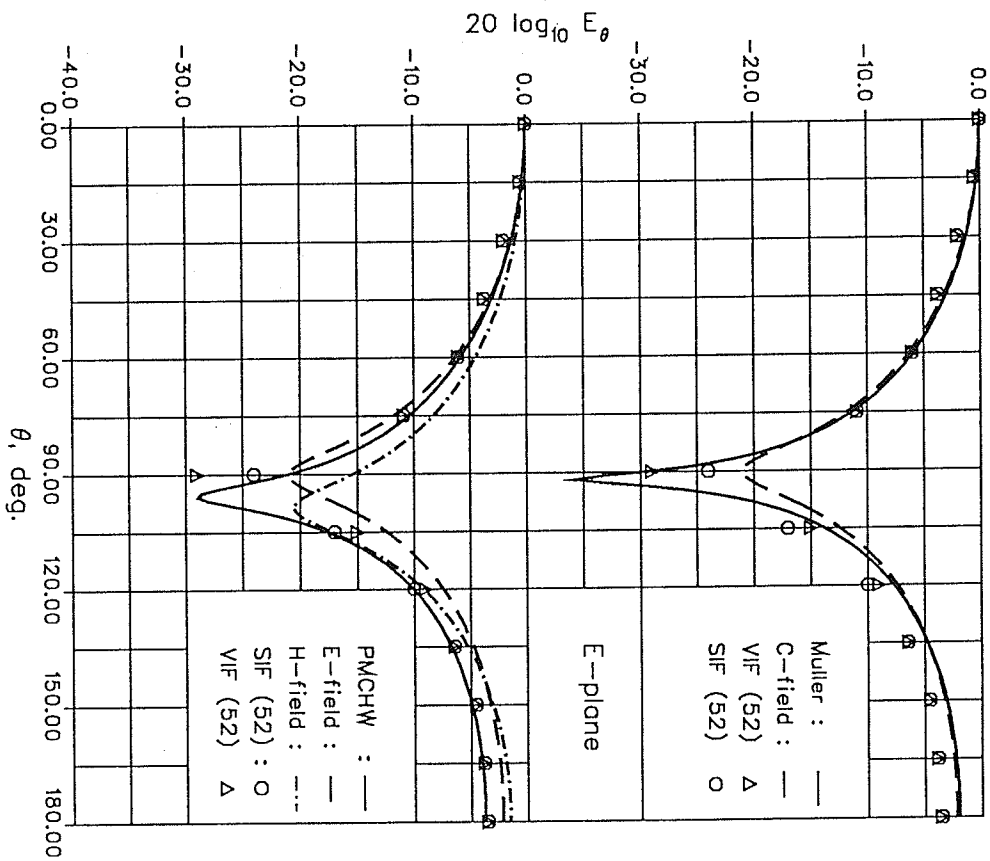
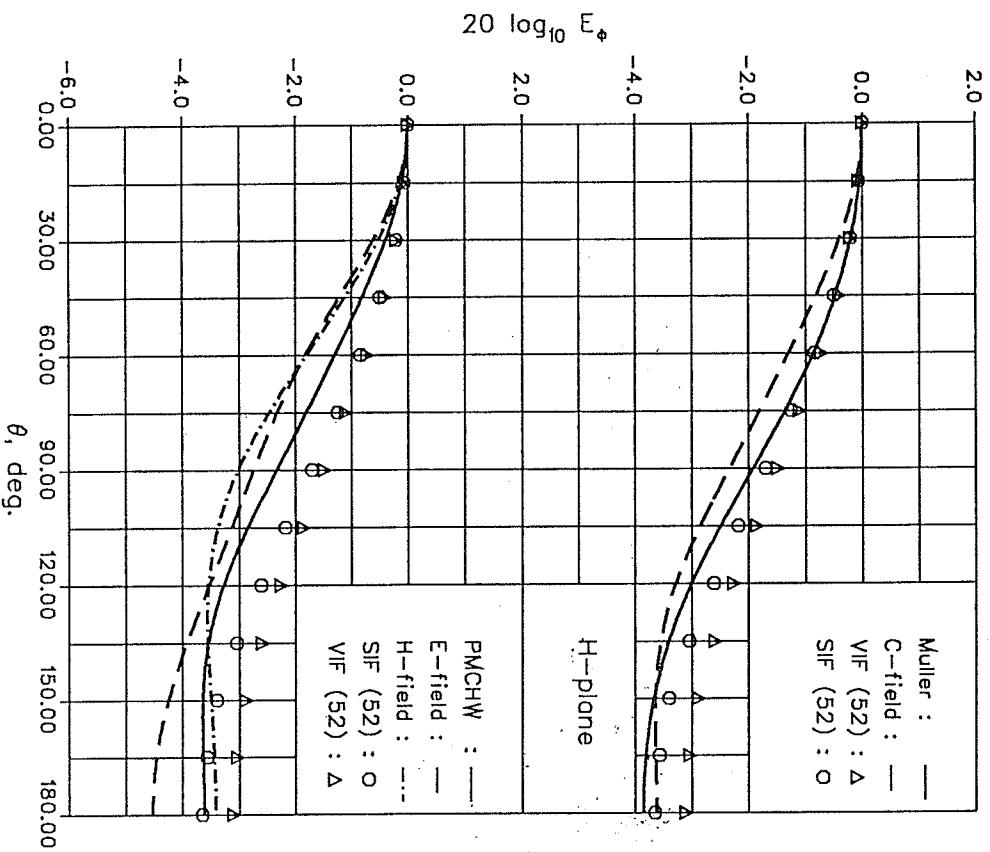


Fig. 4.3.a : Bistatic scattering patterns for a dielectric cube of size $L = 0.2\lambda$, $\epsilon_r = 4$, $n = 1$, and 4 pulses per triangle, for a normal incident plane wave.

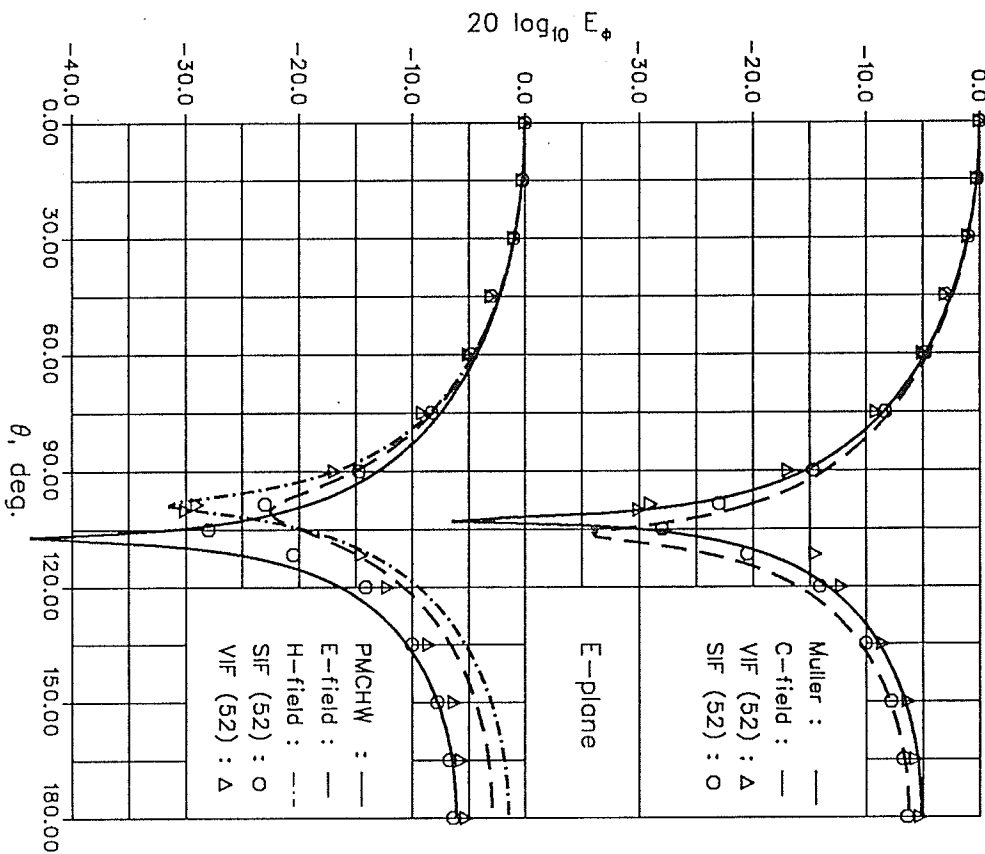
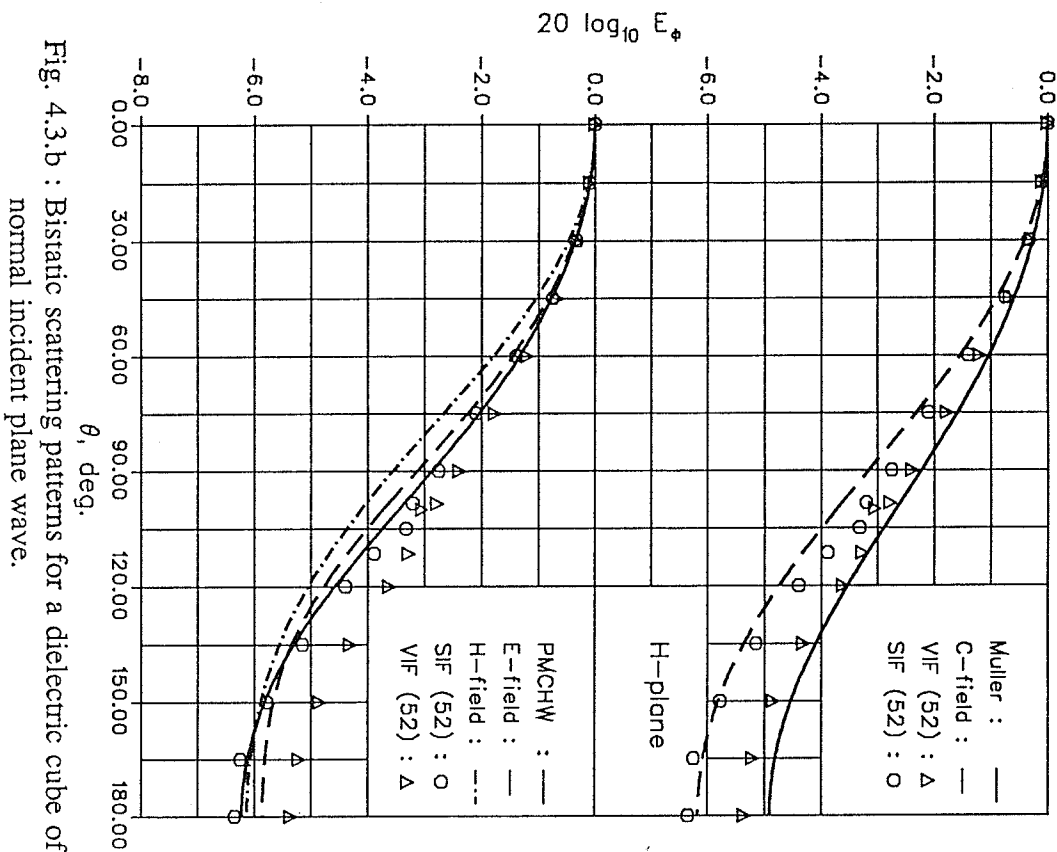


Fig. 4.3.b : Bistatic scattering patterns for a dielectric cube of size $L = 0.2\lambda$, $\epsilon_r = 9$, $n = 1$, and 4 pulses per triangle, for a normal incident plane wave.

solutions. The same argument held also to the formulations of [52]. The predicated forward scattering patterns by the E - and H -field solutions in the H-plane are unsatisfactory. Also, the C -field and $PMCHW$ solutions have shown a shift in the location of the null with other formulations. Otherwise, their results follow the same patterns as the other formulations.

Next a study was conducted to improve the accuracy of the solution, in particular the modeling of the t -directed triangular basis functions by introducing extra number of pulses representing the triangular functions, i.e., 4, 6, and 8. Usually the solution accuracy deteriorates as the dielectric constant of the medium increases specially, for the *Müller* solution which gives less accurate results for high dielectric constants [72]. The interior auxiliary problem is dependent on the permittivity of the medium, and as ϵ_r increases, a better modeling of the dielectric surface becomes necessary. To improve the accuracy of the integration schemes along the interior generating curve, one requires to increase the number of basis functions along the contour t , for a better representation of the surface current. Consequently, the matrix size increases and the present method becomes less efficient, for large dielectric constants. However, as it was discussed in chapter two for a conducting case and also in [72] for the dielectric bodies of revolutions, the number of pulses can be made proportional to the length of the generating curve of the body. In other words, in reducing the surface integral equation to a matrix equation, the surface current can be represented by a fix number of linear basis functions, regardless of the dielectric constant of the medium, by increasing the number of pulses per triangle. Subsequently, the matrix size becomes dependent only on the object's size and independent of the material permittivity. However, the overall computation time of the matrix elements increases.

To examine the dependence of the solution accuracy on the number of pulses in the dielectric region, the cases of $\epsilon_r = 4$, and 9 were further investigated. The number of linear basis functions was kept constant at 6, and also for the exterior region four

pulses were used for each triangle modeling. However, in the dielectric medium it was increased from 4 to 6 and 8. Figs. 4.4 illustrate the numerical computations based on a six pulse approximation. It is evident that the solution accuracy of all formulations is improved and the resulting scattering patterns are in excellent agreement with each other, except for the *PMCHW* solution in which only a slight improvement in the accuracy is noticed. Increasing the number of pulses to eight was found to have a negligible effect on the improvement of the results.

This study shows that the accuracy of the *Müller*, *E*- and *H*-field formulations improve considerably, in particular, at the forward scattering direction, by a better modeling of the triangular functions. Hence, to improve the accuracy of the solution, the interior region of the dielectric medium requires additional pulses to improve the numerical integration technique used over each triangle function. This in turn, leads to a higher precision in computation of the surface current coefficients. Since the length of the interior *t*-contour is multiplied by a factor of $\sqrt{\epsilon_r}$, one requires to take approximately $4\sqrt{\epsilon_r}$ number of pulses as suggested by [72]. However, as summerized in table 4.1, increasing the number of pulses requires extra computer time to compute the elements of the moment matrix. Nevertheless, in this manner, the matrix size becomes independent of the dielectric constant, and becomes depended only on the physical size of the object.

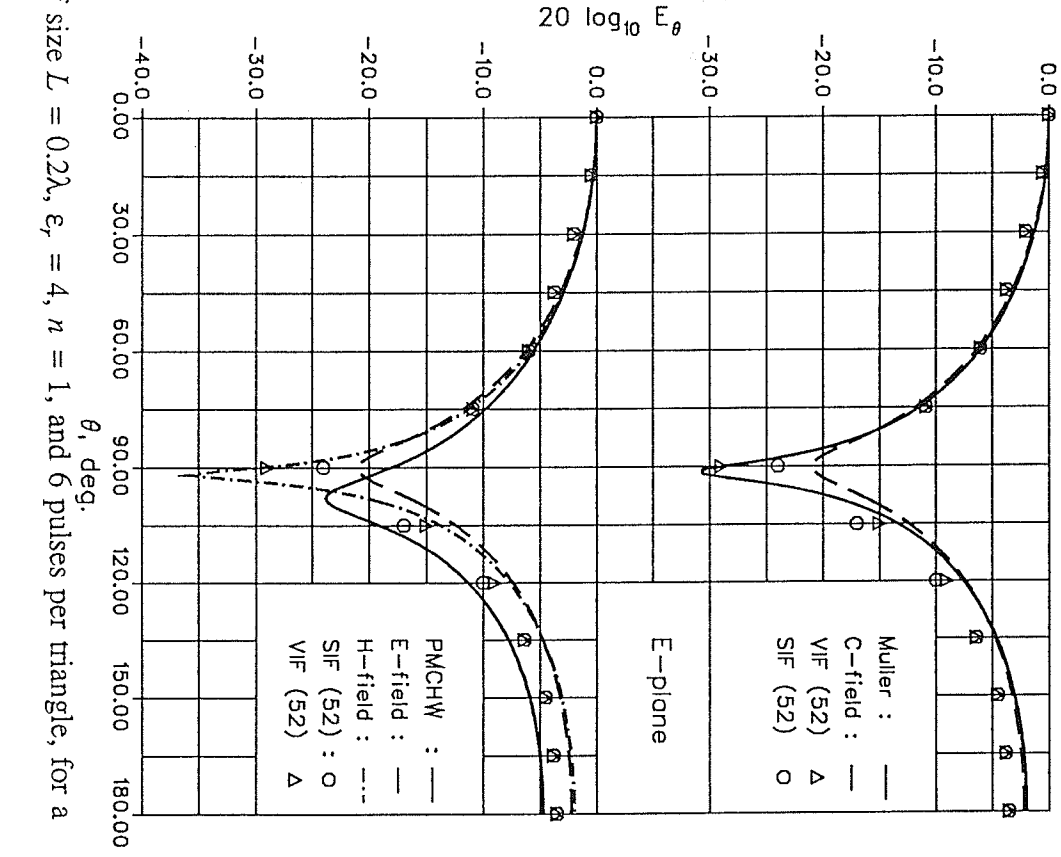
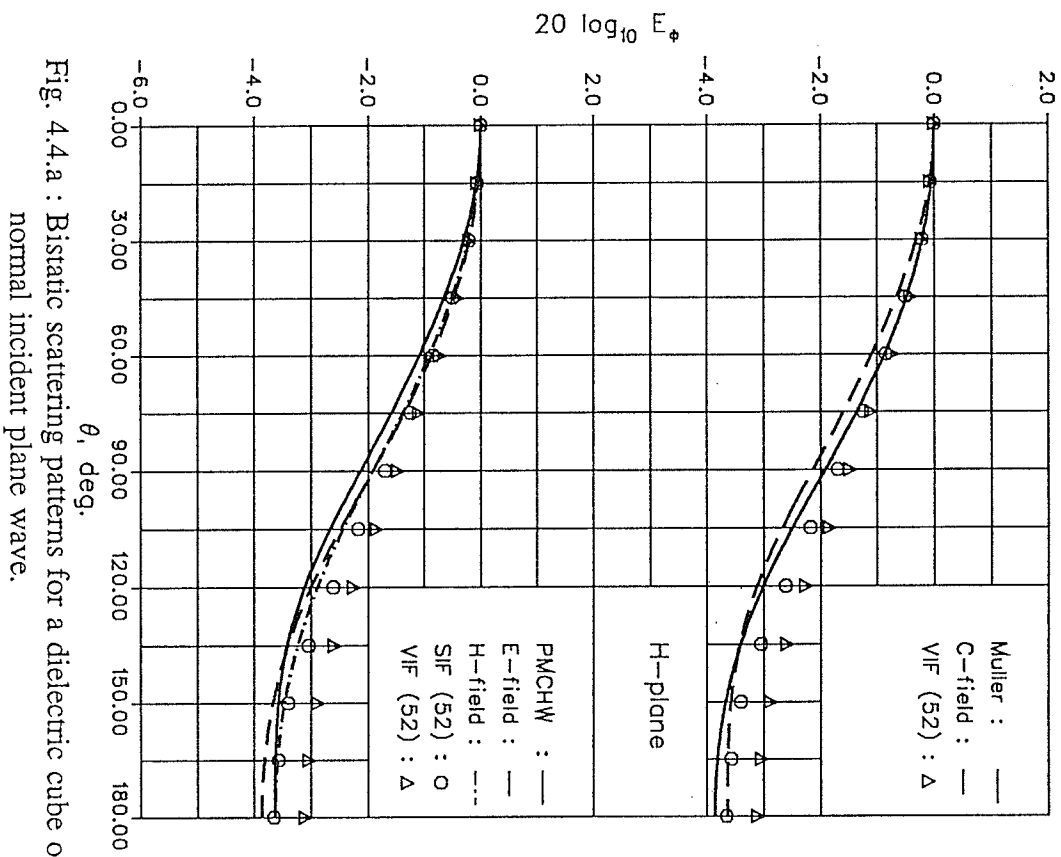


Fig. 4.4.a : Bistatic scattering patterns for a dielectric cube of size $L = 0.2\lambda$, $\epsilon_r = 4$, $n = 1$, and 6 pulses per triangle, for a normal incident plane wave.

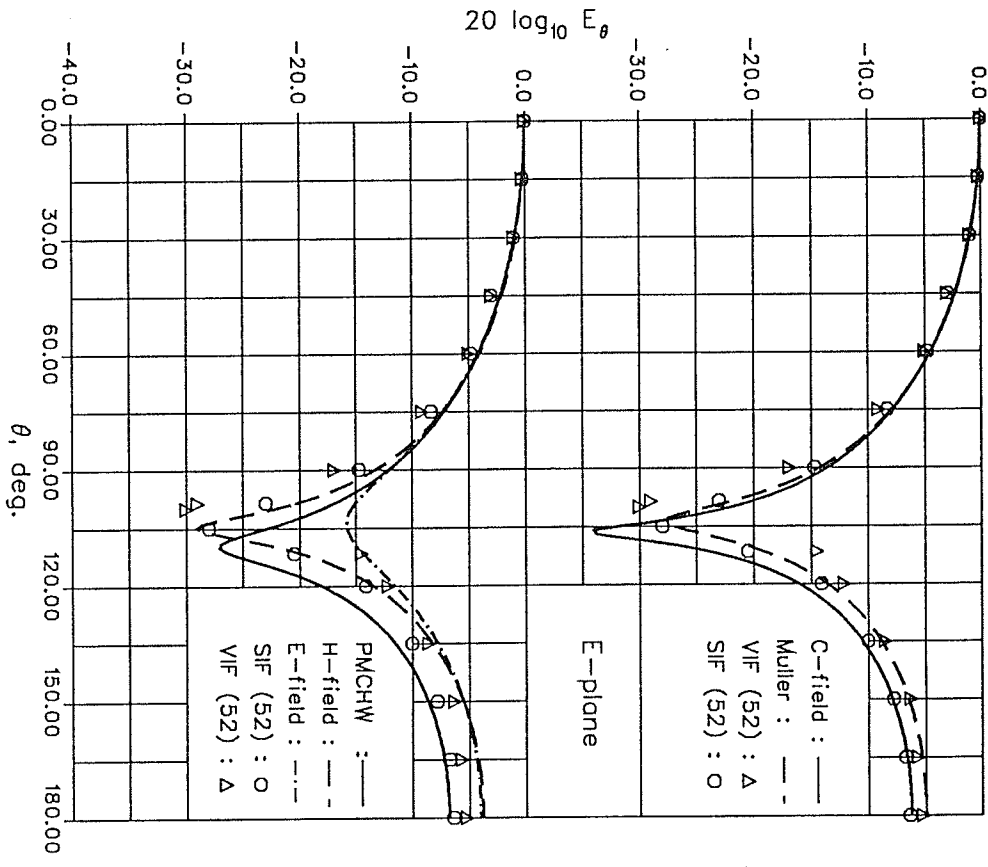
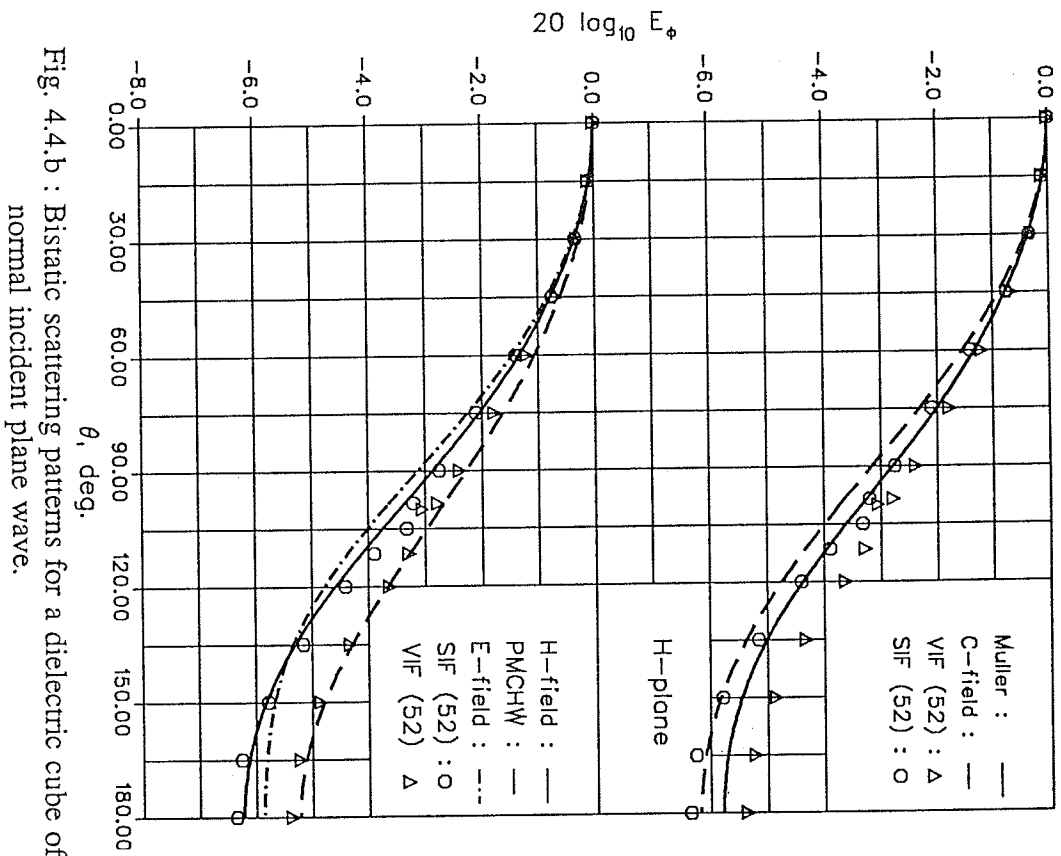


Fig. 4.4.b : Bistatic scattering patterns for a dielectric cube of size $L = 0.2\lambda$, $\epsilon_r = 9$, $n = 1$, and 6 pulses per triangle, for a normal incident plane wave.

Table 4.1

<i>NPE</i>	<i>NPI</i>	<i>No of triangles</i>	<i>No of pulses</i>	<i>No of Gauss</i>	<i>CPU* (sec.)</i>
15	15	6	4	40	120.
15	22	6	6	40	175.
15	29	6	8	40	280.

Table 4.1. Parameters used in computing the bistatic scattering patterns of a dielectric cube of size $L = 0.20 \lambda$. The CPU times are given for the Amdahl main frame, and NPE = Number of points used on the exterior generating curve, NPI = Number of points used on the interior generating curve.

* not an optimized value.

To study the convergence of the solutions in more details, the number of pulses was kept constant, i.e. 6, and the contributions of various modes to the scattering patterns were investigated. The selected results are illustrated in Figs. 4.5. to 4.9. The effect of individual mode on the scattered field stays relatively constant as the permittivity of cube changes from a small value of ϵ_r to a larger one.

Figs. 4.5 illustrates the strength of various modes and their effect on the scattered field of a dielectric cube of permittivities, 4, and 9, for the *Müller* formulation. The present computations show that for the broadside incidence the dominant mode is the $n = 1$ mode, and higher order modes do not contribute significantly to the scattered field, specially for the lower values of ϵ_r . In both E- and H-planes the higher order odd modes are present and couple together. However, they are at least 30 dB below the first mode and their relative level do not change significantly by increasing ϵ_r .

As illustrated in Figs. 4.6 and 4.7 the effect of mode coupling is similar also for the E- and H-field formulations, being slightly higher for small values of ϵ_r and decreases as the dielectric constant of the medium increases. Here, similar to the *Müller* formulation, the higher order odd modes, i.e., $n = 3, 5$, couple strongly on the surface, and are approximately 30dB below the dominant mode, i.e., $n = 1$. However, for the

E -field solution the presence of the $n = 5$ mode is slightly higher, in the forward scattering direction. Nevertheless, it is still considerably below the first mode, $n = 1$. As the permittivity of the material increases the strength of the higher order modes decreases by a small value, and for $\epsilon_r = 9$ the coupled modes are about 35 dB below the first one.

The corresponding results for the C -field, and $PMCHW$ solutions are shown in Figs 4.8 and 4.9, and indicate similar behaviors as the *Müller* formulation.

Finally, a study was done to compare the CTM and the DM formulations for dielectric objects. A cube of a side length $L = 0.2565 \lambda$ and a relative permittivity of 4 was considered. The computed numerical results are depicted in Figs. 4.10. The *Müller* formulation was used to compare their results. For the selected geometry the results of the above two techniques are in excellent agreement, in the H-plane, except for the forward scattering, where the two techniques differ by approximately 1.0dB. In the E-plane the generated results are satisfactory, except at the null location. However, computed results obtained using the direct method require additional Fourier modes, i.e., $n = 2, 3$, to converge. Consequently, the DM method requires extra computer time to compute the elements of the moment matrix, that leads to a less efficient numerical technique. This trend was also observed for the conducting case, where extra Fourier modes were needed to improve the performance of the DM method.

4.6. Conclusions

The electromagnetic scattering from dielectric bodies of arbitrary shape was investigated by extending the method of previous chapter for conducting objects to the dielectric ones. The formulations used the Schelkunoff's equivalence principle and cast the scattered field in terms of equivalent currents, located on the object's surface.

It resulted in a coupled set of integral equations for the unknown currents, which were then reduced to matrix equations using the moment methods. By selecting appropriate boundary conditions five different formulations were feasible and resulted in their corresponding matrix equations. Similar to conducting objects, these matrix equations were generated from the integral equations by expanding the unknown currents in terms of sub-domain triangular and entire domain exponential functions. The developed methods were then applied to different geometries, in particular, to cubes. The behavior of the solutions were examined and the degree of azimuthal mode coupling were studied. It was found that for dielectric objects, the representation of triangular basis functions by pulses is satisfactory, provided their number for the dielectric region is increased over that of free space region. This meant, selecting 4 pulses for the free space region, required that their number for the dielectric region be increased approximately by $4\sqrt{\epsilon_r}$. The effect of mode coupling was also investigated for the normal incidence of the plane wave. It was found that, for all formulations the dominant mode was the $n = 1$ mode, and higher order odd modes coupled together, but were considerably below the first one. For the selected incident angle, the even modes did not contribute to the scattered field. The present formulation resulted in a moment matrix which was independent of the material permittivity. The accuracy of the solution was verified by comparing the result of each individual formulation with one another and also with the numerical results found in the literature.

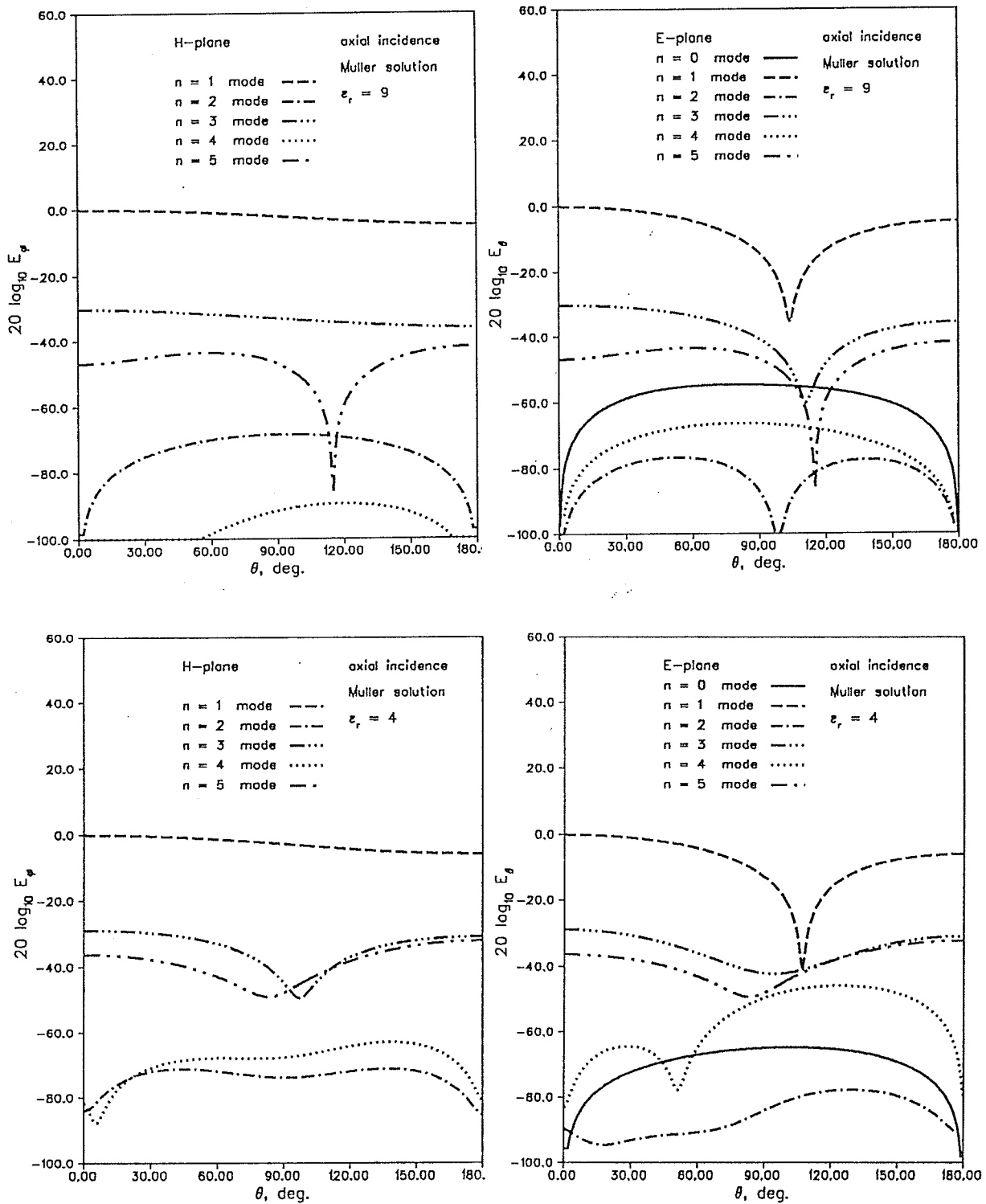


Fig. 4.5 : Contribution of various modes to the bistatic scattering cross-section of a dielectric cube of side length $L = 0.2\lambda$, for a normal incident plane wave.

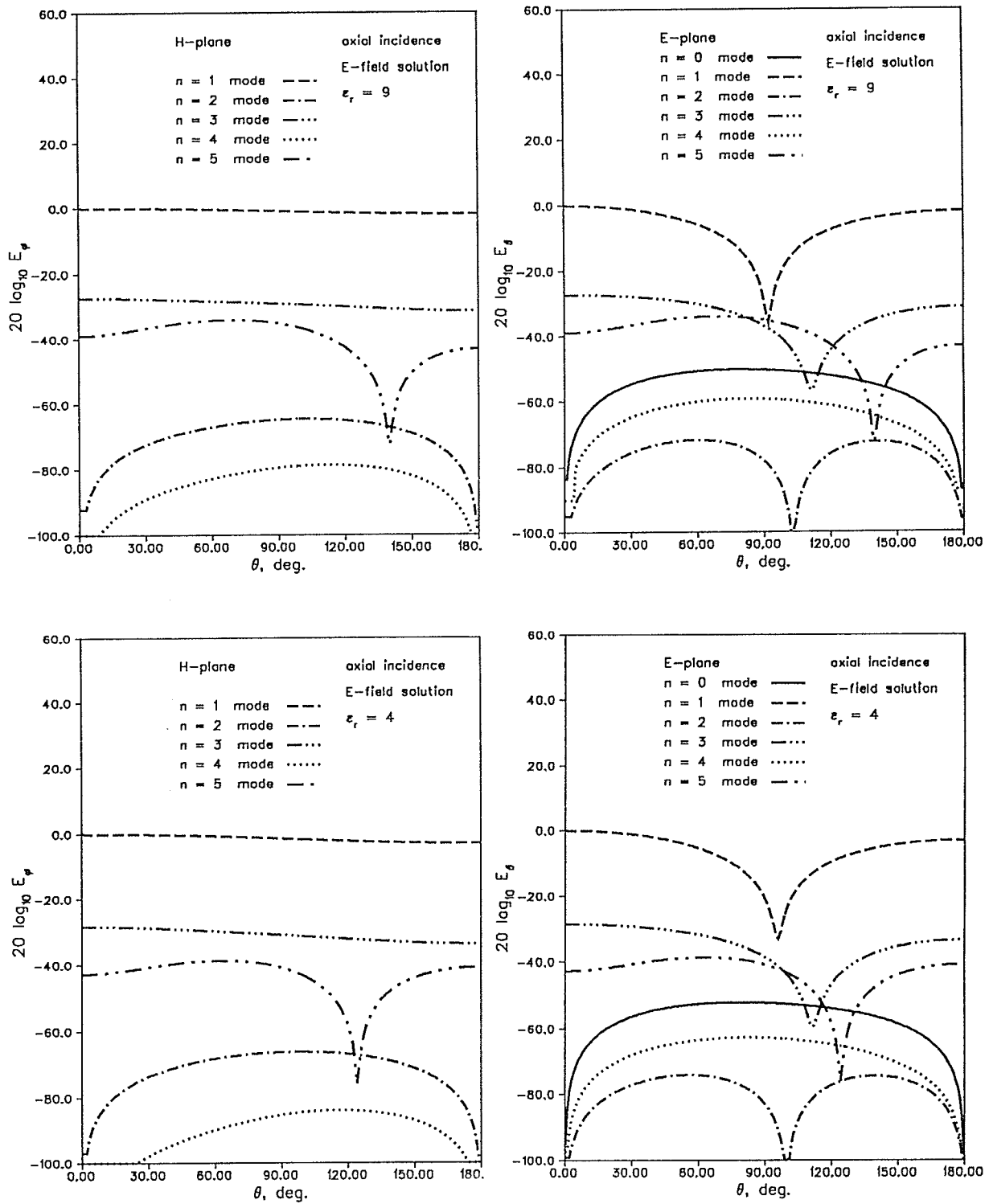


Fig. 4.6 : Same as Fig. 4.5, the E-field solution.

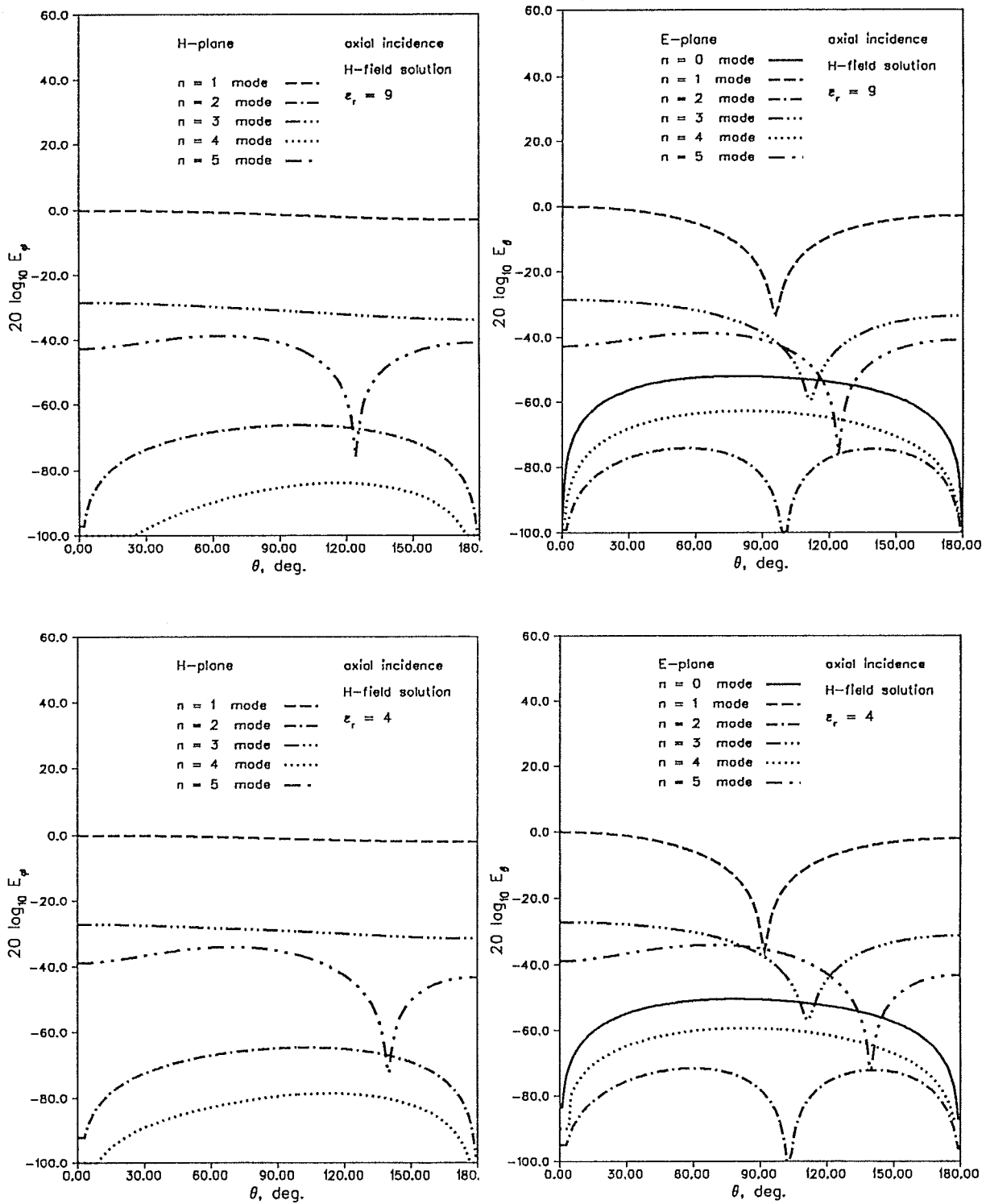


Fig. 4.7 : Same as Fig. 4.5, the H-field solution.

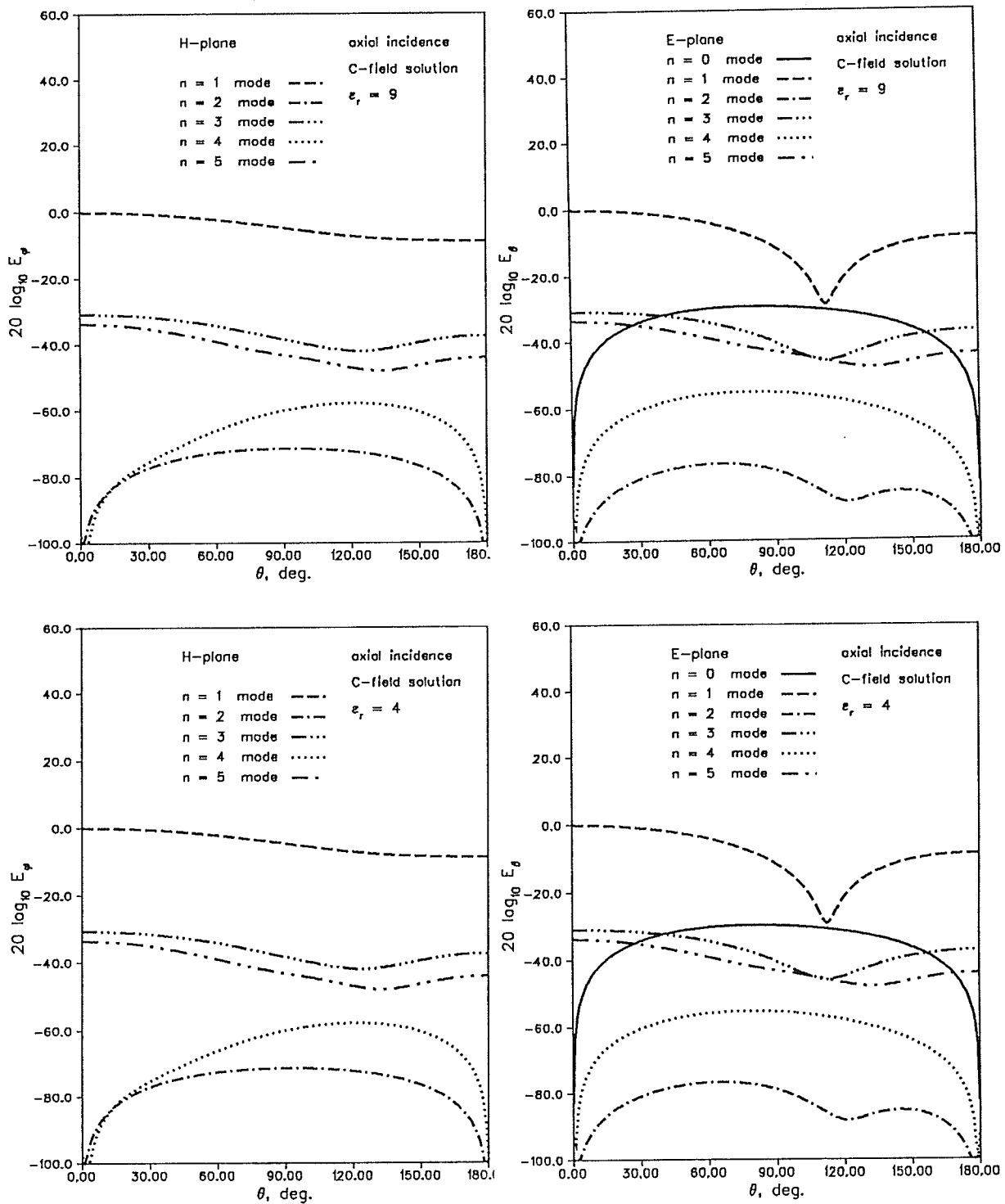


Fig. 4.8 : Same as Fig. 4.5, the C-field solution.

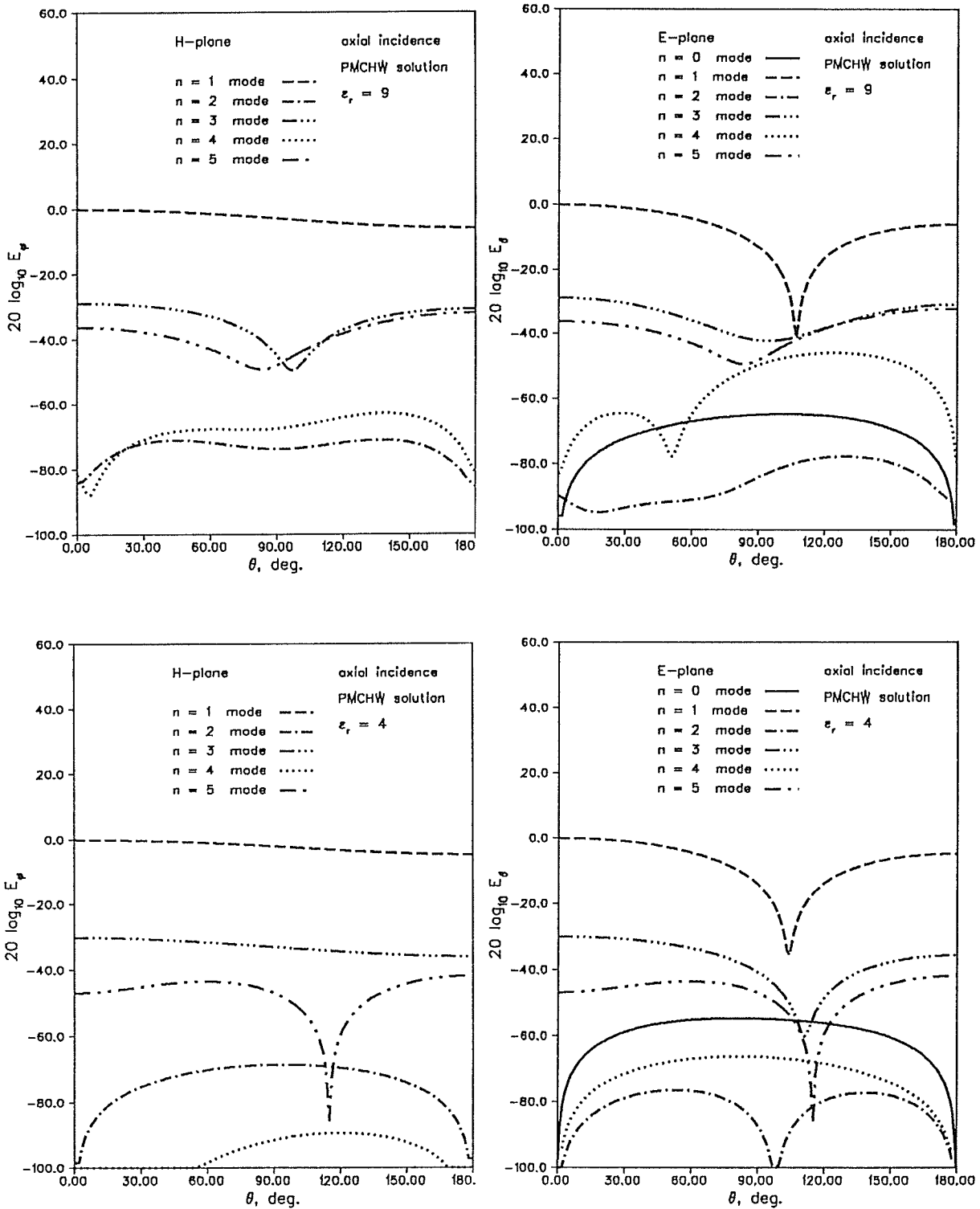


Fig. 4.9 : Same as Fig. 4.5, the PMCHW solution.

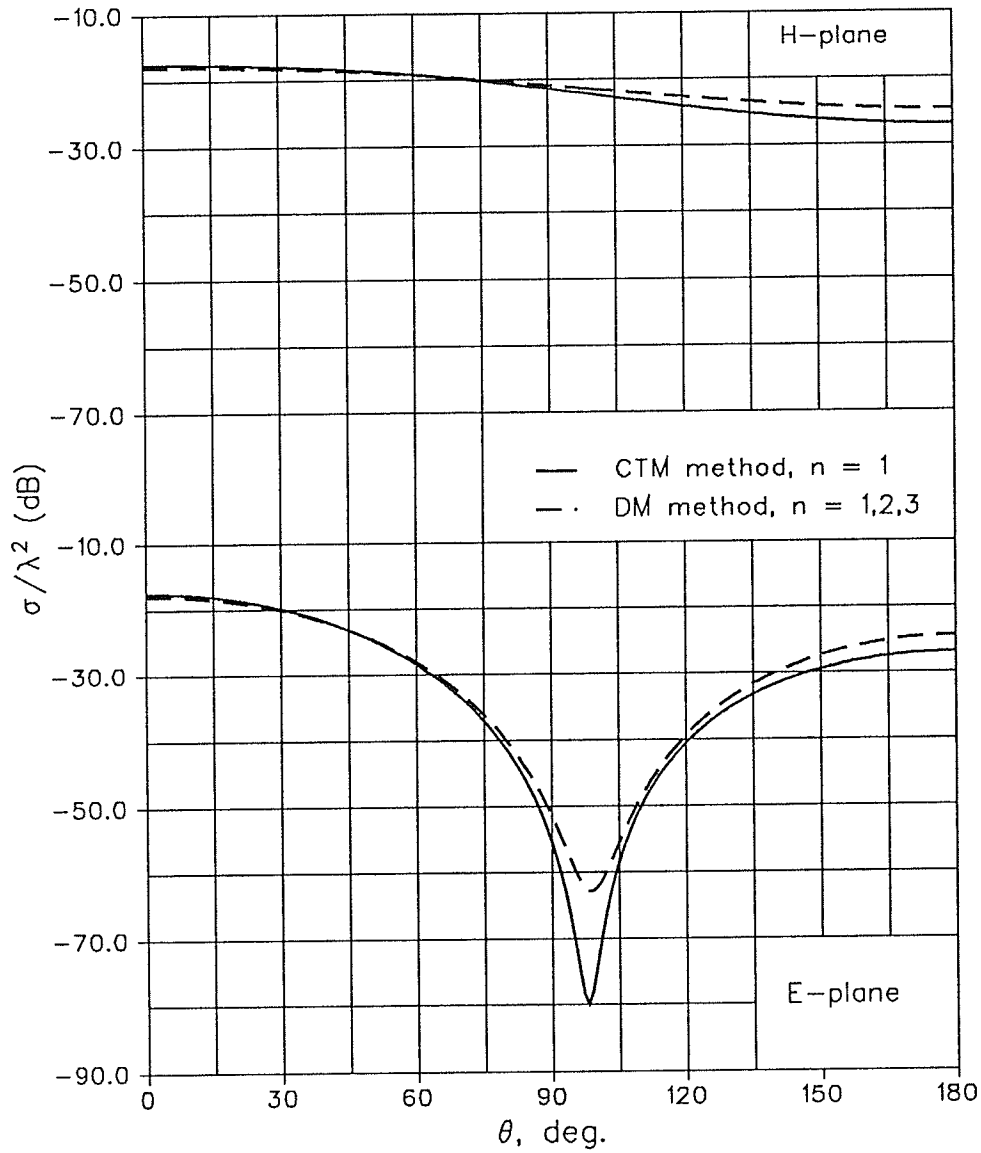


Fig. 4.10 : Bistatic scattering patterns of a dielectric cube of $L = 0.256\lambda$ and $\epsilon = 4$, for a normal incident plane wave.

Chapter 5

Radiation from rectangular waveguides

5.1. Introduction

Rectangular waveguides and horns are among of the most common types of aperture antennas and regularly used at microwave frequencies. Rectangular horns are more common in use and their flare angles control their patterns shape and assist in matching the wave impedance. Rectangular waveguides, with or without a small flare at the aperture, are also popular and used in variety of applications as simple antennas, diathermy and hyperthermia applicators, and radiating elements in space or plasma environment.

Although the geometry of a rectangular waveguide or horn is quite simple, generating an exact solution for their radiated field is not currently feasible. Approximate methods using an aperture integration, or the geometrical theory of diffraction are commonly used to determine their radiation. Examples of such methods are provided in [74] and [75]. In [74], the fields at the open end of a parallel-plate waveguide with an incident TE_{10} mode, is calculated. It is shown that, for plate spacings greater than 0.6λ , the incident and a singly diffracted fields are adequate for pattern calculations. In [75], the aperture field is expanded in a Fourier series, to study the coupling of two collinear coupled waveguides, radiating through the perfecting conducting plane. In this method, the problem is formulated as a set of simultaneous integral equations and solved approximately by expanding the aperture field in a Fourier series.

In recent years, other analytical and numerical techniques have been also studied, to investigate the radiation from rectangular waveguides terminated by an infinite flange. They are referred to as the variational [76]-[78], correlation matrix [79], and integral equation methods [80].

The variational principle is applied in [77] to the case of a flanged rectangular waveguide radiating into a half-space. In this analysis, the field in the waveguide is represented in terms of orthogonal TE and TM modes. By imposing the boundary conditions across the aperture, an integral equation is then obtained, which relates the transverse magnetic fields in the waveguide and in the half space regions to the unknown transverse electric field in the aperture. The aperture admittance of a rectangular waveguide is then computed.

The transverse operator method introduced by Marcuvitz [81] is used in [78] to analyze the radiation characteristics of open-ended rectangular waveguides terminated by a metal flange. In this method, the admittance and power patterns are determined by applying the continuity of the tangential fields, in the spectral domain, which leads to a simple relationship between the electric and magnetic fields. The aperture admittance and the radiation patterns are then determined by expanding the fields in a series of normal transverse electric (TE) and transverse magnetic (TM) modes. It has the advantage of simplicity of the analysis, and the ease of numerical computation. This is particularly true in the case of discontinuities, where the radiation is into a medium such as, a dielectric waveguide, or a shielded structures like a partially filled waveguide.

A more elaborate investigation of radiation from rectangular waveguides terminated by an infinite flange was carried out by Macphie and Zaghloul [79]. They treated the problem, using the principle of conservation of power, which lead to a nonvariational expression for the scattering matrix of a flanged termination. In this method the power radiated from the aperture is expressed in terms of correlation functions of the aperture electric field, which yields a Hermitian matrix for the radiated power in terms

of the electric mode amplitudes. The principle of conservation of power is utilized to obtain an expression for the scattered field, in which the effective TE_{10} load admittance is calculated from the resulting scattering matrix. This technique is rather involved in the formulation. However, it yields results with a high degree of accuracy.

The integral equation method in conjunction with the method of moments is used in [80] to solve numerically the electromagnetic transmission through an arbitrary aperture. The integral equation is formulated for the unknown equivalent magnetic current over the aperture region and evaluated using expansion and testing functions which are the product of triangles and pulses. The triangular basis functions are selected in the direction of current flow, and pulses are chosen in the transverse direction. The formulated integral equation is given for an arbitrary shape aperture. However, the numerical results are provided only for the rectangular shape apertures.

Available theoretical methods are based on some types of approximations, and can hardly be extended to study the effect of geometrical changes, for the improvement of the radiation characteristics. This restricts the validity of these approaches to their particular cases. In addition, valuable informations, such as the back scattering and cross polarization can not be obtained using some of these methods. Therefore, the objective here is to develop a more flexible numerical method, so that the radiation characteristics of rectangular waveguides can be investigated easily and in more detail.

In this chapter, the E-field integral equation is utilized to investigate the radiation patterns of the rectangular waveguide. The selection of the E-field equation was based on its applicability to both open and closed surfaces. It is also, more suitable for thin structures due to the operators affecting the Green's function. The conformal transformation method is formulated, and the accuracy of the method is investigated. The *DM* formulation takes a similar form as the *CTM* and omitted here for brevity. However, the complete formulation of the method can be found in [84]. The excitation is obtained from a dipole source with a proper location and polarization inside the guide, so

that the dominant or any desired propagation mode can be investigated. Subsequently, the behavior of the solution is studied, to determine the effect of various numerical and geometrical parameters, on the accuracy, and the convergence of the solution. Preliminary results for the rectangular waveguide characteristics are presented in the following section. The detail analysis of the problem is under further investigation. The formulation presented here is valid for metallic waveguides of any cross section. However, the generated results are given only for rectangular waveguides.

5.2. Formulation

The formulation of the problem is in terms of the Electric field integral equation (*EFIE*). The derivation of the equations governing the problem and also the necessary steps leading to the impedance operator formulation are given in chapters two or three, depending on the selected numerical approach (*CTM*, or *DM*). Here, similar to the scattering problems the current on the waveguide's surface is decomposed into two components along two orthogonal hybrid tangent vectors \hat{t} and \hat{s} , as shown in Fig. 5.1, and defined in equations (2.2). The expansion and evaluation of the surface current \mathbf{J} , and the reduction of the integral equation to a matrix equation follows the procedure of the moment method. However, to model the waveguide's surface, a closed generating curve is taken, which requires the modeling of the inner and outer surface. Such a surface modeling, increases the dimension of the moment matrix approximately by a factor of two.

The source of the excitation is generally due to an aperture on the waveguide's wall, or by a coaxial probe. Such excitations are difficult to handle numerically. On the other hand, if the waveguide dimensions are selected such that only the dominant mode can propagate, a simple dipole source can be used as the actual source of excita-

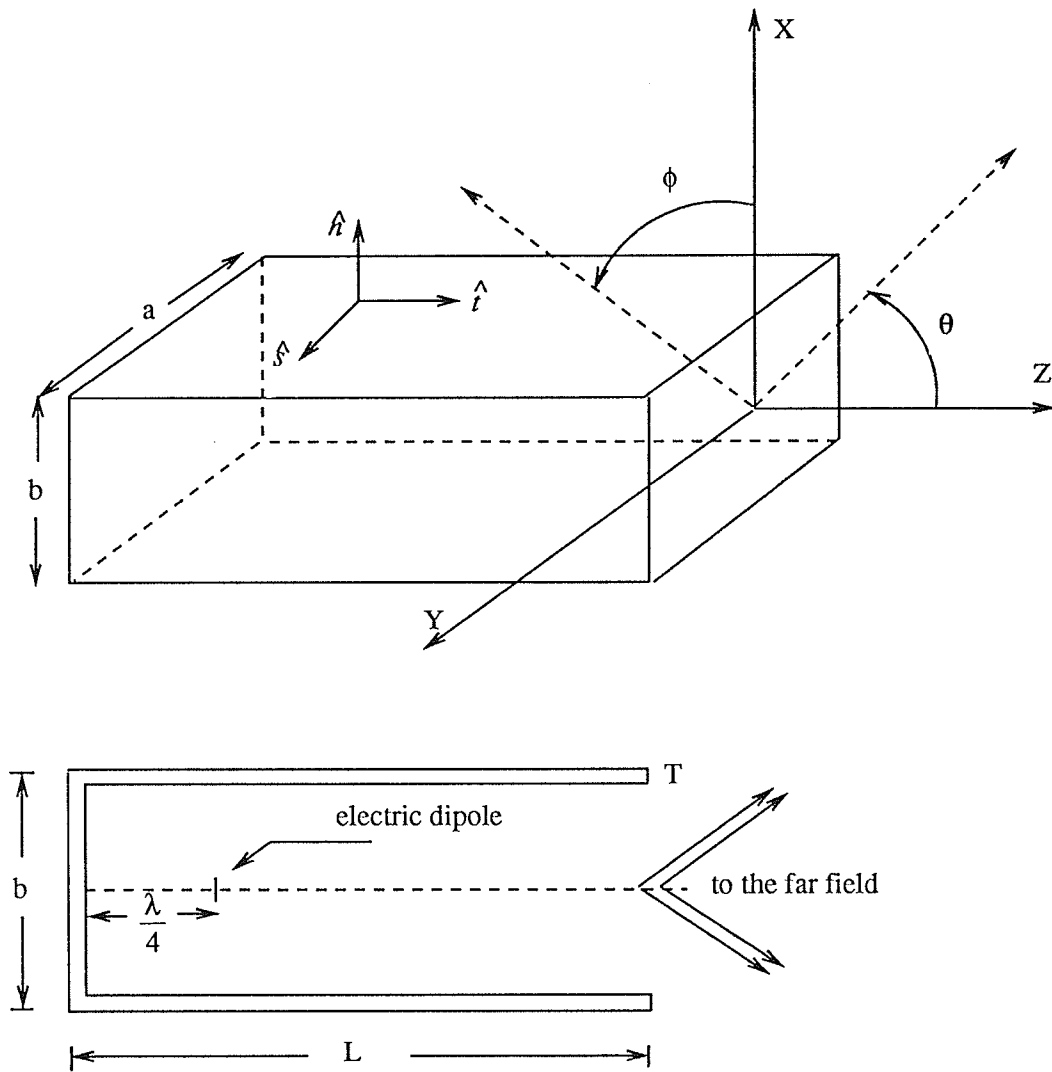


Fig. 5.1 : Physical and numerical modeling of a rectangular waveguide.

tion. It has been used successfully in the past, in studying the radiation patterns of corrugated circular horns by Iskander and Shafai [82], circular, and coaxial waveguides by Shafai and Kishk [83]. A similar source modeling is also adopted here. As a result, an x -directed electric dipole is located on the axis of symmetry at the point $(0, 0, Z_d)$, as shown in Fig. 5.1. Thus, the incident electric field may be written as,

$$\mathbf{E}^i = -j\omega\mathbf{A}_d - \nabla\Phi_d \quad (5.1.a)$$

where, \mathbf{A}_d and Φ_d are the vector and scalar potential given by,

$$\mathbf{A}_d = \frac{-jk\mu\mathbf{Id}l}{4\pi} h_0^2(kR) \quad (5.1.b)$$

$$\Phi_d = \frac{\eta}{4\pi} \mathbf{Id}l \cdot \nabla h_0^2(kR) \quad (5.1.c)$$

Here, $\mathbf{Id}l$ is the dipole moment, η is the intrinsic impedance of the medium, μ is the permeability of the medium, k is a wave number, R is the distance between the source point and a field point, and $h_0^2(kR)$ is the spherical Hankel function of the second kind defined as,

$$h_0^2(kR) = \frac{e^{-jkR}}{kR} \quad (5.2)$$

Following the procedure of the moment method, the excitation vector (V_{mi}^p) can be transformed into an integral of the form,

$$(V_{mi}^t) = \frac{-j\eta k |\mathbf{Id}l|}{4\pi} \int_0^t dt \, cf_i(t) [\sin \beta_i G_7 + j \frac{\partial}{\partial t} (cf_i(t)) G_8] \quad (5.3.a)$$

$$(V_{mi}^s) = \frac{j\eta k |\mathbf{Id}l|}{4\pi} \int_0^t dt \, cf_i(t) [G_9 + \frac{jm}{c_i} cf_i(t) G_{10}] \quad (5.3.b)$$

where,

$$G_9 = \int_0^{2\pi} f(R, \xi) \cos \phi(\xi) d\xi \quad (5.4.a)$$

$$G_{10} = \int_0^{2\pi} f(R, \xi) \frac{1 + jkR}{kR} \frac{x}{R} d\xi \quad (5.4.b)$$

$$G_{11} = \int_0^{2\pi} f(R, \xi) \sin \alpha(\xi) d\xi \quad (5.4.c)$$

$$G_{12} = \int_0^{2\pi} L(\xi) \frac{1 + jkR}{kR} \frac{x}{R} d\xi \quad (5.4.d)$$

with

$$f(R, \xi) = h(\xi) \frac{e^{-jkR}}{kR} e^{-jm\xi} \quad (5.5.a)$$

$$L(\xi) = \frac{1}{h(\xi)} [\sin^2 \alpha x'_\xi + \cos^2 \alpha y'_\xi] \quad (5.5.b)$$

$$R = [\rho(\xi)^2 + (z - z_d)^2]^{\frac{1}{2}} \quad (5.5.c)$$

Using an approach similar to approximating the triangular basis functions by $2M$ pulses, the i^{th} element of the excitation vectors can be written as,

$$V_{mi}^t = \frac{-j\eta k |Idl|}{4\pi} \sum_{p=1}^{2M} [T_p' \sin \beta_i G_9 + T_p' G_{10}] \quad (5.6.a)$$

$$V_{mi}^s = \frac{j\eta k |Idl|}{4\pi} \sum_{p=1}^{2M} [T_p' G_{11} + \frac{jm}{kc_i} G_{12}] \quad (5.6.b)$$

The current coefficients can be subsequently obtained, by solving a system of linear equations of the form,

$$\sum_{n=-\infty}^{\infty} \sum_{j=1, N} (Z_{mn}^{pq})_{ij} a_{nj}^p = V_{mi}^p \quad m = 0, \pm 1, \pm 2, \dots \quad (5.7)$$

where, Z_{mn}^{pq} is the impedance operator as defined in previous chapters, n, m are the Fourier modes, and a_{nj}^p are current coefficients to be determined. Once the current coefficients are calculated, the radiation pattern of the waveguide in both E- and H-

planes can be determined by evaluating the total field, which is the sum of the incident field of the dipole located inside the waveguide, and the scattered field due to the induced surface currents. The required scattering matrices are those developed in chapters two or three, and omitted here for brevity. The formulation leading to the field of a dipole radiating in free space is, however, summarized in appendix III. The radiation in the E- and H-planes can be subsequently determined, by selecting the proper plane cuts, such as $\phi = 0^\circ$, and $\phi = 90^\circ$, respectively.

5.3. Numerical results

To investigate the radiation patterns of rectangular waveguides, an optimum model which numerically represents the actual physical model is required. Therefore, certain numerical aspects of the modeling, such as a proper selection of subdomain basis functions, the convergence of Fourier modes, and their coupling were studied. A study was also done to investigate the effects of the waveguide's physical parameters, on the radiation patterns, in particular, the effects of wall thickness, and the waveguide length. The latter is required, to insure the attenuation of higher order modes at the aperture, which results in launching of only the TE_{10} mode. Although, both inner and outer surfaces of the waveguide were included in the analysis, it was found that it is better to model the surface current on the waveguide inner wall more accurately, due to the presence of strong fields inside the waveguide. Utilizing this approach, numerical solutions were obtained by selecting more current sampling points along the inner sections of the generating curve of the waveguide. This type of modeling results in a better sampling of the fields inside the guide, and subsequently, gives more accurate results.

The effect of linear basis functions number was investigated for the operating frequency near the cut off of the dominant, TE_{10} mode. The density of the matching points was changed from $NP = 39$ to 49 and 59 points, and the computed results for a frequency of $f = 1.1 f_c$ are shown in Fig 5.2. For this case, a single $n = 1$ Fourier mode in the cross-section was assumed and the numerical results converged when the number of linear basis functions in the t -direction was increased to 23 resulting in matrices of order 46×46 . Increasing beyond this point, i.e., $NP = 59$, did not appreciably affect the radiation patterns. Also, lower densities of matching points would generally result in a slightly narrower beam widths in both planes and lower back radiations. This study indicated that a selection of about 10 segments per wavelength constitutes an optimum choice.

Next, the effect of waveguide's length on the radiation patterns was investigated. With the selected dipole source, it's length should be long enough to attenuate the higher order waveguide modes at the aperture. However, increasing the waveguide length excessively increases both the required computer memory and time. While, the radiation patterns are influenced by the waveguide's length, particularly in the back direction, its sufficient length insures the illumination of the aperture by the dominant TE_{10} mode. Therefore, waveguides of different lengths were investigated, and the computed results, for the single $n = 1$ Fourier mode, are shown in Fig. 5.3. It is evident that, for the selected frequency, increasing L tends to enhance diffraction lobes, specially in the H-plane. The back lobe level, on the other hand, oscillates with the waveguide length, reducing initially by increasing L and increasing again for $L > 1.75 \lambda$.

Figs 5.4 shows the contribution of higher order surface current modes to the radiated field, and their effects on the beam widths for different operating frequencies. It was found that, the degree of coupling increases for higher frequencies. The higher order odd modes, i.e., $n = 2,3$, are more dominant and they incorporate the edge

diffraction, specially in the E-plane where, their effects are significant around 90 degree. Consequently, one requires to include these modes to insure a proper modeling of the edge diffracted field, which results in a higher precision for the solution. These computations show that, for the symmetric excitation, the even modes, i.e., $n = 2, 4$, do not participate in the computation of the scattered field, and in all the cases presented here, they are at least 30 dB below the dominant $n = 1$ mode.

The effect of wall thickness on the radiation patterns was investigated by selecting different thicknesses of $T = 0.015, 0.03, 0.045, 0.06$, and 0.075λ . The computed patterns for a waveguide length of 1.5λ , and a frequency of $f = 1.37f_c$ are shown in Fig. 5.5. Increasing the waveguide thickness has a direct effect on the E-plane pattern and broadens the main beam. However, the H-plane pattern stays relatively constant. The back-lobe level increases slightly in H-plane, approximately by 1.0dB. For an operating frequency range of, 9.0–12.0GHz, the physical thickness of a commercial waveguide is about 0.04λ . Hence, a similar thickness of $T = 0.04 \lambda$ was chosen as an optimum choice for the rest of computations. However, the formulation is capable of handling any thickness, excluding the limiting case of a zero thickness.

From the above study it was concluded that an average number of 10 pulses per wavelength, and a selection of at least three modes, i.e. $n = 1, 2, 3$ would constitute an optimum choice. This will result in a convergent solution with a minimum computational time. Discrepancies are more likely to appear in the back lobe region, where the actual results are presumably lower. In order to check the validity of the formulation, the radiation patterns of a rectangular waveguide of dimensions, $a = 0.686 \lambda$, $b = 0.305 \lambda$, $L = 1.5 \lambda$, and thickness of $T = 0.04 \lambda$ were obtained and the computed results are shown in Fig 5.6. A measurement was conducted at several frequencies using an RG52U rectangular waveguide (x-band) with a physical length of $L = 10.67 \text{ cm}$ from the feed location, and a cross section of $a = 2.286 \text{ cm}$, $b = 1.016 \text{ cm}$. A waveguide coaxial adapter was used as a source of excitation. The computed patterns

shown in Fig. 5.6 agree with the measured data for the most of the angular range. In the back direction the computed radiation patterns are higher. Their differences are primarily due to the actual difference of the model used in computation and that of the experimental unit. For the recommended waveguide's operating frequency, i.e., 9.0-12.0GHz, the $n = 1$ mode is the dominant mode, and together with the radiation of the dipole field contributes most of the radiation. Introduction of the $n = 2,3$ modes reduces the back radiation by about 3 dB. A further increase in the number of modes showed no significant effect on the H-plane pattern. However, the convergence is usually slower in the E-plane and higher order modes were needed to obtain an acceptable accuracy.

Next, the cross-polar field radiated from the waveguide was computed by utilizing Ludwig's third definition [85]. From the definition of the cross polarization and also a consideration of the symmetric excitation, it can be deduced that the peak values of the cross-polar field will occur in the diagonal planes of the far-field radiation pattern.

Fig. 5.7 shows the values of these peak cross-polarization for waveguide of square cross-section and for various aperture dimensions. For the sake of comparison, the numerical results of [86] are also included. The agreement is satisfactory. For a square waveguide, the peak cross-polar field is directly proportional to the size of the aperture. For aperture sizes of $a < 1.0\lambda$ the cross-polar field increases rapidly, and levels off for dimensions $a > 1.2\lambda$. For the selected square waveguide, and aperture dimension of, $a < 1.0\lambda$ the cross-polarized field increases and maximizes at $\theta = 90^\circ$ (Fig. 5.7.b). However, the cross-polar pattern is quite different for a rectangular waveguide, where the cross-polarized field maximizes around $\theta = 60^\circ$, and reduces considerably around 90° (Fig. 5.7.c).

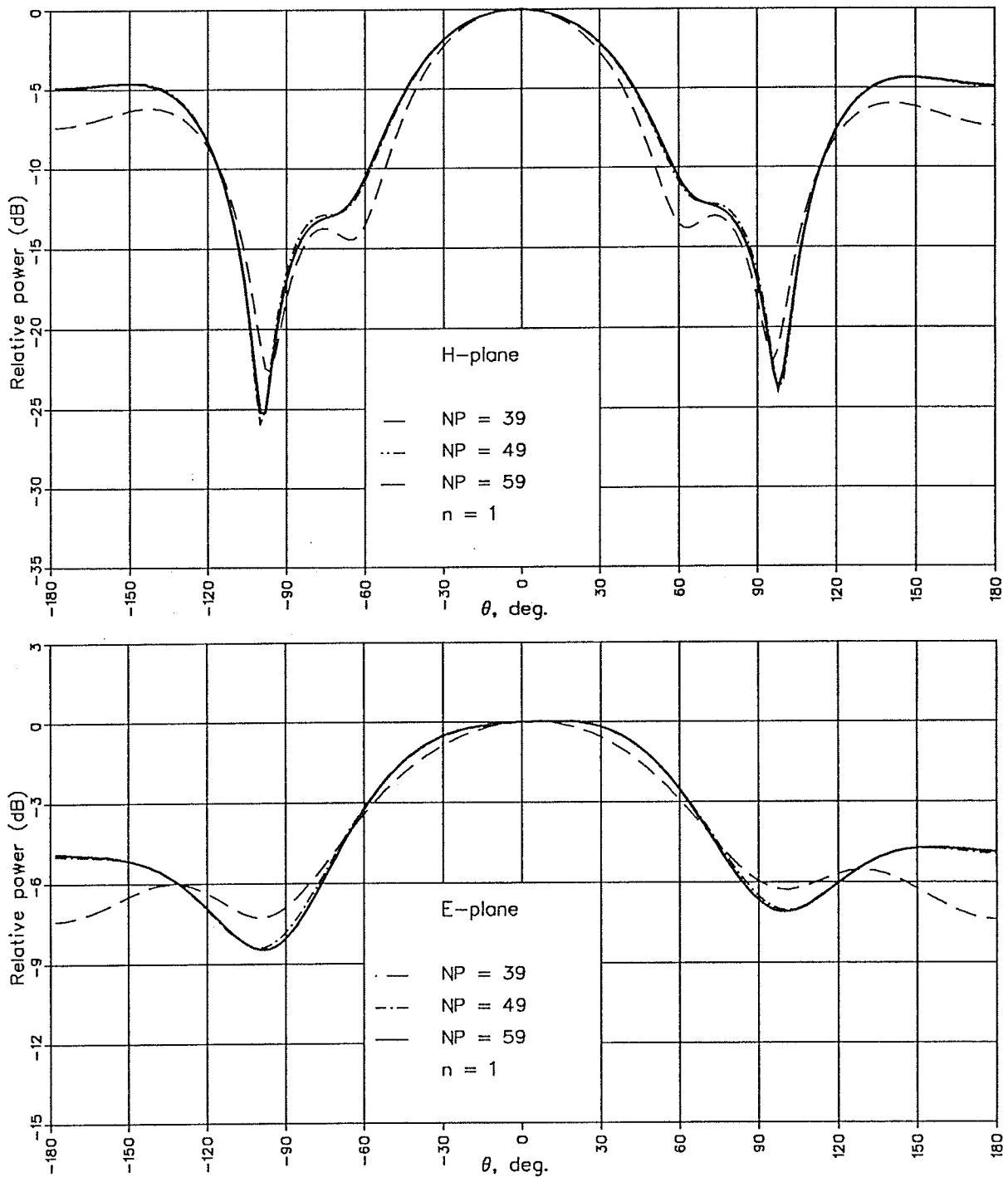


Fig. 5.2. : Radiation patterns of a rectangular waveguide, $a = 0.5\lambda$, $b = 0.22\lambda$, $L = 1.5\lambda$, and $f = 1.1 f_c$.

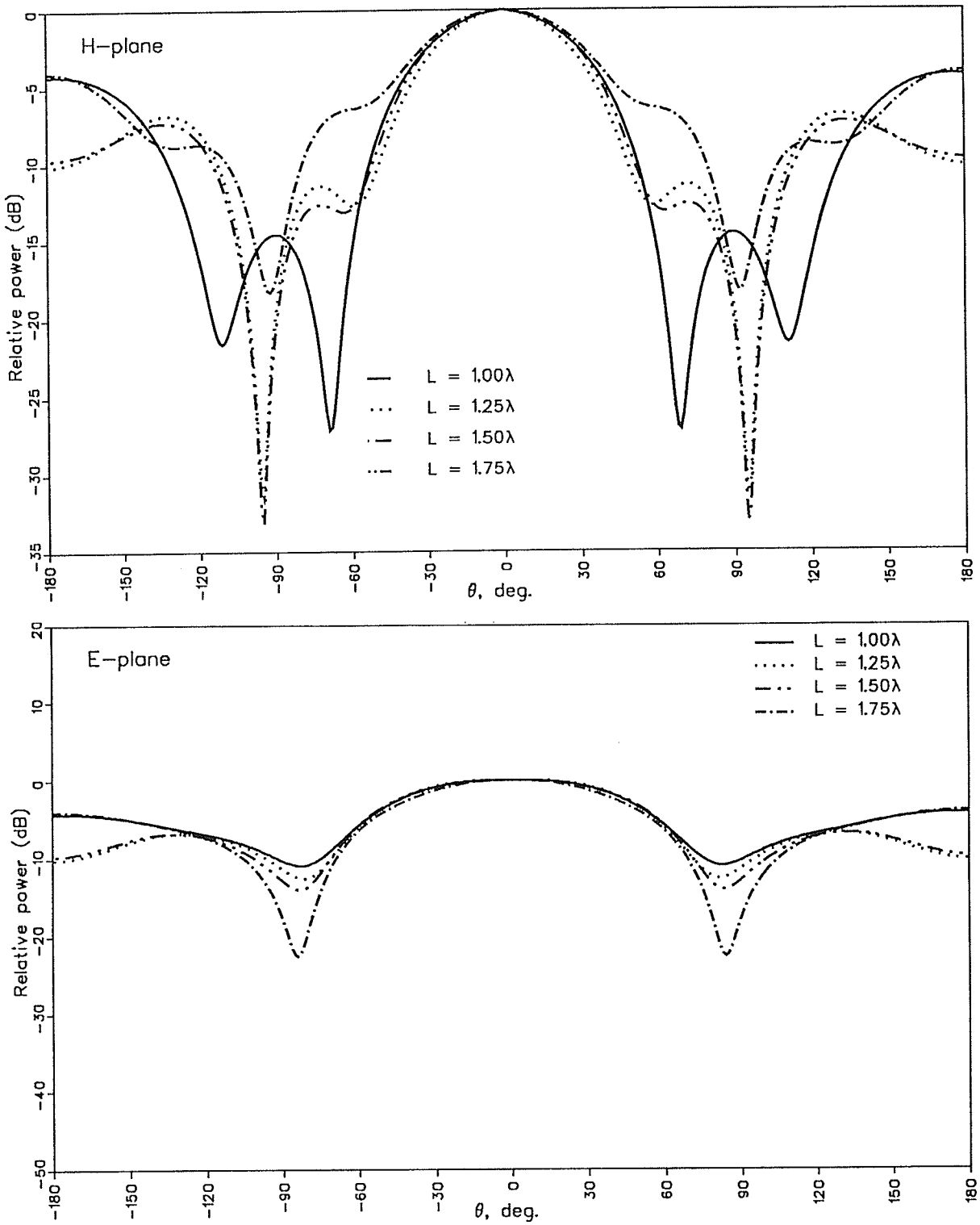


Fig. 5.3. : Effect of the waveguide length on the radiation patterns, $a = 0.686\lambda$, $b = 0.305\lambda$, $n = 1$ mode, and $f = 1.37f_c$.

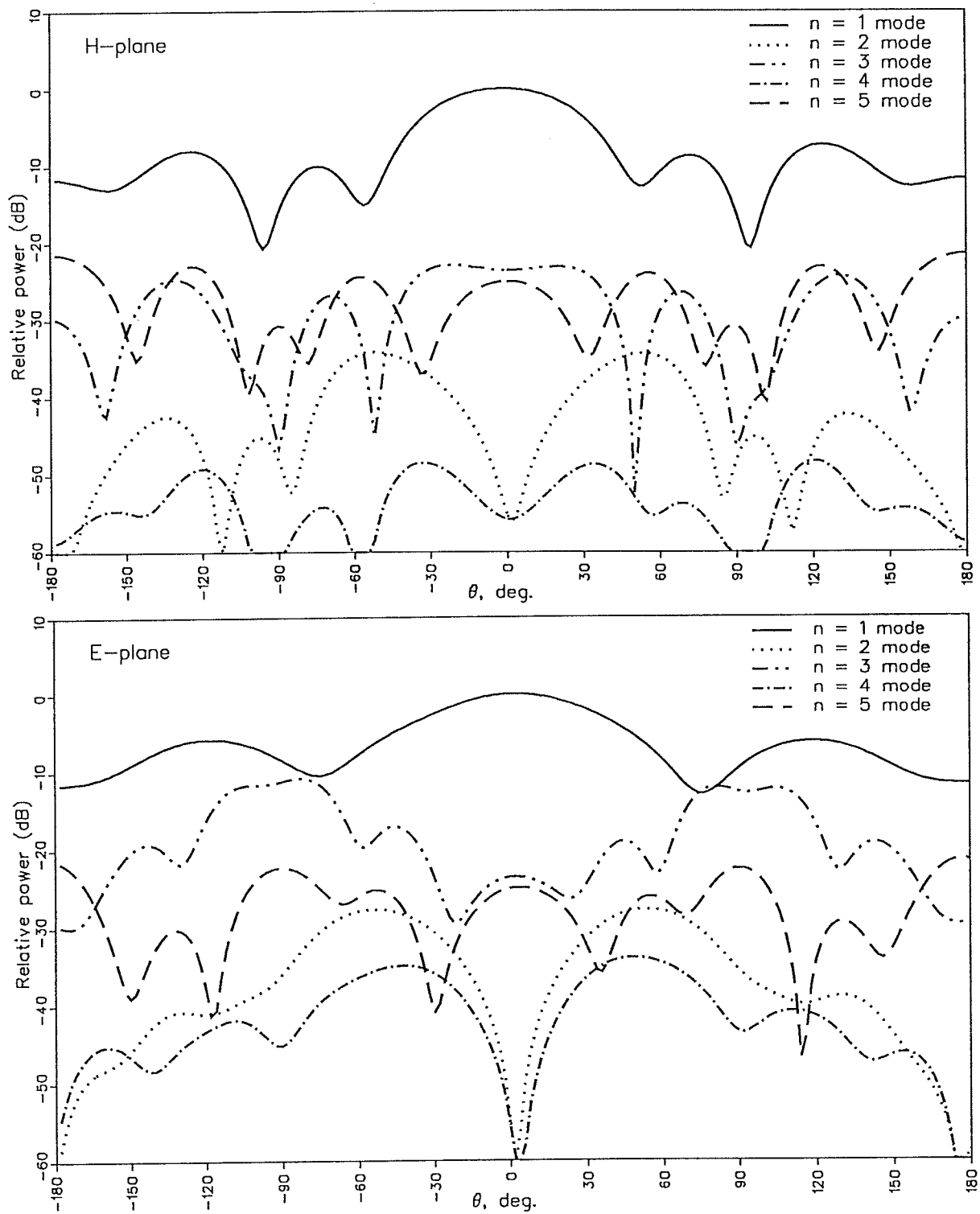


Fig. 5.4.a : Contribution of higher order modes to the radiation patterns of a rectangular waveguide, $a = 0.686\lambda$, $b = 0.305\lambda$, $L = 1.5\lambda$, and $f = 1.37f_c$.

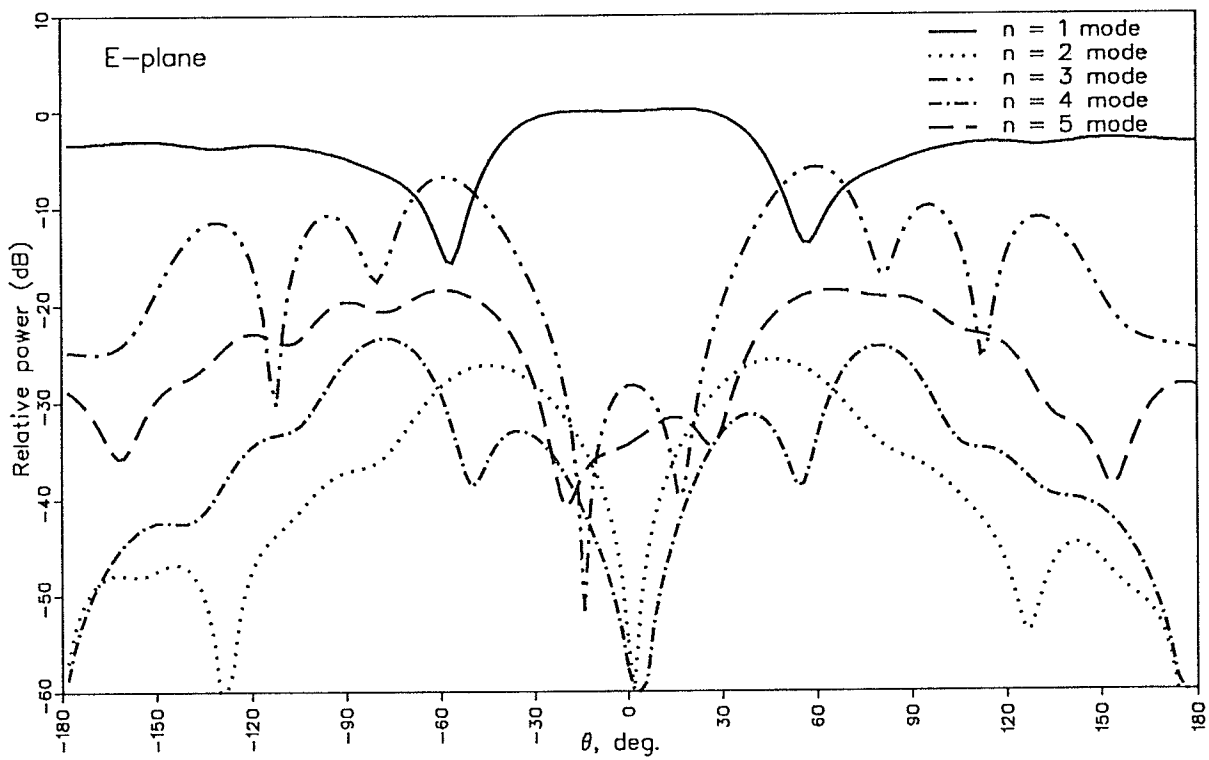
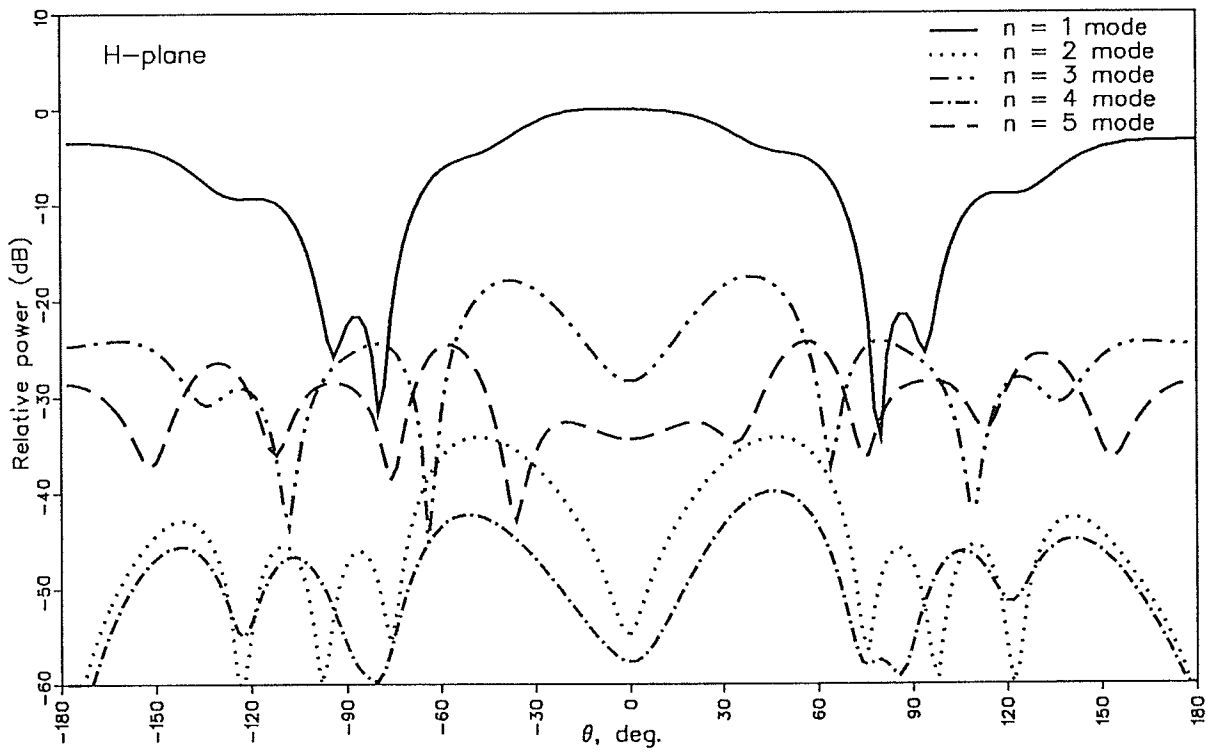


Fig. 5.4.b : Same as Fig. 5.4.a except $f = 1.82f_c$.

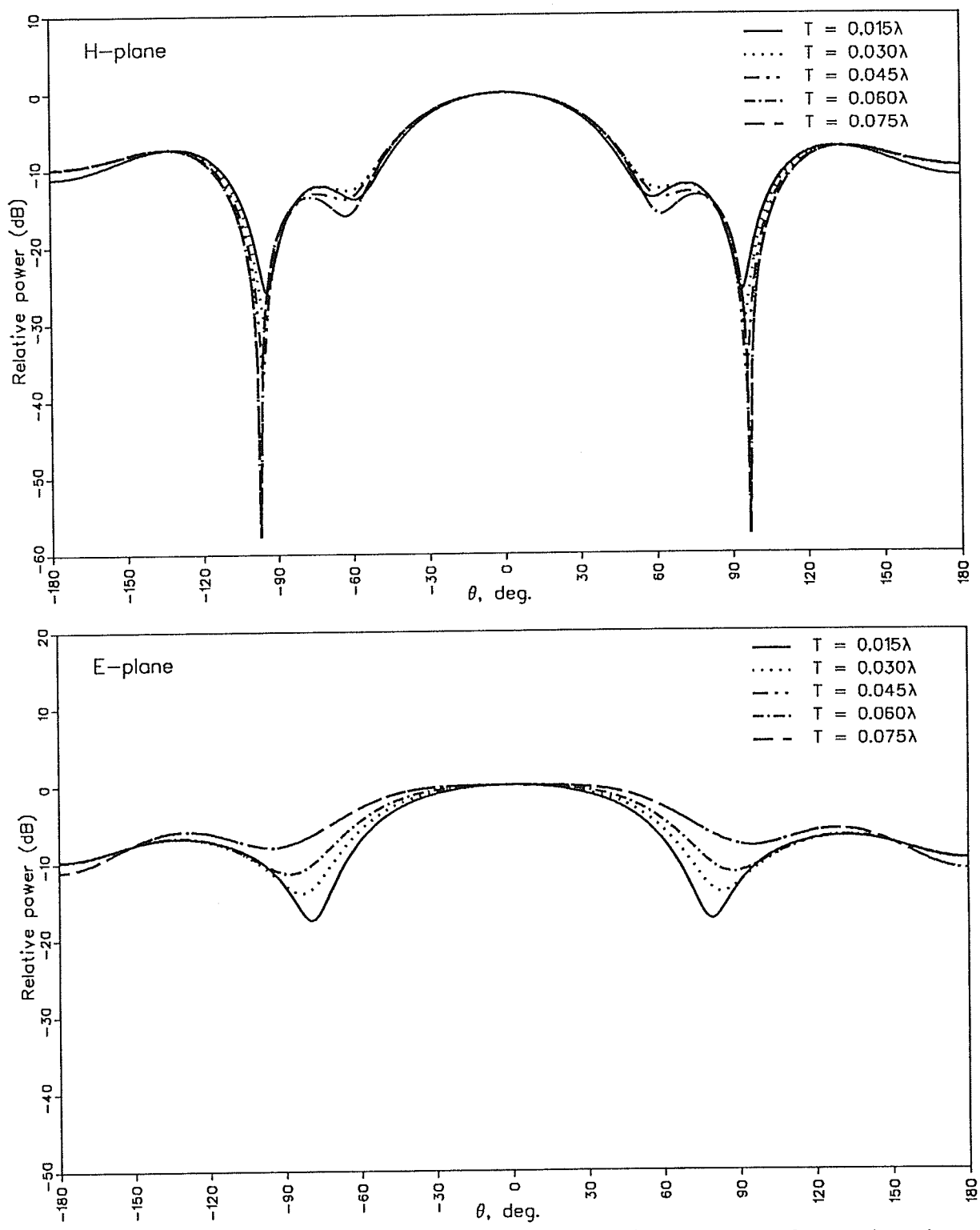


Fig. 5.5. : Effect of the wall thickness on the radiation patterns of a rectangular waveguide, $a = 0.686\lambda$, $b = 0.305\lambda$, $L = 1.5\lambda$, $n = 1$ mode, and $f = 1.37f_c$.

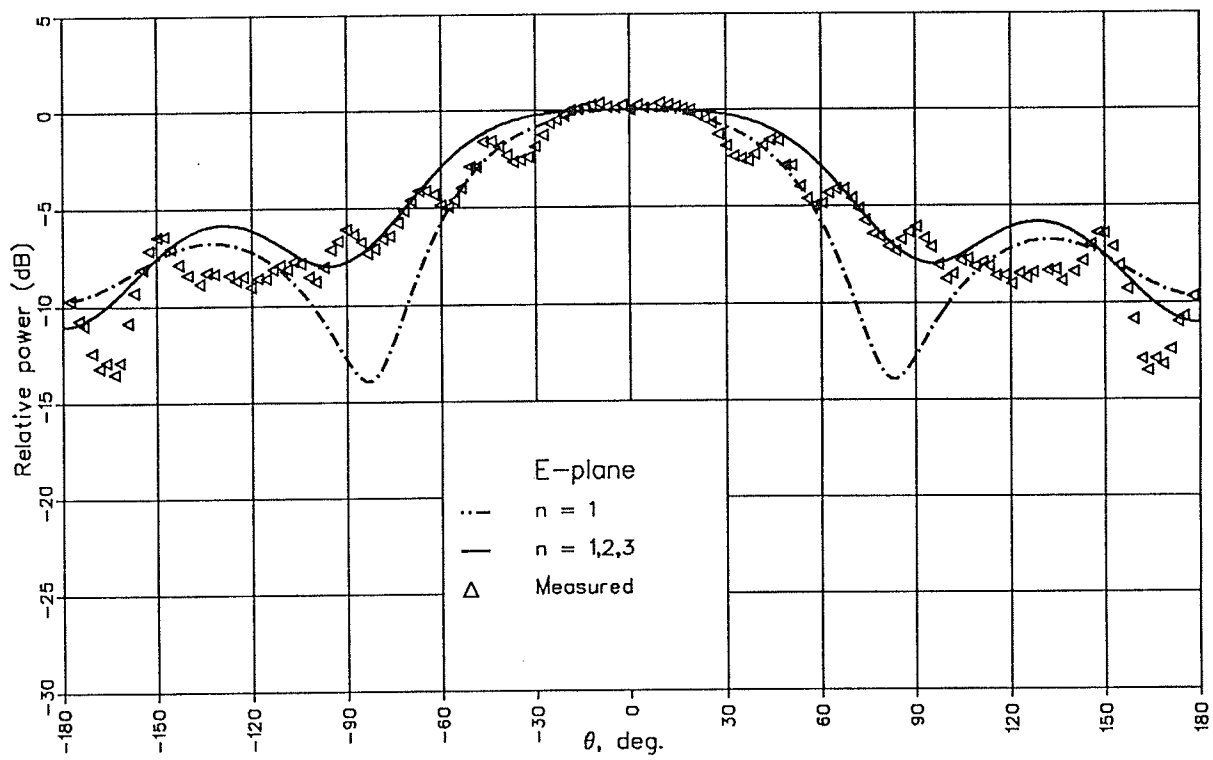
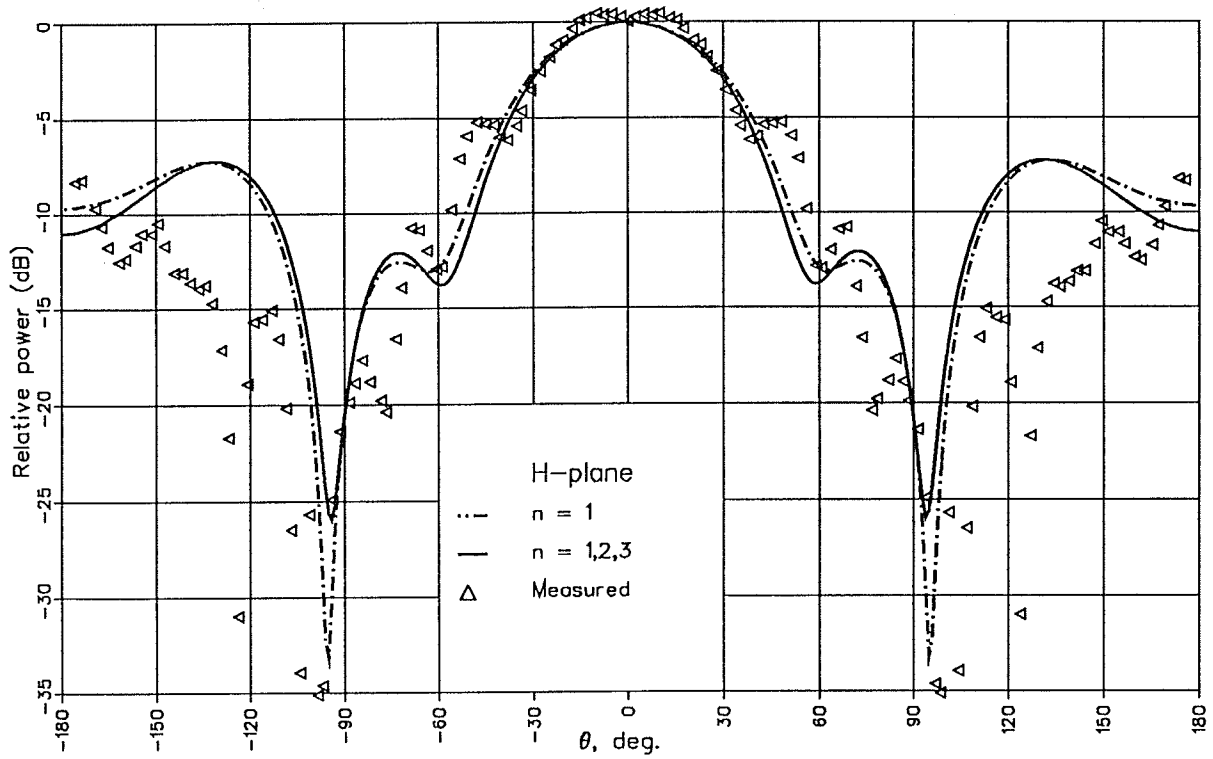


Fig. 5.6. : Radiation patterns of a rectangular waveguide, $a = 0.686\lambda$, $b = 0.305\lambda$, $L = 1.5\lambda$, and $f = 1.37f_c$.

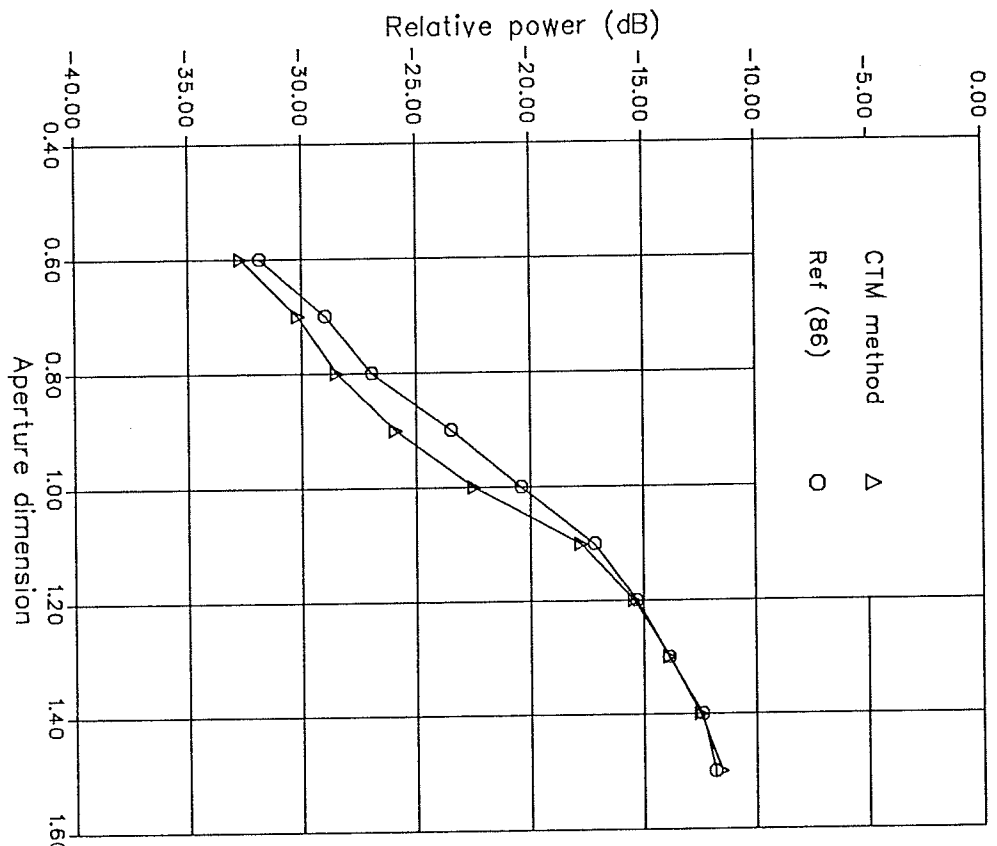


Fig. 5.7.a : Cross-polar characteristic of a square waveguide.

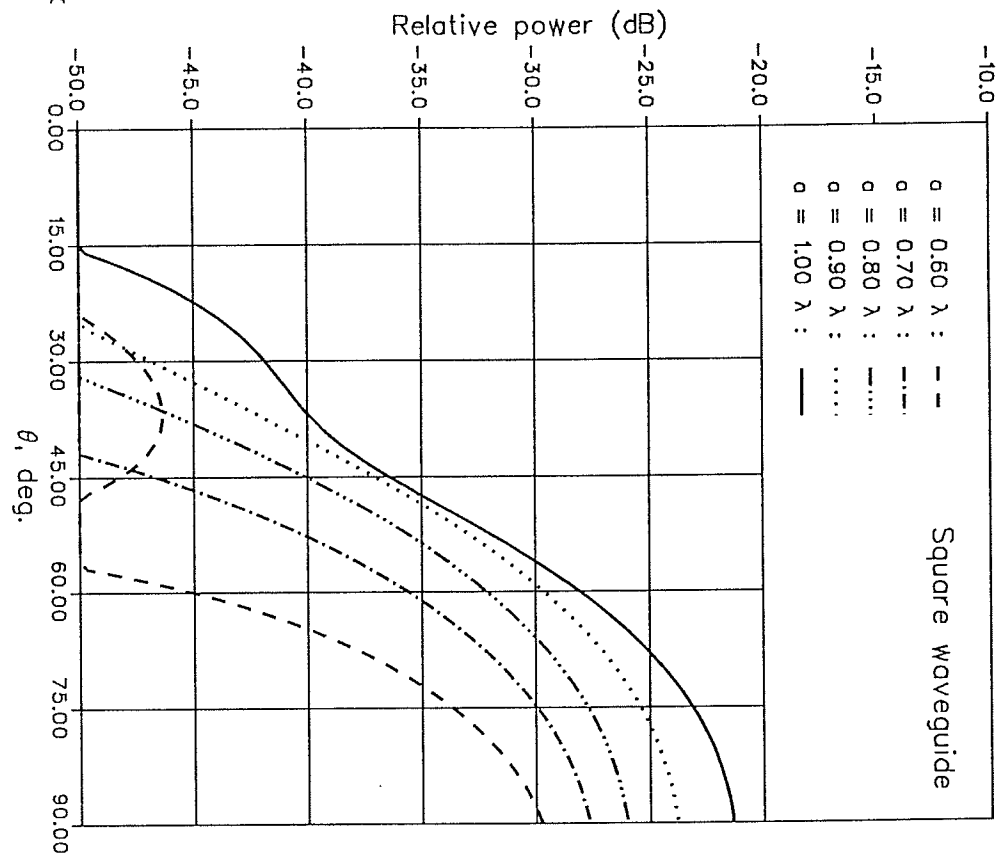


Fig. 5.7.b : Cross-polar radiation pattern of a rectangular waveguide of $L = 1.2 \lambda$ and $n = 1$.

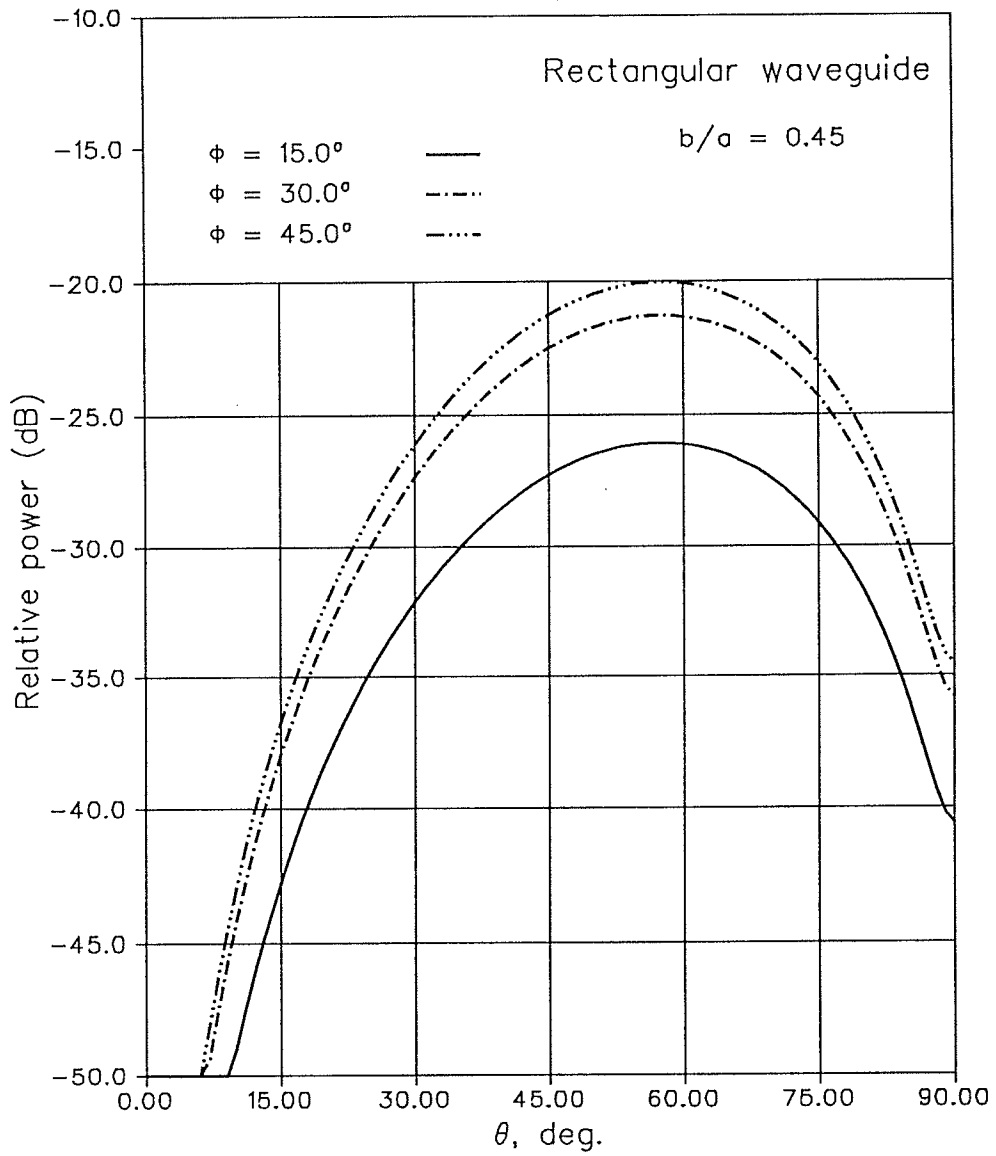


Fig. 5.7.c : Cross-polar radiation pattern of a rectangular waveguide of $a = 0.686\lambda$, $b = 0.305\lambda$, $L = 1.5\lambda$, $n = 1$, and $f = 1.37f_c$.

5.4. Conclusions

The radiation characteristics of a rectangular waveguide antenna were studied numerically using the E -field integral equation and the techniques presented in the previous chapter. The current on the waveguide's surface was modeled by hybrid basis functions, and moment methods were used to convert the integral equation to a matrix equation. The total electromagnetic field radiated from the waveguide was determined from the sum of the scattered field due to surface current and that of the dipole source. The effect of several numerical and physical parameters on the radiation patterns were investigated. It was found that, higher order modes are present, and incorporate the edge diffracted field. For the selected waveguide dimensions, three Fourier modes were sufficient to describe adequately the \hat{s} -dependence of the surface current. As the operating frequency increased, more number of triangular functions were needed to model the current along the \hat{t} -direction. However, for waveguides of larger dimensions the size of the moment matrix increases rapidly, and round-off errors dominate. A rapidly growing matrix dimension, leads to an ill-conditioning of the matrix. But, for such problems, one can select smaller number of triangles, especially on the outer surface, and model them by more pulses. Such a technique has the advantage of keeping the matrix size small. It only increases the computer run time. The numerical results were compared with the experimental data measured in the laboratory, to validate the formulation. Satisfactory agreements were obtained in both planes. The formulation presented here, can be applied to waveguides of any length or thicknesses. This is due to the fact that, no assumption was made regarding the length or the thickness of the walls. However, as discussed earlier, for longer waveguides, a more accurate modeling of the surface current would be required.

Chapter 6

Discussion, Conclusions and Recommendations

6.1. Discussion and conclusions

The principal aim of the present work was to develop a new numerical technique to study the scattering from three dimensional conducting and dielectric geometries. Available numerical methods based on integral equation formulations and moment methods utilize simplified surface representations, such as surface patch and wire-grid modelings. Mathematically, they are equivalent to approximating the surface currents in terms of discrete basis functions of pulse or linear types. While, they are simple to use they suffer from limitations in the accuracy. In the present work, hybrid type basis functions were used by expanding the currents in terms of both discrete and entire domain basis functions, respectively along two orthogonal surface vectors. The entire domain basis functions were of the Fourier type and the convergence of their series was used to control the solution accuracy.

A major difficulty in using moment method solutions is estimating the accuracy. Computational errors accumulate from various sources, but the following ones contribute most

- a. Floating point arithmetic in computers that result in roundoff and truncation errors.
- b. Surface modelings of the geometry, which often modifies the object's shape.
- c. Approximate representation of subdomain basis functions such as multiple pulse representation for triangles.

d. Convergence of series for entire domain basis functions.

Errors due to the floating point variables can be reduced by selecting a double precision arithmetic. This, however, increases both computer storage and the execution time, and may not be desirable in some occasions, in particular, in using the moment methods. For this reason all computations of this thesis are carried out in single precisions.

Accurate modeling of the object's surface, of course, is essential for an accurate solution. However, deviations for the given objects results, the extent and form of which depend on the selected model. Such deviations alter the shape and consequently the results. Some of the secondary results, such as, the scattering pattern shape remain relatively insensitive to most minor geometrical deviations. However, others, specially those dependent on the near field distributions, alter significantly. Examples are, the resonance frequencies of the cavities, impedance of antennas and internal resonance of solid scatterers. Effects on dielectric objects can be more significant, due to variations in the permittivity, between the interior and exterior media. The other important aspect of accurate problem modeling is the accuracy of the number of pulses used to represent sub-domain triangle basis functions. A representation of triangles with a finite number of pulses is used to simplify the integrations involved. However, this means that the accuracy of the results for numerical integrations will depend on the number of pulses. In practice, for a given configuration, an optimum number of pulses exists. Selecting a smaller number for a pulse representation reduces the accuracy, which was noticed for dielectric media. On the other hand, selecting too many pulses increases roundoff errors. For the type of contour segmentations used in this study, four pulses found adequate to provide satisfactory results and their number for dielectric media was increased by a factor of $\sqrt{\epsilon_r}$, to compensate for the relative increase in segment size within the dielectric.

The final point of discussion on the error criteria is the convergence of the series for the entire domain basis functions. For rotationally symmetric scatterers, such as spheres and cylinders, the number of needed Fourier modes for a required degree of accuracy depends on the object size and the direction of the incident field. This issue is well studied in the literature. For complex geometries, such as those studied here, the selected Fourier type basis functions are not natural to the object and therefore couple on the object's surface. This means, the convergence of the series also depends on the geometrical shape of the scatterer. In practice, one hopes to use a minimum number of modes to reduce the needed storage and computation time. In current study the number of selected modes controls the matrix size. Thus, increasing the number of modes increases the matrix size and, in addition to increased cost, it also increases the roundoff errors. With a series type representation, one can examine the excitation efficiency of various modes to limit their number to the required degree of accuracy.

In summary, it may be said that the numerical method developed here is a fairly accurate and powerful approach for the analysis of three dimensional conducting and dielectric problems, including the amongst, the analysis of arbitrary cross-section objects. In the remainder of this chapter a brief overview of the technique is presented, and finally the last section of this chapter is devoted to the future work and to the improvement of the Direct Method.

In chapter 2, the method of coordinate transformation was described and solved by means of the moment methods. In obtaining the solution, the E- and H-field integral equations were used to develop a formulation for the numerical solution of scattering by conducting objects of arbitrary cross-section. A moment method was then used to generate matrix equations for determining the surface currents. To develop these matrix equations, two hybrid orthogonal tangent vectors \hat{t} , \hat{s} were defined on the object's surface. Along the \hat{t} , subdomain basis functions were selected, and in the plane containing the \hat{s} vector the cylindrical basis functions were selected and related to the

physical coordinates of the objects via a mapping function and the metric coefficient of the transformation. The resulting matrix equations were then a generalized form of that used for bodies of revolution, in which current modes were coupled. This method (*CTM*) was then applied to the scattering by conducting objects such as, plates and prisms. The effect of mode coupling and the strength of individual modes were investigated, for different angles of incidence and also, for different aspect ratios of the geometry. It was found that the mode coupling was generally present and converged rapidly. For the selected configurations, with a normal incident wave, normally three coupled modes were adequate to provide acceptable results. However, the selected basis functions were geometry dependent, and the convergence of the solution was related to the object's cross-section. The extreme deviation of the cross-section from circle by virtue of its aspect ratio, slowed down the solution convergence. Also, the *CTM* method required the computation of new metric coefficients as the cross-section aspect ratio changed.

In chapter 3, the Direct Method was described as it enabled the solution for the problem of scattering of arbitrary shape objects to be solved in the object's coordinates system. The E- and H-field integral equations were formulated and subsequently applied to geometries such as, conducting plates and prisms. Similar to the *CTM* technique, a generating curve was defined, and along that, the current was modeled by sub-domain basis functions. The second contour was defined orthogonal to the first one, over which the entire domain Fourier were used. A moment method was then used to convert the integral equations to a matrix equation. A study of the mode convergence showed the existence of mode coupling, due to the angle of incidence, and also the size of the scatterer and the object's aspect ratio. This method was found to be inefficient, for geometries of side length larger than a wavelength. Also, for objects with a sharp edge, the Fourier modes were inadequate to incorporate the singularity of the current at the edge, which increased the size of the moment matrix and resulted in

an inefficient method. Thus, to overcome this problem, an analytic expression should be included in the current expansions to possibly accelerate the convergence of the solution. In the next section, some aspects of such expansions are briefly presented.

In chapter 4, the formulations for conducting objects were extended to dielectric objects. The surface integral equation were formulated by Schelkunoff's equivalence principle in terms of equivalent surface electric and magnetic currents. Five different formulations of the integral equation were presented, and their accuracies were examined, to understand the effects of mode coupling, proper modeling of object surface, and approximations of triangular basis functions. It was found that for the interior generating curve, the four pulse approximation of the triangular functions was not adequate and the accuracy of different formulations improved significantly, when each interior triangle was modeled by more pulses. The study of the higher order modes indicated that, for a normal incident plane wave, the dominant mode was the $n = 1$ mode, and higher order modes did not have a significant effect on the scattered field.

In chapter 5, the E -field integral equation developed for conducting objects was utilized to solve the radiation problem, in particular, the radiation from a rectangular waveguide. A dipole source was located inside the waveguide and the radiation characteristics of the waveguide were studied for its various geometrical parameters.

6.2. Recommendations

It is recommended that the formulations presented here be extended to study the scattering properties of bodies of arbitrary shape with mix boundary conditions. Investigation of these new topics, however, will result in large matrices to be filled and inverted when the moment method is applied to the integral equations. Hence apart from both excessive computer time and memory required for the solution, the accumu-

lation of roundoff errors would also limit the numerical computation. In addition, if the body had sharp edges or corners, the modal representation, as discussed in chapter three, would not be adequate to account for the field singularities. Usually, a finite number of wave modes will not represent the singularities at the edges adequately and an explicit representation for the edge effect has to be included in the solution. In an attempt to overcome this difficulties, one may select a set of basis functions to incorporate the edge conditions for a faster convergence of the solution. One type of such basis functions can be obtained by multiplying each term of the Fourier basis functions by a singular term. For objects having a corner at $\phi = \phi_e$ such basis function may take the form

$$J^p = f_i(t) \frac{e^{jn\phi_i}}{[\sin^2(\phi_e) - \sin^2(\phi_i)]^{\frac{1}{2}}} \quad (6.1)$$

where, the subscript e indicates the location of the singularity. The justification for such a choice is that, the form $[\sin^2(\phi_e) - \sin^2(\phi_i)]^{\frac{1}{2}}$ exhibits the singular behavior at each corner. Also, it has a form similar to the metric coefficient derived in chapter 2 for the conformal transformation method. In fact, for the schemes given by (6.1) a Gauss-Chebyshev quadrature formula with a weight function of the form $\sqrt{1-x^2}$, where x is the distance from the corner, could be generated to obtain an optimal precision with a minimal sampling. Hence, the remaining portion of the integrand will be regular and may be computed in a straight forward manner. This type of basis functions will be studied in the near future.

Appendix I

Coordinate Transformation

A transformation of the type

$$\frac{dZ}{d\zeta} = \frac{k(\zeta)}{(\zeta^2 - 1)^2}, \quad \begin{aligned} Z &= x + iy \\ \zeta &= u + iv \end{aligned} \quad (\text{I-1})$$

maps the two dimensional region outside a single closed boundary onto a (u, v) half space (Fig. I.1). The properties of $k(\zeta)$ and the integration technique are discussed by Bickley [63]. The second transformation

$$\zeta = \tan \frac{\tau}{2}, \quad \tau = \chi + i\xi \quad (\text{I-2})$$

transforms the half-plane region onto a (χ, ξ) region outside a circle with the boundary itself being the circle. The new coordinates $\chi = \text{constant}$ and $\xi = \text{constant}$ define an orthogonal coordinate system and can be identified as equi-potential and force lines in electrostatics. The surface defined by $\chi = 0$ is the cross-sectional contour of the scatterer.

The Jacobian of the transformation $h(\xi)$ which defines the curvature of the original geometry in the (x, y) plane is defined as

$$h^2(\chi) = \left| \frac{dz}{d\tau} \right|^2 = \left(\frac{dx}{d\chi} \right)^2 + \left(\frac{dy}{d\chi} \right)^2 \quad (\text{I-3})$$

$$h^2(\xi) = \left| \frac{dz}{d\tau} \right|^2 = \left(\frac{dx}{d\xi} \right)^2 + \left(\frac{dy}{d\xi} \right)^2 \quad (\text{I-4})$$

Here, $h(\xi) = h(\chi)$ and can be obtained from the transformation formula. Since the E-field integral equation involves Cartesian derivatives of the surface current J , one requires to transform them to curvilinear coordinates, before generating the matrix elements. The transformation for a function J is

$$\frac{\partial J}{\partial x} = \frac{\partial J}{\partial \xi} \frac{\partial \xi}{\partial x} + \frac{\partial J}{\partial \chi} \frac{\partial \chi}{\partial x} \quad (\text{I-5})$$

$$\frac{\partial J}{\partial y} = \frac{\partial J}{\partial \xi} \frac{\partial \xi}{\partial y} + \frac{\partial J}{\partial \chi} \frac{\partial \chi}{\partial y} \quad (\text{I-6})$$

Since the transformed geometry in the new space has a uniform curvature, the behavior of the metric coefficient is directly related to the curvature of the original geometry in the (x,y) plane.

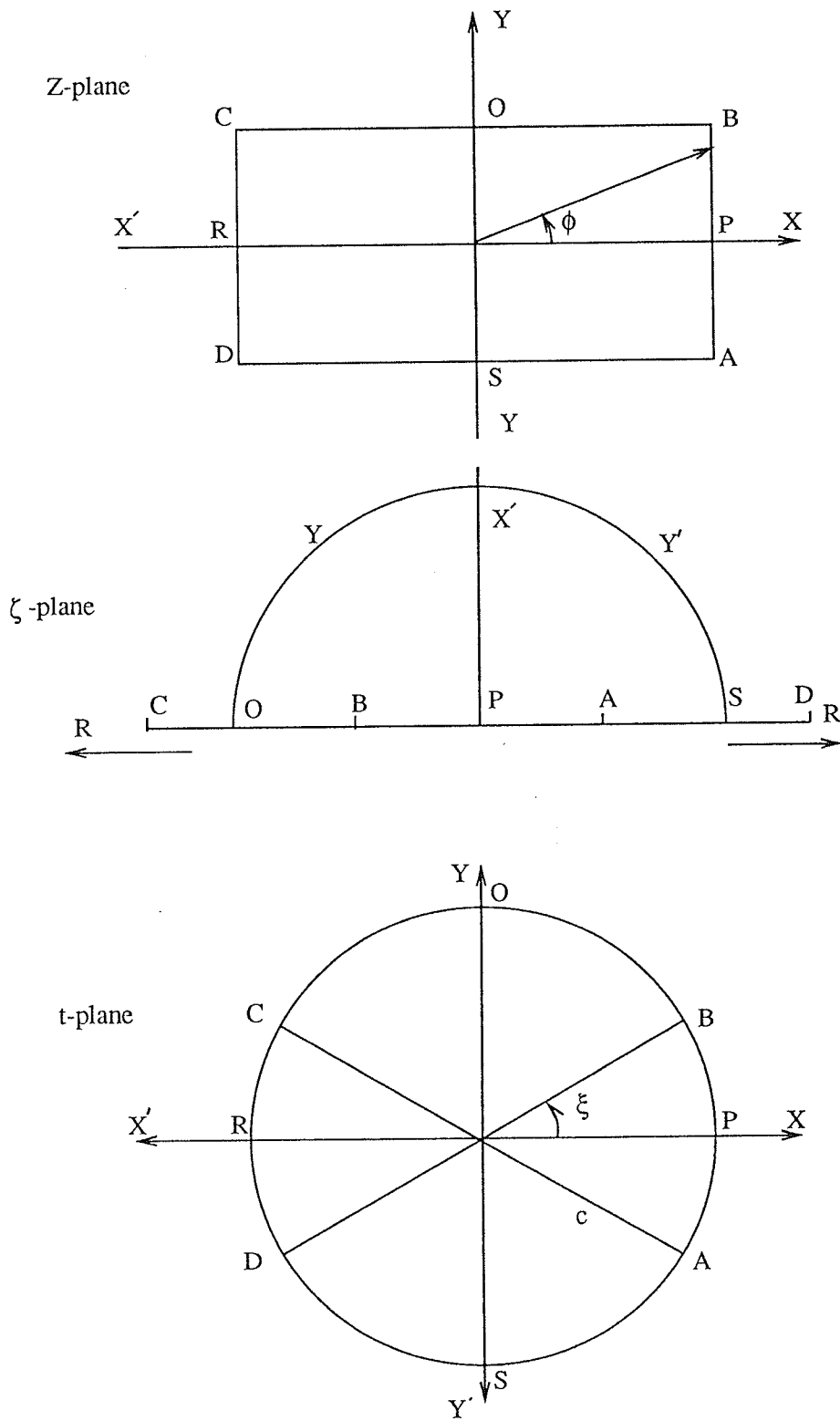


Fig. I.1 : Coordinate transformation of a rectangular cross-section object.

Appendix II

Triangular Basis Function

To evaluate the t directed basis functions, $2M$ impulse functions are selected to approximate each triangle function and its derivatives (Fig. II.1) denoted by T and T' as;

$$T_{2M(J-1)+I} = \frac{k^2}{\Delta_1} \left(\sum_{q=1}^I d_{M(J-1)+q} - \frac{1}{2} d_{M(J-1)+I} \right) d_{M(J-1)+I} \quad (\text{II-1})$$

$$T_{2M^*J-M+I} = \frac{k}{\Delta_2} \left(\Delta_2 - k \sum_{q=1}^I d_{M^*J+q} + \frac{k}{2} d_{M^*J+I} \right) d_{M^*J+I} \quad (\text{II-2})$$

and

$$T'_{2M(J-1)+I} = \frac{k d_{M(J-1)+I}}{\Delta_1} \quad (\text{II-3})$$

$$T'_{2M^*J-M+I} = \frac{-k d_{M^*J+I}}{\Delta_2} \quad (\text{II-4})$$

Here, $J = 1, 2, \dots, N$ and $I = 1, 2, \dots, M$ and

$$N = [(NP - 1)/M] - 1 \quad (\text{II-5})$$

NP is the number of points on the generating curve, and $2M$ represents the number of impulse functions to approximate the triangular functions which represent $f_j(t)$. In the above, Δ_1 and Δ_2 express the electrical length of the generating curve over which the basis function $f_j(t)$ exists and are given by

$$\Delta_1 = k \sum_{I=1}^M d_{M^*(J-1)+I} \quad (\text{II-6})$$

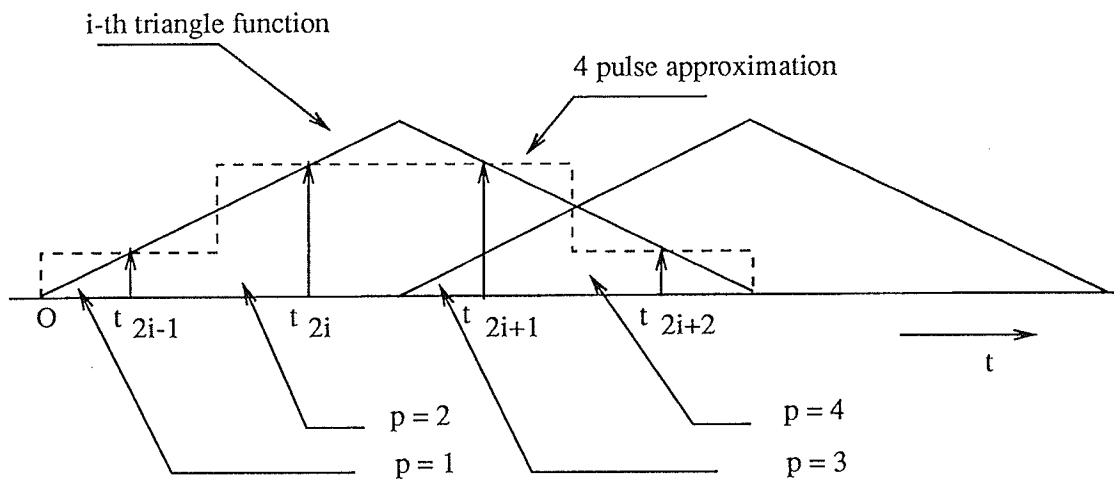
$$\Delta_2 = k \sum_{I=1}^M d_{M^*J+I} \quad (\text{II-7})$$

and d_i is the length of the interval centered about t_i given by

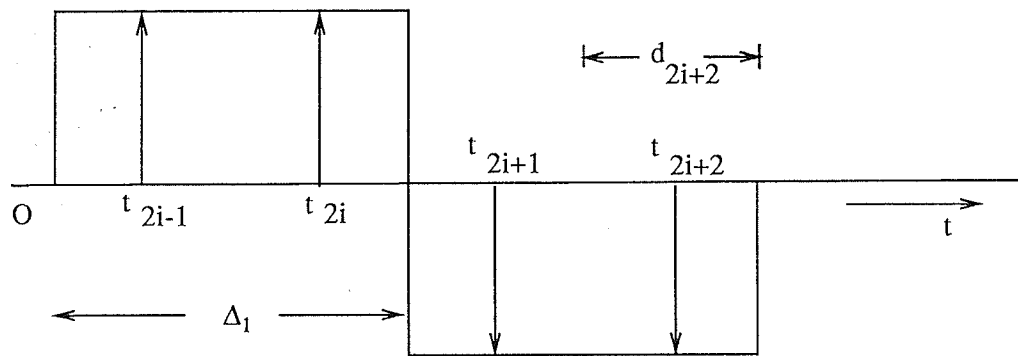
$$d_i = [(\bar{c}_{i+1} - \bar{c}_i)^2 + (\bar{z}_{i+1} - \bar{z}_i)^2]^{\frac{1}{2}} \quad (\text{II-8})$$

where, t_i are the points on the generating curve and defined as

$$t = t_i = (c_i, z_i) = \left(\frac{\bar{c}_i + \bar{c}_{i+1}}{2}, \frac{\bar{z}_i + \bar{z}_{i+1}}{2} \right) \quad (\text{II-9})$$



(a)



(b)

Fig. II.1 : Generic curve of the geometry. (a) Sub-domain representation of surface current. (b) Subdomain representation of surface charge.

Appendix III

Far Field Components of an X-Directed Dipole

For the x -directed dipole located at (x', y', z') , the electric field at a field point (x, y, z) is given by

$$\mathbf{E} = -j\omega\mu\mathbf{A} + \frac{1}{j\omega\epsilon}\nabla(\nabla \cdot \mathbf{A}) \quad (\text{III-1})$$

where

$$\mathbf{A} = \frac{\mathbf{I}l}{4\pi} \frac{e^{-jkR}}{R} \hat{\mathbf{u}}_x \quad (\text{III-2})$$

$\mathbf{I}l$ is the dipole moment, $R = |\mathbf{r} - \mathbf{r}'|$ and k is a wave number. The rectangular field components can be obtained from (III.1) as:

$$E_x = \frac{-j \mathbf{I}l}{4\pi\omega\epsilon} \frac{e^{-jkR}}{R} \left[k^2 - \frac{jk}{R} - \frac{1}{R^2} - (x - x')^2 \left(\frac{k^2}{R^2} - \frac{3jk}{R^3} - \frac{3}{R^4} \right) \right] \quad (\text{III-3})$$

$$E_y = \frac{j \mathbf{I}l}{4\pi\omega\epsilon} (x - x') (y - y') \frac{e^{-jkR}}{R} \left[\frac{k^2}{R^2} - \frac{3jk}{R^3} - \frac{3}{R^4} \right] \quad (\text{III-4})$$

$$E_z = \frac{j \mathbf{I}l}{4\pi\omega\epsilon} (x - x') (z - z') \frac{e^{-jkR}}{R} \left[\frac{k^2}{R^2} - \frac{3jk}{R^3} - \frac{3}{R^4} \right] \quad (\text{III-5})$$

When the dipole is centered on the z axis, $x' = y' = 0$. Neglecting, terms of order in R^{-2} or smaller, the spherical components of the far field can be expressed by

$$E_\theta = \frac{-j\omega\mu \mathbf{I}l}{4\pi} \cos \theta \cos \phi e^{jkz' \cos \theta} \frac{e^{-jkr}}{r} \quad (\text{III-5})$$

$$E_{\phi} = \frac{j\omega\mu Il}{4\pi} \sin\phi e^{jkz'\cos\theta} \frac{e^{-jkr}}{r} \quad (\text{III-6})$$

$$E_r = 0 \quad (\text{III-7})$$

References

- [1] A.W.Maue, "On the formulation of a general scattering problem by means of an integral equation," *Z. Phys.*, vol. 126, no. 7, pp. 601-618, 1949.
- [2] W.K.Saunders, "On solutions of Maxwell's equations in an exterior region," *Proc. Natl. Acad. Sci.*, vol. 38, no. 4, pp. 342-348.
- [3] R.Mitra, *Computer techniques for electromagnetics*. Pergamon Press. New York, 1973.
- [4] J.R.Mautz, R.F.Harrington, "A combined-source solution for radiation and scattering from a perfectly conducting body," *IEEE Trans. Antenna Propagat.*, vol. 27, no. 4., pp. 445-454, 1979.
- [5] A.C.Kelin and R.Mitra, "An application of the condition number concept to the solution of scattering problems in the presence of the interior resonant frequencies," *IEEE Trans. Antenna Propagat.*, vol. 23, no. 3., pp. 431-435, 1975.
- [6] A.D.Yaghjian, "Augmented electric and magnetic-field integral equations," *Radio Sci.*, vol. 16, no. 6, pp. 987-1001, Nov 1981.
- [7] J.R.Mautz and R.F.Harrington, "H-field, E-field, and combined-field solutions for conducting bodies of revolution," *AEU* 32, pp. 157-164, 1978.
- [8] A.A.Kishk and L.Shafai, "Optimization of microstrip feed geometry for prime focus reflector antenna," *IEEE Trans. Antenna Propagat.*, vol. 37, no. 4., pp. 445-451, Apr. 1989.
- [9] S.Abdelmessih and G.Sinclair, "Treatment of singularities in scattering from perfectly conducting polygonal cylinders- A numerical technique," *Can. J. Phys.* vol. 45, pp. 1305-1318, 1967.

- [10] C.R.Mullin, R.Sandburg, and C.O.Valline, "A numerical technique for the determination of scattering cross sections of infinite cylinders of arbitrary geometrical cross section," *IEEE Trans. Antenna Propag.*, vol. 13, pp. 141-145, 1965.
- [11] K.Meï and J.Van Bladel, "Scattering by perfectly conducting rectangular cylinders. *IEE Trans. Antenna Propag.* pp. 185-192, Mar 1963.
- [12] J. Meixner, "The behavior of electromagnetic fields at edges," *Ann. Phys.*, vol. 6. no. 6, 1949.
- [13] L.Shafai, "An improved integral equation for the numerical solution of two-dimensional diffraction problems," *Can. J. Phys.* vol. 48, pp. 954-963, 1970.
- [14] H.H.Meinke, In *electromagnetic theory and antennas, part 2.* pp. 1113-1124, Pergamon Press Ltd., Oxford, 1963.
- [15] W.H.Watson, Report no. AFCRL-66-91, Lockheed Missiles and Space Company, Sunnyvale, CA, 1966.
- [16] R.F.Harrington, *Field Computation By Moment Methods.* MacMillan, New York, 1968.
- [17] P.C.Waterman, "Scattering by dielectric obstacles," *Altra Freq.* Vol. 38, PP. 348-352, 1969.
- [18] G.A.Thiele and T.H.Newhouse, "A hybrid technique for combining moment methods with the geometrical theory of diffraction," *IEEE Trans. Antenna Propagat.* vol. 17, pp. 62-69, Sep 1969.
- [19] W.D.Burnside and P.H.Pathak, "A summary of hybrid solutions involving moment methods and GTD," in *applications of the method of moments to electromagnetic fields*, B.J.Strait, Ed. St. Cloud, FL: SCEEE Press, 1980.
- [20] K.Meï, "Unimoment method of solving antenna and scattering problems," *IEEE Trans. Antenna Propag.* vol. 22, pp. 760-766, 1974.

- [21] S.K.Chang and K.Mei , "Application of the the unimoment method to electromagnetic dielectric cylinders," IEEE Trans. Antenna Propag. vol. 24, pp. 35-42, 1976.
- [22] E.K.Miller, "A selective survey of computational electromagnetics," IEEE Trans. Antenna Propag. vol. 36, no. 9, pp. 1281-1305, 1988.
- [23] T.K.Sarkar and S.M.Rao, "The application of the conjugate gradient method for the solution of the electromagnetic scattering from arbitrary oriented wire antennas," IEEE Trans. Antenna Propag. vol. 32, no. 4, pp. 398-403, 1984.
- [24] T.K.Sarkar, "The conjugate gradient technique as applied to electromagnetic field problems," IEEE AP-S Newsletter, vol. 28, no. 4, pp. 5-14, 1986.
- [25] T.K.Sarkar, E.Arvas, and S.M.Rao, "Applications of FFT and conjugate gradient method for the solution of the electromagnetic radiation from electrically large and small conducting bodies," IEEE Trans. Antenna Propag. vol. 33, no. 5, pp. 635-640, May 1986.
- [26] N.N.Bojarski, "K-space formulation of the acoustic scattering problem," in Proc. Acoustical Soc. of Amer. Symp., Miami, FL, 1972, pp. 102.
- [27] R.Mitra and R.Kastner, "A spectral domain approach for computing the radiation characteristics of a leaky-wave antenna for millimeter waves," IEEE Trans. Antenna Propag. vol. 29, pp. 652-654, 1981.
- [28] R.Kastner and R.Mitra, "A spectral-iteration technique for analyzing scattering from arbitrary bodies-I: Cylindrical scatterer with E-wave incidence," IEEE Trans. Antenna Propag. vol. 31, pp. 499-506, 1983.
- [29] M.F.Catedra, J.G.Cuevas, and L.Nuno, "A scheme to analyze conducting plates of resonant size using the conjugate-gradient method and the Fast Fourier Transform," IEEE Trans. Antenna Propag. vol. 36, no. 12, pp. 1744-1752, Dec. 1988.

- [30] J.H.Richmond, "A wire-grid model for scattering by conducting bodies," IEEE Trans. Antenna Propagat., vol. 14, no. 6, pp. 782-786, Nov 1966.
- [31] J.L.Lin, and W.L.Curtis, "Radar cross section of a rectangular conducting plate by wire mesh modeling," IEEE Trans. Antenna Propagat., vol. 14, no. 6, pp. 718-720, Sep 1974.
- [32] A.Ludwig, "Wire grid modeling of surfaces," IEEE Trans. Antenna Propag. vol. 35, no. 9, Sep 1987.
- [33] K.S.H.Lee, L.Maria, and J.P.Castillo, "Limitations of wire-grid modeling of a closed surface," IEEE Trans. Electrmagn. Compat., vol. 18, pp. 123-129, Aug. 1976.
- [34] L.L.Tsai, D.G.Dudley, and D.R.Wilton, "Electromagnetic scattering by a three-dimensional conducting rectangular box," J.A.Phys., vol. 45, no. 10, pp. 4393-4400, Oct 1974.
- [35] G.J.Burke and A.J.Poggio, "Numerical electromagnetic code(NEC)-method of moment," Naval Ocean Systems Center, San Diego, CA, Tech. Document 116, July 1977.
- [36] A.Sankar and T.C.Tong, "Current computation on complex structures by finite element method," Electron. Lett. vol. 11, no. 20, pp. 481-482, Oct 1975.
- [35] J.J.H.Wang, and C.J.Drane, "Numerical analysis of arbitrary shaped bodies modeled by surface patches," IEEE Trans. MTT., vol. 30, no. 8., pp. 1167-1173, Aug 1982.
- [36] S.Rao, D.Wilton, and A.Glisson, "Electromagnetic scattering by surfaces of arbitrary shape," IEEE Trans. Antenna Propagat., vol. 30, pp. 409-418, May 1982.
- [37] E.Arvas, R.F.Harrington, and J.R.Mautz, "Radiation and scattering from electrically small conducting bodies of arbitrary shape," IEEE Trans. Antenna Propagat., vol. 34, no. 1., pp. 66-77, Jan 1986.

- [38] E.Newman, P.Tulyathan, "A surface patch model for polygonal plates ," IEEE Trans. Antenna Propagat., vol. 30, pp. 588-593, July 1982.
- [39] L.N.Medgyesi-Mitschang and J.M.Putnam, "Scattering from finite bodies of translation: plates, curved surfaces, and nonlinear cylinders," IEEE Trans. Antenna Propagat., vol. 31, no. 6, pp. 847-852, Nov 1983.
- [40] J.R.Muatz and R.Harrington, "H-field, E-field, and combined-field solutions for conducting bodies of revolution," AEU 32, pp. 157-164, 1978.
- [41] S.B.Alder, and R.S.Johnson, "New back-scattering computation and tables for dielectric and metal spheres," Appl. Optics, vol. 1, pp. 655-660, 1962.
- [42] A.L.Aden, and M.Kerker, "Scattering of electromagnetic waves from two concentric spheres," J. of Applied Physics, vol. 22, pp. 1242-1246, 1951.
- [43] P.Barber and C.Yeh, "Scattering of electromagnetic waves by arbitrary shaped dielectric bodies," Appl. Opt., vol. 14, no. 12, pp. 2864-2872, Dec 1975.
- [44] T.K.Wu and L.L.Tsai, "Scattering from arbitrarily-shaped lossy dielectric bodies of revolution," Radio Sci. vol. 12, pp. 709-718, Sept. 1977.
- [45] A.Taflove and M.E.Brodwin, "Computational of the electromagnetic fields and induced temperatures within a model of the microwave-irradiated human eye," IEEE Trans. MTT, vol. 23, pp. 888-896, Nov 1975.
- [46] A.G.Papayiannakis and E.E.Kriezis, "Scattering from a dielectric cylinder of finite length," IEEE Trans. Antenna Propagat., vol. 31, pp. 725-731, Sep 1983.
- [47] J.R.Mautz, and R.F.Harrington, "Electromagnetic scattering from a homogeneous material body of revolution," Arch. Elek. Ubertragung, vol. 33, No. 4, pp.71-80, Apr. 1979.
- [48] A.A.Kishk and L.Shafai, "On the accuracy limits of different integral-equation formulations for numerical solution of dielectric bodies of revolution," Can. J. Phys., vol. 63, pp. 1532-1539, Oct 1984.

- [49] R.Holland, L.Simpson, and K.S.Kunz, "Finite-difference analysis of EMP coupling to lossy dielectric structures," *IEEE Trans. Electro. magn. Compat.*, vol. 22, pp. 203-209, Aug. 1980.
- [50] D.E.Livesay and K-M Chen, "Electromagnetic fields induced inside arbitrarily shaped biological bodies," *IEEE Trans. MTT*, vol. 22, pp. 1273-1280, Dec. 1974.
- [51] M.J.Hagman, O.P.Ghandhi, and C.H.Durnay, "Numerical calculation of electromagnetic energy deposition for a realistic model of man," *IEEE Trans. MTT*, vol. 27, pp. 804-809, Sept. 1979.
- [52] T.K.Sarkar, E.Arvas, and S.Ponnappalli, "Electromagnetic scattering from dielectric bodies," *IEEE Trans. Antenna Propag.* vol 37, No. 5, pp. 673-676, May 1989.
- [53] D.H.Schaubert, D.R.Wilton and A.W.Glisson, "A tetrahedral modeling method for electromagnetic scattering by arbitrarily shaped inhomogeneous dielectric bodies," *IEEE Trans. Antenna Propag.* vol. 32, pp. 77-85, Jan 1984.
- [54] C.C.Su, "Electromagnetic scattering by a dielectric body with arbitrary inhomogeneity and anisotropy," *IEEE Trans. Antenna Propag.* vol 37, No. 3. pp. 384-389, Mar 1989.
- [55] E.K.Miller, "A selective survey of computational electromagnetics," *IEEE Trans. Antenna Propagat.* vol. 36, no. 9, pp. 1281-1305, Sep 1988.
- [56] G.J.Burke and A.J.Poggio, "Numerical electromagnetic code(NEC)-method of moment," Naval Ocean Systems Center, San Diego, CA, Tech. Document 116, July 1977.
- [57] L.Shafai, and P.Bhartia, "Scattering by a conducting aerofoil," *AEU*, vol. 27, pp.447-448, 1973.
- [58] L.Shafai, "Application of coordinate transformation to two-dimensional scattering and diffraction problems," *Can. J. Phys.* vol. 47, pp. 795-804, 1968.

- [59] W.G.Bickley, "Two dimensional potential problems for the space outside a rectangle," London Math. Soc. Proc., pp. 82-105, May, 1932.
- [60] H.Moheb and L.Shafai, "On the numerical accuracy of different integral equations for scattering from surfaces," ISAE 89, Intern. Symp., Shanghai, China, Aug. 1989.
- [61] L.shafai and H.Moheb, "Application of mapping function for numerical solution of scattering by arbitrary shape objects," ICAP 89, London, UK, Apr 1989.
- [62] H.Moheb and L.Shafai, "Geometrical transformation of bodies of arbitrary cross-section for numerical computation," IEEE AP-S, Intern. Symp., San Jose, CA, June 1989.
- [63] W.G.Bickley, " Two dimensional potential problems concerning a single closed boundary," London Math. Soc. Proc., pp. 235-274, June, 1929.
- [64] N.N.Wang, J.H.Richmond, M.C.Gilreath, "Sinusoidal reaction formulation for radiation and scattering from conducting surfaces," IEEE Trans. Antenna Propagat., vol. 23, no. 3, pp. 376-382, Sep 1988.
- [65] L.L.Tsai, "Radar cross section of a simple target:A three-dimensional conducting rectangular box," IEEE Trans. Antenna Propagat., vol. 25, no. 6, pp. 882-884, Nov. 1977.
- [66] M.G.Cote, M.B. Woodworth, and A.D.Yaghjian, "Scattering from the perfectly conducting cube," IEEE Trans. Antenna Propagat., vol. 36, no. 9, pp. 1321-1329, Sep 1988.
- [67] J.H.Richmonds, "Scattering by a dielectric cylinder of arbitrary cross section shape," IEEE Trans. Antenna Propag. vol. 13, pp. 334-341, May 1965.
- [68] J.H.Richmonds, "TE-wave scattering by a dielectric cylinder of arbitrary cross section shape," IEEE Trans. Antenna Propag. vol. 14, pp. 460-464, July 1966.

- [69] V.V.Solodukhov and E.N.Vasilev, "Diffraction of a plane electromagnetic wave by a dielectric cylinder of arbitrary cross section," Soviet Physics, vol. 15, no. 1, July 1970.
- [70] N.Morita, "Analysis of scattering by a dielectric rectangular cylinder by means of integral equation formulation," Electr. & Comm. in Japan, vol. 57-B, no. 10, 1974.
- [71] C. Muller, Foundation of the mathematical theory of electromagnetic waves, Springer-verlag, pp. 301, 1969.
- [72] A.A.Kishk and L.Shafai, "Improvement of the solution accuracy for dielectric bodies using method of moments. IEEE AP-S, Intern. Symp., Blacksburg, Virginia , pp. 260-263, 1987.
- [73] A.J.Poggio and E.K.Miller, Computer techniques for electromagnetics. Pergamon Press. New York, 1973.
- [74] E.Jull, "Aperture fields and gain of open-ended parallel-plate waveguides," IEEE Trans. Antenna Propag. vol 21, No. 1. pp. 14-18, Jan. 1973.
- [75] R.J.Mailloux, "Radiation and near-field coupling between two collinear open-ended waveguides," IEEE Trans. Antenna Propag. vol 17, No. 1. pp. 49-55, Jan. 1969.
- [76] D.G.Bodnar, and D.T.Paris, "New variational principle in electromagnetic," IEEE Trans. Antenna Propag. vol 19, pp. 216-223, Mar. 1970.
- [77] A.R.Jamieson and T.E.Rozzi, "Rigorous analysis of cross-polarization in flanged-mounted rectangular waveguide radiators," Electron. Lett. vol 13, pp. 742-744, Nov. 1977.
- [78] H.Baudrand, J.W.Tao, and J.Atechian, "Study of radiating properties of open-ended rectangular waveguides," IEEE Trans. Antenna Propag. vol 36, No. 8, pp. 1071-1077, Aug. 1988.

- [79] R.H.Macphie, and A.I.Zaghloul, "Radiation from a rectangular waveguide with infinite flange-Exact solution by the correlation matrix method," IEEE Trans. Antenna Propag. vol 28, No. 4. pp. 497-503, July 1980.
- [80] R.F.Harrington, and J.R.Mautz, "Electromagnetic transmission through an aperture in a conducting plane AEU. vol 31, No. 2. pp. 81-87, 1977.
- [81] A.D.Bresler, G.H.Joshi, and N.Marcuvitz, "Orthogonality properties for modes in passive and active uniform wave guides," J. Appl. Phys., vol. 20, no. 5, pp. 794-799, May 1958.
- [82] K.A.Iskander, et al., "Application of impedance boundary conditions to numerical solution of corrugated circular horns," IEEE Trans. Antenna Propagat., vol 30, no. 3., pp. 366-372, May. 1982.
- [83] L.Shafai and A.Kishk, "Coaxial waveguides as primary feeds for reflector antennas and their comparison with circular waveguides," AEU, vol. 39, no. 1., pp. 8-14, 1985.
- [84] H.Moheb and L.Shafai, "On the numerical study of radiation characteristics of rectangular waveguides," ANTEM90, Intern. Symp., Wpg., Canada, Aug. 1990.
- [85] A.C.Ludwig, "The definition of cross-polarization," IEEE Trans. Antenna Propag. vol 21, pp. 116-119, Jan. 1973.
- [86] A.W.Rudge, et al., "Low cross-polar waveguide horns for multiple-feed reflector antennas," IEE conf. , Antennas and Propagat., pp.360-363, Nov. 1978.